5-2023

A Multi-Wavelength Remote Sensing Investigation of Lunar Surface and Crustal Evolution

Cole Nypaver
University of Tennessee, cnypaver@vols.utk.edu

To the Graduate Council:

I am submitting herewith a dissertation written by Cole Nypaver entitled "A Multi-Wavelength Remote Sensing Investigation of Lunar Surface and Crustal Evolution." I have examined the final electronic copy of this dissertation for form and content and recommend that it be accepted in partial fulfillment of the requirements for the degree of Doctor of Philosophy, with a major in Geology.

Dr. Bradley Thomson, Major Professor

We have read this dissertation and recommend its acceptance:

Dr. Molly McCanta, Dr. Nicholas Dygert, Dr. Edgard G. Rivera-Valentín, Dr. Jeffrey Moersch

Accepted for the Council:

Dixie L. Thompson

Vice Provost and Dean of the Graduate School

(Original signatures are on file with official student records.)

A Multi-Wavelength Remote Sensing Investigation of Lunar Surface and Crustal Evolution

A Dissertation Presented for the
Doctor of Philosophy
Degree
The University of Tennessee, Knoxville

Cole Nypaver
May 2023

“I’m sure that, to a geologist, the Moon is a fascinating place, but this monotonous rock pile, this withered, sun-seared peach pit out my window offers absolutely no competition to the gem it orbits. Ah the Earth, with its verdant valleys, its misty waterfalls. I’d just like to get our job done and get out of here.”

-Astronaut Michael Collins
Apollo 11 Command Module Pilot
Quote from *First Man* by James R. Hansen

Acknowledgments

Similar to many intellectual pursuits, a Ph.D. in the natural sciences is not a singular effort. The people, places, and experiences that have shaped my understanding of and passion for planetary science are far too numerous to list here. Still, there are several people in particular who deserved recognition for their contribution to the work presented in this volume.

I would first like to thank my advisor, Dr. Bradley Thomson, for his undying support, guidance, and friendship throughout my graduate career. Mere words are not adequate to express my appreciation for all that he has done for me. Brad witnessed my potential long before I saw it, myself, and I would not be the scientist or person that I am today without him.

I would also like to thank my dissertation committee members, Dr. Molly McCanta, Dr. Nicholas Dygert, Dr. Edgard G. Rivera-Valentín, and Dr. Jeffrey Moersch for their time, guidance, and feedback throughout my graduate career.

I would like to thank my numerous colleagues at institutions around the country for the feedback, productive discussion, and suggestions that allowed me to grow as a scientist and greatly improved the overall quality of this work. These individuals include, but are not limited to Dr. Caleb Fassett, Dr. G. Wesley Patterson, Dr. Jacklyn Clark, Dr. Joshua Cahill, Dr. Tom Watters, Dr. Peter Schultz, Dr. Catherine Neish, Dr. Catherine Elder, and Dr. David Kring.

Thank you to my parents, Kirk and Donna Nypaver, who made continuous sacrifices for the sake of my education and wellbeing throughout my life. From a young age, they instilled in me the value of education and an innate curiosity for nature and the outdoors. I would not be the person that I am without them. Thank you also to my brother, Kirk C. Nypaver, for his continual companionship and mentorship throughout my life.

Thank you to my lab mates, Cameron Harris, Ivy Ettenborough, Tyler Seglynski, and Dailey Sparks for their continual support and willingness to listen to my prolonged lunar science-related soliloquies during our weekly group meetings.

Thank you to the UTK Department of Earth and Planetary office staff, Angie Staley, Marie Ballard, Melody Branch, and Teresa Parrot for their continual support and assistance throughout my time at UTK.

Thank you to all of my friends from the science, running, cycling, and outdoor realms for their companionship and encouragement over the past six years. Specifically, thank you to Dave Kesterson, Hayden Foltz, Trevor Barnes, Carter

Hall, Peyton Gupton, Cassidy Gupton, Brandon Bagley, Dr. Sam Gwizd, Dr. Michael Phillips, Hannah Rigoni, Hannah McCarty, Cameron McCarty, Dr. Audrey Martin, Diego Sanchez, Pete Schreiner, Vinnie Athey, Katie Woodfin, Taylor Woodfin, Liz Canty, Luke Hough, Wes Ormond, Robert Jacobsen, Hannah Jacobsen, The Coker family, Kira O'Sullivan, Matt Bartow, Anthony Maue, Chad Melton, Claire Mondro, CJ Leight, Louisa Rader, and Cameron Hughes – your friendship in my life has been invaluable and something that I will cherish forever.

To my dogs, Lucy and Buzz. No matter how tremendous my successes or failures, it brings me comfort to know that you both will always love me as much as possible. Woof!

Lastly, thank you to my lovely wife, Dr. Jessica Ende, for being a constant source of love, support, guidance, and inspiration throughout my time as a graduate student. I'll never be as beautiful, interesting, or as kind as you, but at least we can have the same academic degree.

Abstract

The surface of Earth's Moon is a complex geologic system that continues to evolve due to a variety of ongoing geologic processes. The goal of this dissertation was to identify and quantify current endogenic and exogenic sources of lunar surface modification using remote sensing data. Radar and thermophysical measurements of 6,221 impact craters on the lunar nearside mare have indicated that lunar regolith is highly mobile at crater rims, making those areas ideal locations for lunar sampling initiatives (Chapter 1). Furthermore, a detailed mapping of recently formed tectonic features on the Moon revealed >1000 wrinkle ridges that are recently or currently active in deforming the lunar surface (Chapter 2). That addition of small-scale wrinkle ridges to the lithospheric stress budget of the Moon allowed for the first globally complete perspective of recent lunar tectonism. Lastly, drone-based thermophysical data collected over the ejecta of Barringer Meteorite Impact crater in NE Arizona, USA indicated that coarse-resolution measurements of impact ejecta on the Moon may be excluding key details about impact crater and ejecta formation processes (Chapter 3). The combination of these investigations has indicated that Earth's Moon is recently (if not, currently) active and the resulting surface acceleration and surface displacements are likely responsible for regional regolith movement in high-sloping areas of the lunar surface – such as crater rims where subsurface boulders are actively being exhumed. This work also reveals that the remote sensing data used to identify and measure those processes may be limited in the scale of geologic information that they may provide. These findings are relevant to future lunar surface science investigations for which a compositionally diverse sampling of locally sourced lunar surface material is desired. Moreover, the results of this work show that a better understanding of lunar surface processes is dependent on the quality and resolution of any future data that might be obtained over the lunar surface.

Table of Contents

List of Tables

List of Figures

INTRODUCTION

The Effect of Lunar Exploration

As you read this dissertation, it would be reasonable to ask the question “Why dedicate the time and funding to lunar research and exploration?”, or more generally, “Why conduct planetary research at all?” Perhaps you’ve asked those questions long before picking up this volume of work, or perhaps you will be challenged with those questions in the future. It is a reasonable query after all. The United States space budget was nearly $41 billion dollars in 2021 – over half of which was dedicated solely to space exploration. With those figures in mind, our question becomes one of the value that space exploration holds to humankind relative to the other needs and demands of a modern society. You need not look farther back than Apollo 8 for an answer. The Apollo 8 mission, crewed by Astronauts Frank Borman, James Lovell, and William Anders, was the first mission in which human beings orbited Earth’s Moon. It was during that mission, on Christmas Eve, 1968, and just before the scheduled trans-Earth injection burn that would bring the Apollo 8 crew back home, that Astronaut Bill Anders captured a photo of Earth slowly rising above the lunar horizon. The photo that was stored in Anders’ camera on that day would alter the public perception of our celestial home and the fragility of life as we know it. That photo was called “Earthrise.”

When the Earthrise photograph was inevitably published in magazines and newspaper articles around the world, humankind observed their home planet without the illustration of defined countries that belonged to any one person or group of people. They saw an atmosphere so thin and delicate, that it was barely visible to the naked eye. They saw, for the first time in its entirety, a delicate planet that was worth protecting. In the years that followed, the U.S. Environmental Protection Agency, the National Oceanic and Atmospheric Administration (NOAA), The United Nations Conference on the Human Environment, and The United Nations Environment Programme were all initiated. The first Earth Day was held on April 22nd, 1970. New amendments to the Clean Air Act were signed into law on December 31st, 1970. Dichlorodiphenyltrichloroethane (DDT) and leaded gasoline were banned in 1972 and 1975, respectively. This inexhaustive list illustrates that the benefit of planetary research is not only an improved understanding of the planet being investigated, but an improved perspective of our own planet and society as well.

In the 54 years since the Earthrise photo was first presented to humanity, I fear that the wholesome perspective granted by the Apollo program has been lost on much of the world around me. However, I simultaneously feel fortunate that my time in the field of planetary geoscience has come on the eve of the most ambitious lunar exploration program since the Apollo era. The Artemis space program will provide a renewed perspective on what it means to inhabit planet Earth in the modern era, but I am confident that the societal impacts of Artemis will not end with improved environmental awareness and disseminated technological innovation. Artemis III will see the first woman and person of color

set foot on the Moon — thus, extending the inspiration of lunar exploration to a wider range of individuals who, may one day, change the world in their own way.

I can only hope that my own research and dissertation plays a small part in improving the understanding of our closest celestial neighbor and paves the way for the next generation of lunar exploration.

A Geologically Dynamic Moon

The geologic history of Earth is readily attainable. The collision and separation of immense slabs of continental crust, the evolution and erosion of orogenic events on an unimaginable scale, the rise and fall of oceans and shallow seas — all recorded in the terrestrial rock record and measurable in microscopic detail. The recent geologic evolution of Earth's surface is also readily discernible even to the naked eye as evidenced by the migration of fluvial systems and aeolian dunes on a timescale of months to decades. Relative to the ever-apparent geologic evolution of Earth's surface, the monotone and quiescent appearance of the lunar surface may lead to the interpretation that Earth's Moon is somehow geologically inactive. This assumption is far from accurate. It is true that the Moon lacks plate tectonics, liquid water, or a substantive atmosphere, but the absence of those geologic and environmental attributes exposes the lunar surface to energetic processes that are just as dynamic, albeit fundamentally different than, those that operate on Earth. The work presented in this dissertation primarily focuses on two of these processes — impact cratering and global tectonics — and how those processes can be measured to inform our understanding of lunar history.

The dominant geologic process acting on the lunar surface is impact crater formation. Without a substantial atmosphere to shield it from incoming bolides, the Moon has been continuously bombarded by hypervelocity impactors ranging in diameter from micrometers to kilometers. While larger impactors were more common earlier in lunar history during and immediately after the primordial late heavy bombardment, smaller micrometeoroids are the most pervasive cause of surface alteration in recent lunar history. The continual sandblasting of the lunar surface by micrometeoroids results in the long-term breakdown of lunar rocks and boulders into fine grained lunar regolith. The same micrometeoroid bombardment process that forms the lunar regolith then continues to churn the fine-grained regolith and facilitate its downslope movement. On geologic timescales, this process of rock breakdown and regolith movement is a powerful force of geomorphic change that can reduce crisp impact craters and other topographic features into muted structures that are hardly recognizable to the human eye. Understanding the rate of impact-induced topographic change will be a recurring theme in the work presented here and is valuable to our understanding of the lunar chronology — a tool that has applications for unraveling the geologic history of the greater solar system and the search for life on other solid bodies.

Impact cratering is an inherently exogenic process that is readily apparent when viewing the Moon at a large scale, but the geologic activity of the Moon does not end with mere surface alteration. Roughly 600 Ma after the formation of the Moon, the lunar thermal state shifted from net expansion to net contraction as the lunar interior began to cool. Since this shift, the lunar lithosphere has been in a constant state of compressional stress. Such a compressional stress field was further complicated by the outpouring of flood basalts on the lunar nearside known as the lunar maria in the Late Imbrian-Eratosthenian time period (~3.6–2.0 Ga). The isostatic response of the lunar lithosphere to the formation of the lunar maria resulted in the localized formation of kilometer-scale, linear compressional features, known as wrinkle ridges, in the basins that contained the mare basalts. The kinematic relationship between wrinkle ridges and lunar mare formation indicates that their growth largely halted with the end of the emplacement of the lunar maria approximately ~2.0 Ga. It was only recently that younger tectonic features were identified using new high-resolution images returned from the Lunar Reconnaissance Orbiter. Those data were used to identify a global population of small, compressional tectonic features in the lunar highlands known as lobate scarps that formed recently (<500 Ma) due to the combination of solid body tides, orbital recession of the Moon away from Earth, and lunar global contraction. The work presented in this dissertation builds on those observations by presenting a newly identified population of small, arcuate wrinkle ridges in the lunar maria that are similar to lobate scarps in both scale and formation timing. This new class of tectonic feature helps to complete our understanding of mechanisms responsible for recent deformation of the lunar lithosphere and how the lunar stress state has evolved over time.

Alas, the body of work presented here is not an exhaustive summation of all lunar geologic processes. Mass wasting, effusive volcanism, pyroclastic volcanism, volatile deposition, interior dynamics, and radiogenic sputtering all play or have played a valued role in lunar geologic history — each with a compelling scientific narrative that I would be delighted to review for the reader. However, in the work presented here, I rely only on the work of my graduate career — guided by my advisor, colleagues, and mentors — to tell the story of the geologically dynamic Moon.

CHAPTER ONE : PROLONGED ROCK EXHUMATION AT THE RIMS OF KILOMETER SCALE LUNAR CRATERS

A version of this chapter was published in the Journal of Geophysical Research: Planets by Cole A. Nypaver, Bradley J. Thomson, Caleb I. Fassett, Edgard G. Rivera-Valentín, and Gerald W. Patterson:

Nypaver, C., Thomson, B. J., Fassett, C. I., Rivera-Valentín, E. G., Patterson, G. W. (2021) Prolonged Rock Exhumation at the Rims of Kilometer-Scale Lunar Craters. Journal of Geophysical Research. Planets, 126(7). https://doi.org/10.1029/2021JE006897.

Abstract

Fresh impact ejecta deposits on the lunar surface can be characterized as heterogeneous mixtures of boulders, cobbles, and fine-grained regolith that are deposited on the lunar surface during the impact crater formation process. Over time, the surface boulders associated with ejecta deposits break down into fine-grained regolith due to a combination of later impacts and thermal fatigue. Nonetheless, observations of old (>2.0 Ga) kilometer-scale (0.8–2.0 km) lunar impact craters in high-resolution images reveal >1 m boulders along their rims and in their near-proximal ejecta deposits on the lunar maria. Here, we use a combination of radar and thermal-infrared data from the Lunar Reconnaissance Orbiter spacecraft to show that the rims of kilometer-sized impact craters exhibit elevated rock abundances for the lifetime of the lunar maria. We interpret these results as indicating that boulders are continually being uncovered at crater rims due to downslope movement of the overlying regolith. Moreover, rocks found at crater rims that have been exhumed from depth in geologically recent times are locally derived and unlikely to have come from other areas of the Moon. Future collection of lunar samples at crater rims will serve to mitigate the potential for

sample contamination from distal sources, helping to ensure accurate geologic interpretations from the collected samples.

Introduction

The surface of the Moon is dominated by the geomorphological effects of impact craters, and recent remote sensing data provided by the Lunar Reconnaissance Orbiter (LRO) have helped to improve our understanding of those effects on impact crater ejecta deposits (e.g., Neish et al., 2013; Ghent et al., 2014; 2016; Fassett et al., 2018; Wang et al., 2020; Hörz et al., 2020; Ruesch et al., 2020). However, many questions remain regarding the rate at which impact ejecta deposits are modified, the mechanisms responsible for surface changes, and the suitability of remote sensing data for assessing these geologic processes.

Recent work using S-band (12.6 cm, 2380 MHz) radar data from the LRO Miniature Radio-Frequency (Mini-RF) instrument revealed that while surface and subsurface rock populations associated with lunar impact ejecta are diminished with time due to space weathering processes, the rock content of impact crater interiors increases for the first ~0.5 Gyr of a crater's lifetime (Fassett et al., 2018). A separate study used thermal infrared measurements from the LRO Diviner thermal radiometer to infer that boulders within ejecta deposits associated with large (~18–100 km) lunar impact craters break down in less than 1.0 Gyr, and that rate could be used to estimate an approximate age for large diameter impact craters on the lunar surface (Ghent et al., 2014; 2016). The rate of ejecta

breakdown established by that work was more recently utilized to infer an increase in the inner Solar System cratering rate in the last ~290 Myr (Mazrouei et al., 2019). Additionally, several studies have utilized high-resolution images from the Lunar Reconnaissance Orbiter Camera (LROC) to manually count the number of boulders present in lunar ejecta deposits associated with craters of varying ages (e.g., Basilevsky et al., 2013; 2015; 2018; Li et al., 2018; Watkins et al., 2019). Those data were used to infer that most boulders ≥2 m on the lunar surface are destroyed in less than 300 Myr, likely due to meteoroid impacts and thermal fatigue of exposed rocks at the lunar surface (e.g., Hörz et al., 1975; Molaro et al., 2017; Ruesch et al., 2020). The contradictory lifetimes of boulder breakdown given in the aforementioned studies indicate that the post formation fate of impact craters and impact ejecta is far from simple and breakdown processes and rates have yet to be fully constrained.

Key differences exist between prior boulder lifetime studies in the form of impact crater age determination methods, impact crater size, and measurement location and area. Lunar impact crater age estimates are robust but have ~10–30% systematic uncertainties between investigators (Robbins et al., 2014). Past studies have established crater ages by utilizing crater counting methods and qualitative morphology comparisons with craters that possess radiometric age dates from Apollo samples (e.g., Arvidson et al., 1975). Other analyses of boulder breakdown, which utilized the rock sensitivities of thermal and radar data, studied craters with larger (~18–97 km) diameters (Ghent et al., 2014).

Craters of that size exhibit much larger boulders, more extensive ejecta deposits, and different topographic modification rates (e.g., Bart and Melosh, 2010; Fassett et al., 2018a; Minton et al., 2019). Those studies utilizing remote sensing-based methods to establish boulder lifetimes via measured data over the entire continuous ejecta deposit used their measurements to estimate the percentage of the surfaces that were occupied by meter-scale boulders (Ghent et al., 2014; 2016). That method differed from boulder count-based lifetime studies that relied upon a 100×100 m^2 count area within the respective crater ejecta deposit (Basilevsky et al., 2013). The boulder densities obtained within that smaller count area were then extrapolated under the assumption that the selected count area was representative of the whole ejecta deposit.

In the work presented here, an initial assessment of old (>2.0 Gyr) kilometer-scale craters on the lunar maria visually revealed tens of large (>1.0 m) boulders associated with the ejecta on and just outside of the impact crater rims with a lack of boulders beyond that narrow annular zone (Fig. 1.1 - All figures and tables mentioned are included in appendices at the end of each chapter). This observation of heightened boulder populations at crater rims has also been noted in early characterizations of the lunar surface. For example, Apollo 17 astronauts documented a sharp boundary in surface rock percentage between the rim and ejecta deposit of Camelot crater (e.g., Schmitt et al., 2017).

Background

Macroscopic space weathering is the primary means by which rocks on the lunar surface break down over time due to a lack of atmospheric winds and liquid water (e.g., Hörz et al., 1975; Hörz and Cintala, 1985). The processes responsible for lunar rock breakdown are meteoroid bombardment and thermal cycling. Micrometeoroid bombardment is defined as the continual sandblasting of lunar rocks by small (~10^{-15}–10^{-3} g) meteoroids which reduce that boulder into small fragments over time (e.g., Ross, 1968; Soderblom, 1970). Larger impactors also contribute to the boulder breakdown process at the lunar surface. While larger, cm-scale impactors occur less frequently than micrometeoroid impacts, the likelihood of a larger impactor imparting a critical rupture energy on a lunar boulder is much higher. Thermal fatigue and shock are the responses of lunar boulders to the intense temperature fluctuations of the lunar day-night cycle (e.g., Molaro and Byrne, 2012; Molaro et al., 2017). Thermal fatigue results in microcrack propagation within the boulder while thermal shock is the catastrophic rupture of a boulder due to overwhelming microcrack propagation. Although described separately here, all of these breakdown processes act together as a continuum of rock fragmentation. The relative contribution of these physical breakdown mechanisms to the breakdown of lunar rocks remains a topic of ongoing research. Prior work has modelled the time required for these processes to reduce boulders on the lunar surface to fine-grained regolith (e.g., Basilevsky et al 2013; 2015; Watkins et al., 2019). Those prior studies used high resolution

LROC images to manually count the boulders present on various impact ejecta blankets and compare those distributions with the modelled age of the impact crater to establish boulder lifetimes. Results generally agree that even the largest boulders on the lunar surface should be completely broken down in no longer than ~300 Myr (e.g., Basilevsky et al., 2013; Watkins et al., 2019).

While boulders are present in other locations on the lunar surface such as rilles, wrinkle ridges, and domes, impact craters and associated ejecta blankets have been the main study sites for examining boulder populations and lifetimes on the lunar surface. Past analyses of lunar boulder breakdown have focused on ejecta deposits associated with km-scale craters largely due to the consistent presence of meter-scale boulders within them. Because the Moon lacks a meaningful atmosphere, boulders are emplaced ballistically during the impact crater formation process. The majority of boulders produced during crater formation are emplaced within ~2–3 crater radii of the parent crater in the proximal ejecta deposit, but some can be distributed several tens to hundreds of kilometers as part of the distal ejecta (e.g., Osinski et al., 2011). Furthermore, these boulders are emplaced in a pattern of gradational size with the largest boulders near the rim of the parent crater and boulder diameter subsequently decreasing in size with distance from the rim (e.g., Bart and Melosh, 2010).

The data used to assess rock populations in this work are derived products from the Miniature Radio Frequency (Mini-RF) and Diviner instruments onboard the Lunar Reconnaissance Orbiter (LRO). The Mini-RF instrument is a hybrid,

dual-polarization Synthetic Aperture Radar (SAR) that transmits a left-circular polarized signal and receives the horizontal and vertical components of that signal. Reflection of the incident, left-polarized signal from a single scattering event at the lunar surface results in a returned signal in the opposite circular (OC) polarization as transmitted. This single scattering event is referred to as specular scattering and commonly occurs in association with smooth, featureless surfaces. In contrast to specular scattering, multiple scattering events at the lunar surface commonly result in a signal polarization change to the same circular (SC) polarization as transmitted. The multiple scattering behavior is referred to as diffuse scattering, which is commonly associated with areas of the lunar surface and subsurface where wavelength-scale boulders are abundant. The SC component of the radar signal is enhanced by reflectors that are within an order of magnitude of the radar wavelength in size on the lunar surface and down to a depth of some 10× the radar wavelength (Campbell & Ulrichs, 1969). The OC component is enhanced by single reflections from relatively flat, undisturbed surfaces (i.e., the lunar soil-atmosphere horizon). A comparison of these components will reveal the relative contributions of the various scatter-causing mechanisms to the returned radar signal. Several recent studies have utilized SC and OC data from the Mini-RF instrument, specifically, to assess roughness and potential ice associated with lunar impact craters (Thompson et al., 2011; Virkki and Bhiravarasu, 2019). These data are important for the work here in that an enhanced SC component associated with the radar return at the rims of older

craters in our dataset may support our hypothesis that boulders are present at these locations for extended periods of time.

An additional radar product that we utilize in this work is circular polarization ratio (CPR) data from the Mini-RF instrument. These CPR data is the ratio of the SC and OC radar albedo. Prior studies have revealed that CPR data serve as a useful metric for assessing surface and subsurface rock populations on the Moon (e.g., Fa et al., 2011; Campbell, 2012). Given the direct and inverse dependencies on the SC and OC polarization components, respectively, a densely bouldered surface will increase CPR while a relatively smooth surface will exhibit a lower CPR. The rough surface with an abundance of surface and subsurface boulders on the scale of the S-band wavelength will exhibit a characteristically higher CPR because of the likelihood of multiple interactions at the S-band radar wavelength-scale.

The thermal infrared dataset that we use to measure rock and boulder populations in lunar ejecta deposits is rock abundance (RA) data (Bandfield et al., 2011; 2015). A derivation of thermal infrared instruments from the Diviner instrument onboard LRO, RA represents the aerial fraction of the lunar surface that is covered in rocks ~1 m in diameter. The RA model assumes input parameters of density, specific heat capacity, and thermal conductivity for a vesicular basalt (Horai and Simmons, 1972) to define a rock thermal inertia of 1570 J m^{-2} K^{-1} $s^{-1/2}$ at 200 K for the lunar surface. This thermal inertia, an emissivity of 0.95, and an albedo of 0.15 were then used to construct a rock

temperature lookup table and model the radiance of the lunar surface. Rock temperatures were binned by latitude and local lunar time and the radiance was compared for each bin. Model rock abundance was then obtained by minimizing the root mean squared error between the measured and model radiance values. Rock abundance ranges from 0.05–0.1 (5–10%) on the lunar maria but can theoretically reach values of 1 (100%) where surface rocks comprise the entire lunar surface (Bandfield et al., 2011, 2015). Both the Mini-RF radar and Diviner RA data are publicly available in global mosaic form from the University of Washington, St. Louis Planetary Data System Geosciences node (https://pds-geosciences.wustl.edu/missions/lro/).

In order to compare the age of craters to their boulder populations, ages for the associated impact craters must first be established. The crater ages used in this work were modelled from topographic degradation state in Fassett and Thomson (2014; hereafter referred to as FT2014). In that study, the authors extracted topographic profiles from ~13,000 km-scale impact craters on the lunar maria in the size range of ~0.8–5.0 km from topography data from Kaguya's Terrain Camera (Haruyama et al., 2012). They fit these topographic profiles to a diffusion model to assign topographic degradation states for each crater in their dataset, κt, where κ represents the integrated diffusivity experienced and t represents the time exposed on the Moon. The degradation states were then calibrated to absolute ages by calculating the local crater density of the surface they were exposed on in moving neighborhoods of 50 km radius. The result of

this algorithm is a sample set of ~13,000 simple impact craters on the lunar maria with unique degradation states and modelled age values. This degradation model is based on the premise that the features of a fresh impact crater become topographically muted over time due to the downslope motion of the overlying regolith. Until recently, the downslope motion of the regolith covering the crater rims and interior walls has been attributed to ejecta splashing from subsequent primary impactors. The FT2014 crater dataset was recently updated to account for anomalous diffusion (Fassett et al., 2018a). Anomalous diffusion is defined as the combination of small, primary impacts and distal, secondary impacts into a pre-existing, larger impact structure with a net downslope ejecta distribution that subsequently flattens topographic slopes over time (Speyerer et al., 2016; Fassett et al., 2018a; Minton et al., 2019). This update corrected the individual κt values to account for the size-dependence of topographic diffusion by normalizing the diffusion model to a 1-km crater diameter. This is an improvement on the prior description of the crater degradation process (e.g., Xie et al., 2017) and is necessary to reconcile crater degradation with the observed equilibrium size-frequency distributions observed on the lunar surface (Minton et al., 2019). Seismic shaking may also contribute to the process of topographic degradation. However, prior work has demonstrated that seismic shaking, when compared to the process of ballistic sedimentation-driven diffusion, is likely a secondary process in topographic degradation on the Moon (Fassett et al., 2011).

Methods

The sample set of craters used for this study consists of those craters from the FT2014 and Fassett et al., 2018 database convolved with Mini-RF data coverage (6,221 craters) and Diviner RA data coverage (6,240 craters). This slightly larger sample set of craters measured in the RA data is due to better RA data coverage over the lunar mare (Fig. 1.2). Using ArcMap 10.6, the center points of these craters were overlain as a single shapefile onto the Mini-RF CPR, SC and OC radar albedo, and Diviner Rock Abundance global mosaics (Fig. 1.3). Because the Mini-RF and Diviner RA mosaics exhibit imperfect selenodetic control with the LROC WAC basemap, offsets no greater than ~1.0 km existed between the WAC, RA, and radar mosaics. To correct for these offsets and ensure consistent annular zone boundaries, all center points were manually re-referenced to the geographic centers of the respective crater in each dataset. The ArcMap Zonal Statistics tool was then used to extract average CPR, SC, OC, and RA values associated with the crater rims (1.0–1.5 crater radii) and proximal ejecta deposits (1.5–4.0 crater radii) of each crater.

Results

Our zonal statistics characterization algorithm includes mean, median, and percentile values of CPR and RA data for all impact craters in our dataset. A direct comparison of all individual impact craters in these datasets is unlikely to reveal clear trends due to noise in the Mini-RF CPR and Diviner RA datasets as well as the error that is inherent in the FT2014 diffusion model ages. This

uncertainty, specifically the noise inherent in CPR measurements, has been documented in prior work (Ghent et al., 2016; Fassett et al., 2018; Nypaver et al., 2019). Therefore, we advise caution in using these methods of correlating remote sensing data and age as a means of establishing an independent age-dating method for individual craters. To mitigate this noise and provide a clearer understanding of the erosional processes occurring at lunar impact craters, we bin the crater data values in 1000 κt increments and plot those bins as a function of increasing age.

For both crater rims and ejecta deposits, binned CPR and RA values generally tend to decrease over time (Fig. 1.4). Moreover, CPR and RA mean and median values associated with crater rims were elevated above ejecta deposit values for every crater bin over the lifetime of the lunar maria. To further characterize the observed trend, we used the York Method (York et al., 2004) to identify the least-squares fit line accounting for uncertainty in both CPR and RA. The slopes of the mean RA data for crater rims and ejecta (Fig. 1.4d) are distinguishable from each other (Table 1.1). Moreover, the slopes of the crater rim means in both data sets are statistically separable from zero. A difference of means test for all CPR and RA data bins indicates a higher degree of difference between the RA ejecta and rim data bins <0.6 Ga. The crater rim values reach a steady-state increase over the ejecta at ~2.0 Ga in both datasets. The difference between crater rim and ejecta values at the beginning of a crater's lifetime is ~0.06 in RA and ~0.1 in CPR. This difference in crater rim and ejecta RA and

CPR decreases by ~60% and ~30% over the lifetime of the lunar mare, respectively.

An analysis of Mini-RF SC radar albedo for the same crater bins from Fig. 1.5 reveals a similar trend to that of CPR and RA data with average SC albedo values decreasing over time (Fig. 1.5b). A similar relationship also exists in the evolution of SC albedo in that the impact crater rim SC values are elevated above the ejecta SC values for every bin in our dataset. A direct comparison of the crater rim and ejecta SC and OC radar albedo reveals separate trends both in slope and data distribution for those data bins (Fig. 1.5a). For Fig. 1.5a, we derived a linear fit using the York method and found that the rim data is best fit by a line of slope 1.03 ± 0.75, while the ejecta data is best fit by a line of slope 1.52 ± 1.78. Thus, while for the rim SC data provides information for the prediction of OC data and a positive linear correlation exists, within error ejecta SC values do not provide information for the prediction of ejecta OC values (i.e., the null hypothesis, that of a zero slope, cannot be ruled out). Our derived trend for crater rims is similar to that found by Virkki and Bhiravarasu (2019) for crater interiors and supports our interpretation of wavelength-scale scatterers on crater rims. The lack of a statistically robust trend for the ejecta SC and OC albedo values, along with their overall low albedo values compared to the rim, agrees with our interpretation of significant processing of wavelength-scale scatterers within the ejecta over time.

Discussion

We interpret the data presented in Figs. 1.4–1.5 to indicate that boulders are present at the rims of impact craters on the lunar maria, not only during the early stages of an impact crater's existence on the lunar surface, but throughout the lifetimes of most craters in our dataset. Decreasing trends are observed for the RA and CPR data associated with impact crater rims and ejecta deposits as a function of time. Those trends indicate that surface and subsurface rocks at crater rims and ejecta deposits are breaking down over time. Decreasing differences between crater rim and ejecta data with time indicate that a steady state rock population may be reached at crater rims within ~2.0 Byr. That steady state rock population is then retained at crater rims for the duration of that crater's lifetime. The smaller difference between mean CPR ejecta and rim data slope relative to RA mean data is likely due to the sensitivity of the CPR data to subsurface rocks at the scale of the S-band wavelength. Though, this increased indifference in trend slope and the increased CPR standard deviation may also be attributable to the low signal-to-noise of the Mini-RF monostatic data. Without this sensitivity, the RA data show an increased disparity between crater rim and ejecta surface rock populations. The separation of impact crater rim and ejecta SC data is in agreement with the analysis of CPR and RA data and strongly supports the hypothesis that meter-scale boulders are present at impact crater rims for prolonged periods of time.

A direct comparison of crater rims and ejecta in Mini-RF SC and OC data (Fig. 1.5a) reveals distinct trends for these regions in both datasets. We base our interpretations of these trends on prior modelling of SC and OC scattering behaviors (Virkki and Bhiravarasu, 2019). Those authors utilized a discrete dipole approximation code to create a 4×4 covariance scattering matrix that approximates the effects of particle size, size distribution and refractive index on radar scattering. Their model held two of those variables constant while altering the third to show the effects of each. The results of those experiments indicate that an increase in wavelength scale scattering particles increases the backscattering enhancement factor and the overall length of the data distribution in a plot of SC and OC data. Furthermore, the slope of the data distribution best-fit line decreases with increasing backscattering enhancement factor. Based on that model, we infer that the increased distribution of binned crater rim data observed in our data is indicative of an increased number of wavelength-scale scatterers at crater rims. Moreover, the low SC and OC radar albedo values for the ejecta data is indicative of evolution towards a more porous regolith and increased cobble roundness in the ejecta with time (Fig. 1.5a). These interpretations are consistent with a higher degree of overturn in the regolith and boulder presence at crater rims.

Based on these results, we suggest that surface rock populations are maintained at simple crater rims by ongoing exhumation. This interpretation is not contradictory to earlier observed rates of boulder breakdown inferred from

boulder counting methods. Rather, we suggest that mass wasting at crater rims occurs at a rate that exceeds the previously established rates of boulder breakdown. Mass wasting is, therefore, a dominant control on surface rock populations in that narrow annular zone. Prior work has shown that mass wasting processes are active on the lunar surface (e.g., Xie et al., 2017; Fassett and Thomson, 2014; Minton et al., 2019). It has also been shown that, over time, regolith from impact crater rims will incrementally fill crater interiors, initially producing an increasing CPR signature in the crater interior for the first billion years, that then declines (Fassett et al., 2018b). Based on these prior studies and our findings in Figs. 1.4 and 1.5, we infer that subsurface rocks at impact crater rims are continually being uncovered as the overlying regolith migrates downslope into the crater interior of the crater ejecta. Some combination of past seismic activity and anomalous diffusion is the likely cause of the downslope motion of regolith from crater rims and is the same mechanism responsible for the topographic degradation of km-scale lunar craters and topography as a whole. At impact crater rims, anomalous diffusion and regolith transport must occur at a rate that exceeds the rate of regolith production, or at least the time it takes to break down exhumed rocks to scales smaller than detectable in the radar and RA datasets.

Conclusions

In this work we show that boulders are present at crater rims for prolonged periods of time, and we attribute their presence to rapid downslope transport of

surface regolith. This conclusion is supported by both radar (CPR, SC, and OC) and thermal infrared (RA) remote sensing datasets. Qualitatively, large boulders are still observed at the rims of old, km-scale craters in LROC NAC images, and a visual crater rim/ejecta boulder dichotomy was reported by Schmitt et al., (2017) using Apollo 17 photographs (Fig. 1.6).

In a re-analysis of Taurus Littrow valley geology, it was noted that there was a clear dichotomy between rock populations at the crater rim and in the ejecta deposit (Schmitt et al., 2017; Fig. 1.6). Those authors also cited a mechanism of continual regolith removal and rock exposure at the crater rim to explain their observations. It was also noted that the observed rocks at crater rims are likely to be in-situ, meaning that they underwent minimal transportation during the formation of the parent crater.

With the exception of several drill core samples from the Apollo and Luna programs, all lunar rock and soil samples were collected at the lunar surface where loose rocks were easily attainable. As previous work has shown, rocks at the lunar surface are mostly composed of ejecta material that has the capability to travel great distances from the parent crater during the crater formation process (e.g., Dundas and McEwen, 2007). Hence, one ongoing challenge in our understanding of lunar surface ages and composition lies in the assumption that our lunar samples were all relatively in situ at the time of collection. Attempts have been made to disentangle the source of lunar samples and mitigate the potential for distal source contamination, but if this assumption is incorrect and

the samples that we have were transported from other areas of the Moon, some aspects of our understanding of lunar chronology and petrologic evolution may be flawed. The demonstration that rocks are exhumed over long periods of time at km-scale crater rims implies that those rocks being uncovered are locally derived. This finding provides a vital piece of information for future lunar sample return missions for which in-situ samples are desired for accurate chronological and petrological characterizations of the lunar surface units.

References

Bandfield, J. L. et al. (2015), Lunar surface roughness derived from LRO Diviner radiometer observations. *Icarus*, 248, 357–372.

Bandfield, J. L. et al. (2011), Lunar surface rock abundance and regolith fines temperatures derived from LRO Diviner Radiometer data. *Journal of Geophysical Research*, 116, E00H02.

Bart, G., & H. Melosh (2010), Distributions of boulders ejected from lunar craters. *Icarus* (New York, N.Y. 1962), 209(2), 337–357. https://doi.org/10.1016/j.icarus.2010.05.023.

Basilevsky, A. T. et al. (2013), Survival times of meter-sized boulders on the surface of the Moon, *Planetary and Space Science*, 89, 118-126

Basilevsky, A. T. et al. (2015), Survival times of meter-sized rock boulders on the surface of airless bodies. *Planetary and Space Science*,117, 312–328.

Basilevsky, A. T. et al. (2018), Rock spatial densities on the rims and interiors of a group of Copernicus secondary craters. *Planetary and Space Science,*172, 14-21.

Cahill, J. S. et al. (2014), The miniature radio frequency instrument's (Mini-RF) global observations of Earth's Moon. *Icarus,* 243, 173–190.

Campbell, B. A. (2012), High circular polarization ratios in radar scattering from geologic targets. Journal of Geophysical Research, 11, E06008.

Campbell, M., & J. Ulrichs (1969), Electrical properties of rocks and their significance for lunar radar observations. *Journal of Geophysical Research*, 74(25), 5867–5881. https://doi.org/10.1029/JB074i025p05867

Craddock, R., & A. Howard (2000), Simulated degradation of lunar impact craters and a new method for age dating farside mare deposits. *Journal of Geophysical Research. Planets*.

Dundas, C. M., & A. S. McEwen (2007), Rays and secondary craters of Tycho. Icarus, 186, 31– 40.

Fassett, C. et al. (2011), Thickness of proximal ejecta from the Orientale Basin from Lunar Orbiter Laser Altimeter (LOLA) data: Implications for multi-ring basin formation. *Geophysical Research Letters,* 38(17). https://doi.org/10.1029/2011GL048502

Fassett, C. I. & B. J. Thomson (2014), Crater degradation on the lunar maria: Topographic diffusion and the rate of erosion on the Moon. *Journal of Geophysical Research: Planets*, 119, 2255–227.

Fassett, C. I. et al. (2018a), Re-analysis of observations of crater degradation on the lunar maria accounting for anomalous diffusion. *Lunar Planet. Sci. Conf. 49th*, abstract 2083.

Fassett, C. I. et al. (2018b), Temporal evolution of S-band circular polarization ratios of kilometer-scale craters on the lunar maria. *Journal of Geophysical Research: Planets*, 123, 3133– 3143.

Gault, D. et al. (1972), Effects of microcratering on the lunar surface, *Geochem. Cosmochem A. cta, Suppt,* 3, 2713-2734.

Ghent, R. R. et al. (2014), Constraints on the recent rate of lunar ejecta breakdown and implications for crater ages. *Geology*, 42, pp. 1059-1062.

Ghent, R. R. et al. (2016), Lunar crater ejecta: physical properties revealed by radar and thermal infrared observations. *Icarus*, 273 pp. 182-195.

Haruyama, J., et al. (2012), Lunar global digital terrain model dataset produced from Selene (Kaguya) Terrain Camera stereo observations, *43rd Lunar Planet. Sci. Conf.,* 1200.

Horai, K. I. & G. Simmons (1972), Thermal property measurements on lunar material returned by Apollo 11 and 12 missions, Progress Astronaut. *Aeronaut*., 28, 243–267.

Hörz, F. et al. (1971), Micrometeorite craters on lunar rock surfaces. *Journal of Geophysical Research,* 76(23), 5770–5798. https://doi.org/10.1029/JB076i023p05770

Li, Y. et al. (2018), Correlations between ejecta boulder spatial density of small lunar craters and the crater age. *Planetary and Space Science*, 162, 52–61. https://doi.org/10.1016/j.pss.2017.08.007

Mazrouei, S., et al. (2019), Earth and Moon impact flux increased at the end of the Paleozoic. *Science*, 363(6424), 253–257.

Minton, D., et al. (2019), The equilibrium size-frequency distribution of small craters reveals the effects of distal ejecta on lunar landscape morphology. *Icarus* (New York, N.Y. 1962), 326, 63–87. https://doi.org/10.1016/j.icarus.2019.02.021

Molaro, J., & S. Byrne (2012), Rates of temperature change of airless landscapes and implications for thermal stress weathering. *Journal of Geophysical Research: Planets*, 117(E10). https://doi.org/10.1029/2012JE004138

Molaro, J. L. et al. (2017), Thermally induced stresses in boulders on airless body surfaces, and implications for rock breakdown. *Icarus*, 294, 247-261.

Neish, C., et al. (2013), A comparison of rayed craters on the Moon and Mercury. *Journal of Geophysical Research: Planets*, 118(10), 2247–2261. https://doi.org/10.1002/jgre.20166

Nypaver, C. N. (2019), Deriving lifetimes of lunar ejecta constituents: A model for lunar erosion and regolith overturn. Master's Thesis, University of Tennessee, 2019. https://trace.tennessee.edu/utk_gradthes/5500

Osinski, G., et al. (2011), Impact ejecta emplacement on terrestrial planets. *Earth and Planetary Science Letters,* 310(3-4), 167–181. https://doi.org/10.1016/j.epsl.2011.08.012

Raney, R. K. et al. (2011), The lunar Mini-RF radars: Hybrid polarimetric architecture and initial results, *Proc. IEEE*, 99(5), 808–823, doi:10.1109/JPROC.2010.2084970.

Robbins, S. J. et al. (2014), The variability of crater identification among expert and community crater analysts. *Icarus*, 234, 109–131. https://doi.org/10.1016/j.icarus.2014.02.02210.1029/2020JE006400

Ross, H. P. (1968), A simplified mathematical model for lunar crater erosion. *Journal of Geophysical Research*. 73, 1343–1354.

Schmidt, R., & K. Housen (1987), Some recent advances in the scaling of impact and explosion cratering. *International Journal of Impact Engineering*, 5(1), 543–560. https://doi.org/10.1016/0734-743X(87)90069-8

Schmitt, H., et al. (2017), Revisiting the field geology of Taurus–Littrow. *Icarus*, 298, 2–33. https://doi.org/10.1016/j.icarus.2016.11.042

Soderblom, L. A. (1970), A model for small-impact erosion applied to the lunar surface. *Journal of Geophysical Research.* 75, 2655–2661, doi:10.1029/JB075i014p02655.

Speyerer, E. et al., (2016), Quantifying crater production and regolith overturn on the Moon with temporal imaging. *Nature* (London), 538(7624), 215–218. https://doi.org/10.1038/nature19829

Stoffler, D. (2006), Cratering History and Lunar Chronology. *Reviews in Mineralogy and Geochemistry,* 60(1), 519–596. https://doi.org/10.2138/rmg.2006.60.05

Thompson, T. et al. (2011), Modeling radar scattering from icy lunar regoliths at 13 cm and 4 cm wavelengths. *Journal of Geophysical Research: Planets*, 116(E1). https://doi.org/10.1029/2009JE003368

Vickery, A. (1986). Size-velocity distribution of large ejecta fragments. *Icarus* 67 (2), 224–236.

Virkki, A. & Bhiravarasu, S. (2019), Modeling Radar Albedos of Laboratory-Characterized Particles: Application to the Lunar Surface. *Journal of Geophysical Research: Planets*, 124(11), 3025–3040. https://doi.org/10.1029/2019je006006

Wang, J. et al., (2020), Quantitative Characterization of Impact Crater Materials on the Moon: Changes in Topographic Roughness and Thermophysical Properties with Age. *Journal of Geophysical Research: Planets,* 125(10). https://doi.org/10.1029/2019JE006091

Watkins, R., et al. (2019), Boulder Distributions Around Young, Small Lunar Impact Craters and Implications for Regolith Production Rates and Landing Site Safety. *Journal of Geophysical Research: Planets,* 124(11), 2754–2771. https://doi.org/10.1029/2019je005963

Xie, M. et al. (2017), Effect of Topography Degradation on Crater Size-Frequency Distributions: Implications for Populations of Small Craters and Age Dating: Effect of Topography Degradation on CSFD. *Geophysical Research Letters*, 44(20), 10–10,179. https://doi.org/10.1002/2017GL075298

York, D. et al. (2004), Unified equations for the slope, intercept, and standard errors of the best straight line. *American Journal of Physics,* 72(3), 367–375. https://doi.org/10.1119/1.1632486

Appendix

Figures

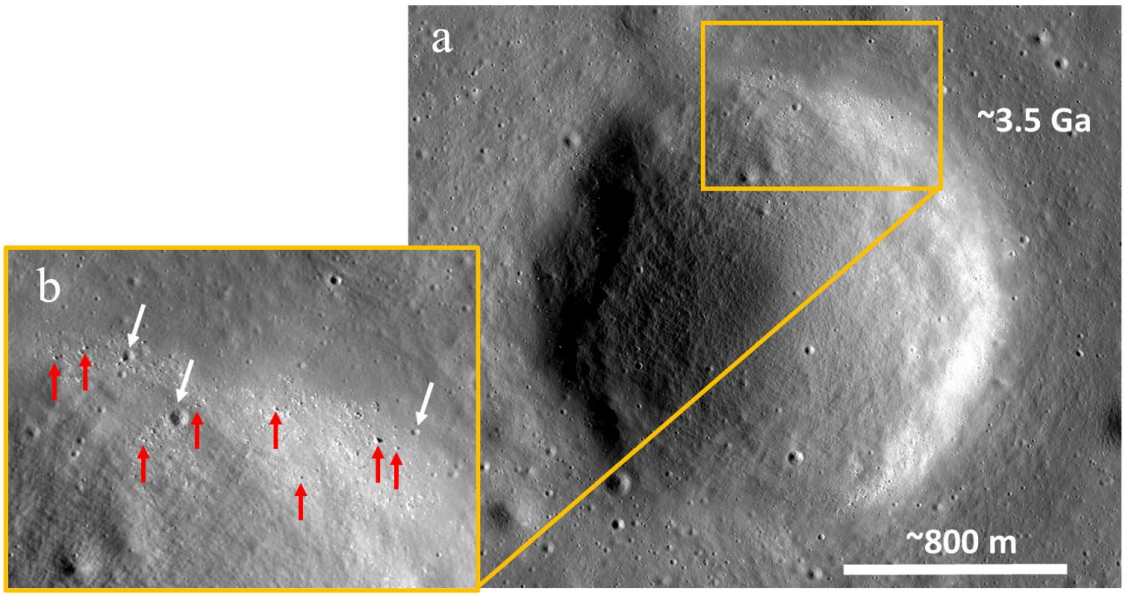

Figure 1.1. (a) LROC NAC image of a simple impact crater with a diameter of ~2.0 km on Mare Nubium (20.206° N, 9.031° E) with a modelled age of ~3.7 Ga (κt: 26203, Fassett and Thomson, 2014) and a (b) enhanced image of the NE portion of the crater rim with red arrows indicating boulders present in this region and white arrows indicating small impact craters amongst the boulders.

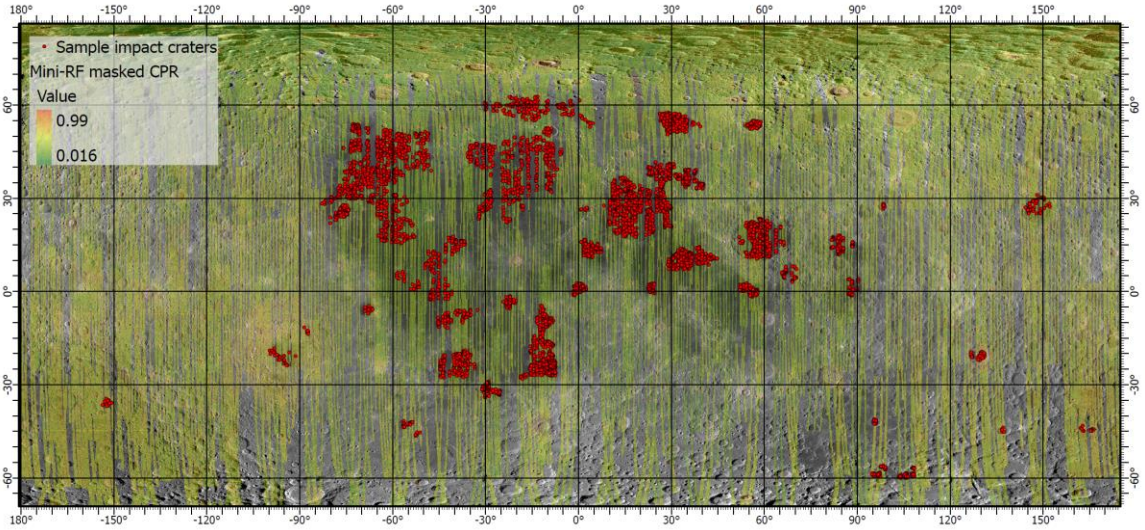

Figure 1.2. Locations of individual sample craters from the Fassett and Thomson, 2014 crater database (red points) superposed onto Mini-RF CPR and LROC WAC global mosaics.

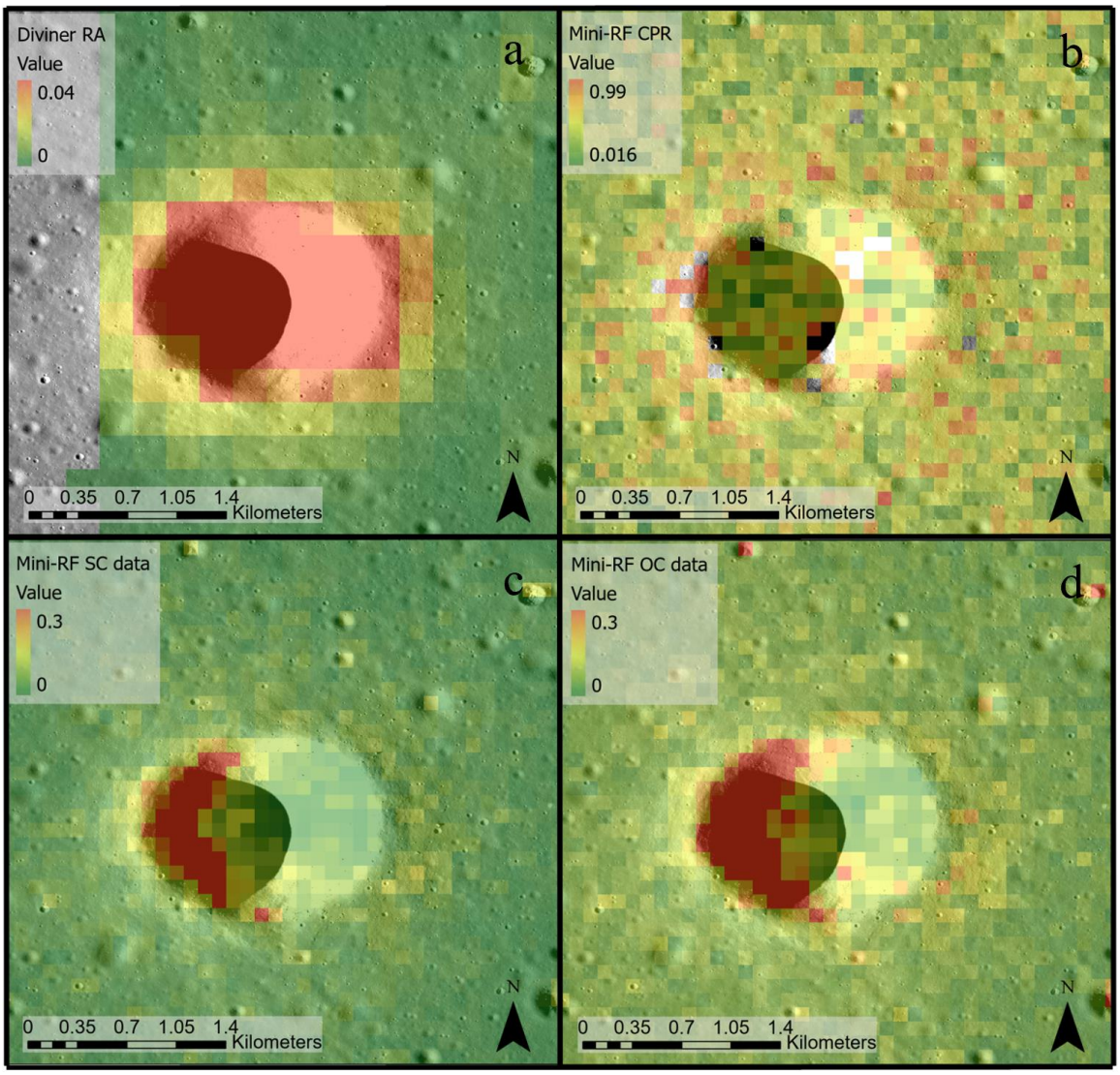

Figure 1.3. Diviner RA (a), Mini-RF CPR (b), SC (c), and OC data (d) overlaid onto an LROC NAC image of crater 8683 from the FT2014 crater database. This crater is located at 36.86° N, -15.9° E with a diameter of ~1.37 km and a modelled age of ~0.02 Ga

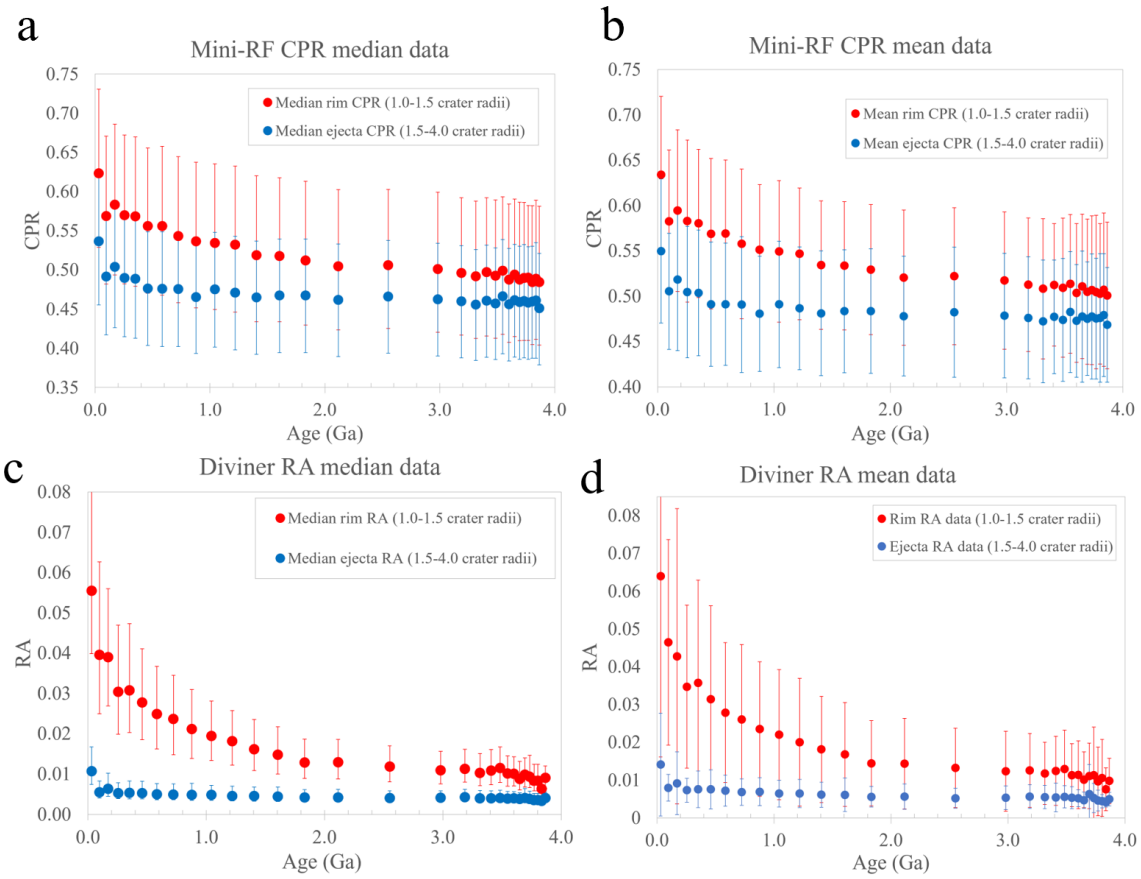

Figure 1.4. Binned CPR (a-b) and RA (c-d) median and mean values associated with the crater rim region (red points) and ejecta (blue points) shown as a function of increasing age. RA data associated with the crater rims is substantially decoupled from ejecta RA data (c-d) whereas the CPR signatures of crater rims and ejecta are within error of one another (a-b). In both datasets, the crater rims appear elevated above the ejecta for the lifetime of most craters in our dataset. Error bars in Figs. 1.4a and 1.4c represent the 25th and 75th percentile data values of the respective bins whereas error bars in figs. 1.4b and 1.4d represent standard deviations. A comparison of our Diviner RA mean results with the crater rim (green diamonds) and ejecta (yellow diamonds) RA values associated with a subset of the smaller (<30 km) impact craters sampled in Ghent et al., (2014; 2016) is also given (e). That comparison yields similar trends to those observed in our own results where crater rim RA values are elevated above the ejecta and all RA values decrease with time.

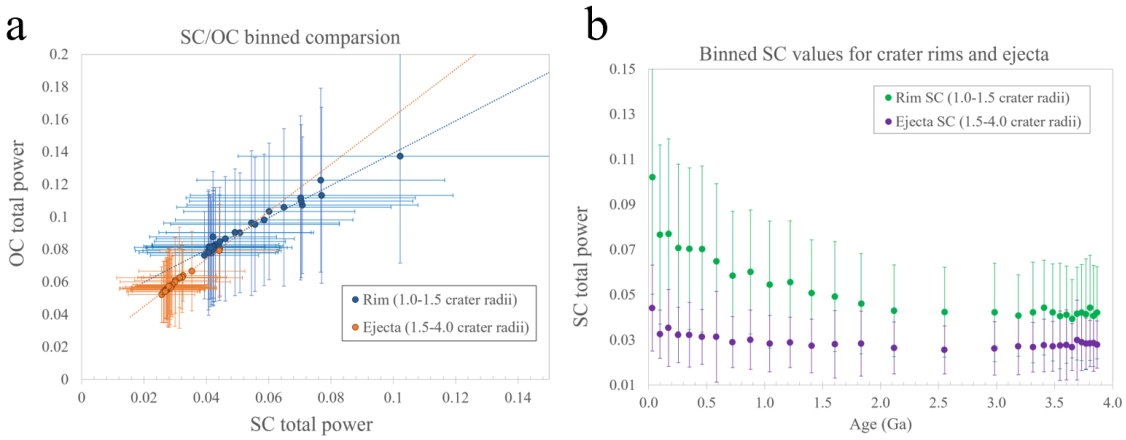

Figure 1.5. Binned SC (Same-sense radar albedo) for the same crater bins presented in Fig. 1.4 as a function of increasing age (a) and direct comparison of SC and OC radar albedo for those same bins. The SC data associated with the crater rims in (b) shows a similar trend to the RA and CPR data in Fig. 1.4 and is substantially decoupled from ejecta SC data. Based on the modeling results

Figure 1.6. (Fig. 18 in Schmitt et al., 2017) Apollo 17 photograph taken by Astronaut Gene Cernan from the perspective of the rim of Camelot crater looking out into the associated ejecta deposit. A dichotomy is observed between the boulder population at the crater rim and in the ejecta deposit. NASA Photograph

Tables

Table 1.1. York fit slope values for the overall trends of binned CPR and RA mean values as a function of age (Figs. 1.3b and 1.3d.).

	Ejecta data slope	Rim data slope
RA	-0.001±0.000	-0.006±0.002
CPR	-0.008±0.009	-0.022±0.011

CHAPTER TWO : NEW OBSERVATIONS OF RECENTLY ACTIVE WRINKLE RIDGES ON THE LUNAR MARE: IMPLICATIONS FOR THE TIMING AND ORIGIN OF LUNAR TECTONICS

A version of this chapter has been published in Geophysical Research Letters by Cole A. Nypaver and Bradley J. Thomson

Nypaver, C. and B. J. Thomson (2022). New observations of recently active wrinkle ridges in the lunar mare: Implications for the timing and origin of lunar tectonics. Geophysical Research Letters, e2022GL098975. https://doi.org/10.1029/2022GL098975.

This text has been modified from its originally published form to include additional background information on lunar tectonism and compressional tectonic features at the lunar surface.

Abstract

The variety of tectonic features on the Moon indicates that the lunar lithosphere has undergone a complex deformational history. Lobate scarps and wrinkle ridges are two such tectonic features that have resulted from compressional stresses. The crisp morphologies and cross cutting relations associated with a global population of lobate scarps have been cited as evidence for their recent (<1.0 Ga) formation, but observations of recently active wrinkle ridges have not been made on a similar scale. Here, we present new observations of 1,116 recently active (~0.056–1.5 Ga) wrinkle ridge segments on the lunar maria. Our results indicate that clusters of recently active wrinkle ridges are distributed across ~90% of nearside mare basins. Spatial correlations were noted between wrinkle ridge orientations with predicted stress fields from both orbital recession and global contraction as well as ongoing reactivation of a residual set of structures associated with the South Pole–Aitken basin.

Introduction

The surface of the Moon boasts an array of tectonic features. Compressional stresses acting on the lunar lithosphere have manifested in the form of lobate scarps and wrinkle ridges across the lunar highlands and mare (e.g., Schultz, 1976; Watters, 1988; Watters, 2022). Evidence for the recent displacement and formation of lunar lobate scarps has been put forth in the form of crosscutting relations with other, young lunar surface features (e.g., Binder, 1982; Watters et al, 2010; 2012) as well as absolute model ages derived from buffered crater counting over those scarps (Clark et al., 2017; Van der Bogert et al., 2018). The global distribution and non-random orientations of lunar lobate scarps have indicated that some combination of orbital recession, global contraction, and solid-body tidal stresses are at work in deforming the lunar lithosphere on a global scale (e.g., Watters et al., 2010; 2015; Banks et al., 2012).

Compared to the near-global distribution of lobate scarps, wrinkle ridges on the lunar surface exist primarily in the lunar maria (e.g., Schultz, 1976; Melosh, 1978; Watters et al., 2022). Early wrinkle ridge formation in the lunar maria resulted from the isostatic response of the lunar lithosphere to the voluminous outpouring of mare basalt deposits onto the lunar surface (e.g., Melosh, 1978; Whitaker, 1981; Wilhelms, 1987; Yue et al., 2015; Thompson et al., 2017). The formation of those early wrinkle ridges followed a predictable geometric pattern in which linear wrinkle ridges formed in radial and concentric patterns away from the mascon center (e.g., Melosh, 1978; Solomon and Head, 1980; Freed et al.,

2001). Morphologically, most wrinkle ridges exhibit increased lengths, widths, and topographic relief relative to lunar lobate scarps.

The regional distribution and ages of those larger, mascon-induced wrinkle ridges have been analyzed using Lunar Reconnaissance Orbiter Camera (LROC) Wide Angle Camera (WAC) data with an image resolution of 100 m/pixel (Yue et al., 2015; 2017; Li et al., 2018; Schleicher et al., 2019). Recent work has also successfully utilized rock abundance data derived from LRO Diviner instrument thermal data to identify a network of recently active wrinkle ridges on the lunar nearside (Bandfield et al., 2011; Valantinas and Schultz, 2020). However, the resolution of the rock abundance dataset is coarser (237 m/pixel) than that of the LROC WAC image data. The use of those coarse resolution data in prior work prohibited the observation of any smaller, decameter-wide wrinkle ridges that may be below the resolution of the LROC WAC and Diviner rock abundance datasets. The omission of small, recently active wrinkle ridges from past work has the potential to introduce a sampling bias into the understanding and timing of wrinkle ridge formation and global stress mechanisms acting on the lunar lithosphere.

Several recent studies have identified subsets of recently active wrinkle ridges that do not follow the established hypothesis of mascon tectonism (e.g., Williams et al., 2019; Lu et al., 2019; Früh et al., 2021; Clark et al., 2022). These narrow (~100–300 m) ridges are located in isolated regions of Mare Frigoris, Mare Serenitatis, and Mare Imbrium, crosscut decameter-scale impact craters,

and display crisp, uneroded morphologies in high-resolution LROC NAC images – potentially indicating recent formation or reactivation by localized, late-stage mare cooling (Lu et al., 2019) or lunar global contraction (Williams et al., 2019). However, those studies present isolated results over only a small percentage of the nearside mare.

Until now, interpretations regarding global stress mechanisms currently acting on the lunar lithosphere have been primarily derived from observations and measurements of lobate scarps in the lunar highlands and large-scale wrinkle ridges in the nearside lunar mare. Here, we present some of the first observations of small, recently active wrinkle ridges across ~90% of the lunar nearside mare. Our work therefore stands to provide a more spatially comprehensive understanding of stress mechanisms that are responsible for recent deformation of the lunar surface and lithosphere. This work also provides new regions of interest for a future lunar geophysical network that are advantageous to a wider variety of geologic subdisciplines.

Background

Lunar Mascon Tectonism

Thermal expansion associated with the presence of a global magma ocean early in lunar history resulted in an initially extensional global stress field (e.g., Binder, 1986; Binder and Gunga, 1985, Watters and Johnson, 2010). Such an extensional stress field resulted in the formation of linear and arcuate rilles with formation mechanics similar to those of structural graben (e.g., McGill, 1971;

Lucchitta and Watkins, 1978, Golombek, 1979). The formation of those extensional features ceased at approximately ~3.6 Ga — as evidenced by the presence of rilles in only the oldest mare units and lunar highlands (e.g., Luchitta and Watkins, 1978; Solomon and Head, 1979). The lack of extensional features in any lunar terrains younger than ~3.6 Ga is attributed to a global shift in stress state from net expansion to net contraction (e.g., Solomon and Head, 1980). This shift in stress state also coincides with the most intense period of lunar mare formation and the onset of mascon tectonism on the Moon (e.g., Luchitta and Watkins, 1978; Melosh, 1978).

The prolonged infilling of nearside lunar impact basins by the lunar mare basalts over the majority of lunar history (~1.2–4.0 Ga; Hiesinger et al., 2011) resulted in isolated rheologic loads across the lunar nearside. The resulting mass concentrations (“mascons”) within preexisting impact basins provoked an isostatic response from the underlying lithosphere in which the outer layers of the Moon deformed elastically to accommodate for the increased surface mass (e.g., Melosh, 1978; Solomon & Head, 1980; Freed et al., 2001). The concave geometry of the embayed impact basins led to thicker mare basalts, and thus, increased mass at the center of the basins. The contractional stress fields that stemmed from the mascon-related lithospheric subsidence formed a pattern of radial and concentric wrinkle ridges within the mascon basin that radiated away from the basin center (e.g., Whitaker, 1981; Watters and Johnson, 2010). It is worth noting that while contractional features are the dominant landform

associated with this rheological model of mascon loading, extensional features are predicted and observed to occur concentrically at the edge of the mascon basin and in the surrounding highlands terrain (e.g., Melosh, 1978). The concentric nature of mascon wrinkle ridge populations also serves as evidence of structural control from pre-existing basin-concentric ring systems that underlie the mare basalts (e.g., Watters and Johnson, 2010). Recent and ongoing efforts to establish relative and absolute model ages for basin concentric wrinkle ridges have indicated that wrinkle ridge formation generally began at the distal edges of the basin — where the basalts are structurally thinner — and progressed inward (e.g., Yue et al., 2019; Frueh et al., 2022). The onset of wrinkle ridge formation in mascon settings was generally coincident with the most intense period of mare formation (~3.6–3.1 Ga) and ceased no sooner than ~1.2 Ga.

The wrinkle ridges that formed via mascon loading are large relative to other tectonic features on the lunar surface. The largest lunar wrinkle ridges are <20 km in width and <300 km in length with several hundred meters of relief. A broad, topographic arch and a superimposed central ridge structure comprise the morphology of most large lunar wrinkle ridges (e.g., Plescia & Golombek, 1986; Strom, 1972; Watters, 1988; Watters et al., 2022; Frueh et al., 2023). The central ridge structure can be described as a linear structure with two bounding scarps and an uplifted, flat, or pseudo-flat ridge crest. The steeper of the two bounding scarps is typically associated with the vergent side of the ridge, but reversals in vergence along strike are common for lunar wrinkle ridges (e.g., Plescia &

Golombek, 1986). Smaller, secondary ridges are commonly found parallel to or atop the central, primary ridge structure (e.g., Frueh et al., 2022). The arcuate nature of the central ridge and bounding scarps is likely the result of structural control from underlying impact craters that pre-date the emplacement of the mare basalts (e.g., Watters and Johnson, 2010).

The understanding of subsurface structure associated with large lunar wrinkle ridges is limited to coarse resolution seismogram data from the Apollo Lunar Sounder Experiment (ALSE) and dislocation modeling. ALSE data over a larger wrinkle ridge in Mare Serenitatis appear to indicate that interbedded basalt layers have been folded upward to form the central ridge structure (e.g., Phillips et al., 1973; Peeples et al., 1978; Maxwell and Phillips, 1978). The folded beds dip away from the uplifted central ridge in both directions along strike. Moreover, the observed interbeds appear to be structurally thinner at the ridge crest and progressively thicken with distance from the ridge. Past models of subsurface fault structure combine an assumed fault dip angle with maximum relief of the ridge in question to estimate the maximum ridge displacement (e.g., Watters et al., 2004; Watters and Johnson, 2010). Those models approximate well the displacement along smaller lunar lobate scarps, but they typically fail to reproduce the complex geometries associated with larger lunar wrinkle ridges and the associated topographic arch. More recent modeling has found that the observed topography associated with lunar wrinkle ridges is best replicated by a blind listric fault that shallows continuously into a flat decollement at depth that is

proportional to the maximum relief of the wrinkle ridge in question (Watters, 2022).

Lunar Lobate Scarps

Another more recently identified class of tectonic features on the lunar surface are lobate scarps. Lobate scarps were first identified in Apollo photographs as contractional features with a smaller geometry relative to mare-located wrinkle ridges (e.g., Schultz, 1976). Lobate scarps are typically <20 km in length, less than several hundred meters in width, exhibit <150 m in relief, and are observed to exist predominantly in the lunar highlands (e.g., Banks et al., 2012; Williams et al., 2013). One popular exception to the omnipresence in the lunar highlands is the Lee-Lincoln scarp which crosscuts mare basalts in the Taurus-Littrow valley and was the subject of investigation by the Apollo 17 astronauts (e.g., Schmitt and Cernan, 1973; Schmitt et al., 2017). Hence, lobate scarps are also observed on the mare-highlands boundaries. The cross-sectional morphology of lunar lobate scarps includes an asymmetric topographic rise with a single steeply sloping scarps and a shallow sloping back limb (e.g., Banks et al., 2012). Dislocation modeling was employed to determine the best-fit fault geometry to that topographic profile (Williams et al., 2013). Results of that investigation indicated that subsurface fault dip angles associated with lobate scarps range from 35°–40°, depth of faulting ranged from 220–900 m, and fault slip ranges from 18–62 m.

Lobate scarps are interpreted to be Copernican in age based on their small scale and generally crisp morphology (e.g., Watters et al., 2010; Watters et al., 2015). Given their global presence in lunar highlands terrain, which has undergone continuous bombardment and overturn since lunar formation, it is difficult to ascertain whether any lobate scarps pre-date that Copernican timeframe. Several investigations have utilized buffered crater counting methods and high-resolution optical images from the Lunar Reconnaissance Orbiter Camera (LROC) to derive absolute model ages as young as ~56 Ma for highlands lobate scarps (Clark et al., 2017; van der Bogert et al., 2018). Given their youth and global distribution in the lunar highlands, it is unlikely that the same stress fields responsible for mascon tectonics and large wrinkle ridge formation are responsible for the formation of lunar lobate scarps. Recent work has estimated that a globally isotropic stress field of ~2–7 MPa would be required to induce shallow faulting in the lunar highlands (Williams et al., 2013). The stress field induced via lunar global contraction is estimated to be sufficient to induce faulting, but those isotropic stresses alone would likely result in an equally isotropic orientation pattern of the resulting tectonic features. Hence, additional stress mechanisms are necessary to explain the non-random orientation patterns of lobate scarps on a global scale (e.g., Watters et al., 2015). Stresses on the lunar lithosphere resulting from lunar orbital recession and solid body tides are insufficient in magnitude to induce shallow faulting on their own but would likely contribute to the non-random placement and orientation of any resulting tectonic

features. Stresses induced via solid body tides would have a periodized effect on the lunar lithosphere due to the Moon's non-zero eccentricity around Earth. Tidal stresses would have an enhanced effect when the Moon is at perigee and apogee in its circum-Earth orbit. Moreover, those stresses would be disproportionately enhanced at the sub-Earth and anti-Earth points on the lunar surface. The effects of orbital recession would be concentrated on the lunar nearside due to the relaxation of the nearside tidal bulge as the Moon migrates away from Earth in its orbit. At present, the accepted hypothesis for lobate scarp formation includes global contraction as a primary force responsible for the initiation of faulting, followed by orbital recession and solid body tides as lesser magnitude stress fields that control the orientation of observed lobate scarps (e.g., Watters et al. 2015). The above hypothesis is based on the measured correlation between mapped lobate scarp orientations and modelled principal stress orientations. However, recent and ongoing work has indicated that other stress fields, such as loading from SPA ejecta, may produce feature orientations similar to those mentioned above (Matsuyama et al., 2021).

Methods

We utilized NAC images from the LROC instrument in the LROC Quickmap web interface (https://quickmap.lroc.asu.edu/) to identify tectonically deformed impact craters across the lunar maria with diameters ranging from ~0.030 km to 2.0 km. The specific NAC image data used in our work consisted of an LROC Wide Angle Camera (WAC; 100 m/pixel) mosaic overlaid with large incidence

(55–80˚) NAC images (0.5–2.0 m/pixel) and NAC region of interest (ROI) mosaics (0.5–2.0 m/pixel) where available (WAC+NAC+NAC_ROI_MOSAIC toggle in the Quickmap layers menu). As the NAC mosaics are only available for specific, larger surface features, the majority of our mapping was conducted using the individual NAC image swaths. A shapefile of 11,746 previously mapped wrinkle ridges was overlain onto these image data to provide a general sense of wrinkle ridge location throughout the lunar maria (Thompson et al., 2017). The individual wrinkle ridges mapped in that work exhibit a mean length of 15.8 km and a total, combined length of 94,824 km. Those previously identified ridges were mapped in LROC WAC image data at a larger scale than that used in our methods. We manually examined each wrinkle ridge under or near to those polyline features in the Thompson et al., 2017 dataset and placed a point feature at the center of every identifiable impact crater that had been deformed in some way by a wrinkle ridge.

Impact craters were classified as tectonically deformed in our mapping if impact crater interiors were crosscut by one or both bounding scarps of a wrinkle ridge segment (Fig. 2.1). Once the craters were flagged as tectonically deformed in Quickmap, the database of deformed crater center points was exported into ESRI's ArcGIS Pro as a point shapefile. That point shapefile was then used to create a density map of deformed crater populations using the ArcGIS Kernel Density tool.

We used our point density maps of tectonically deformed impact craters to help identify isolated zones of increased tectonic activity across the lunar nearside mare. Each zone typically contained an isolated cluster of small, sinuous ridges that were responsible for the majority of crater deformation in that zone. We used the same NAC image data (0.5–2.0 m/pixel) in the LROC Quickmap interface to then map those individual ridge segments within the zones of recent activity. In order to place better temporal and spatial constraints on our database of recently active ridges, we then clipped the database of tectonically deformed craters to only those <300 m in diameter and eliminated any ridges that did not deform any craters. Hence, only the ridges with a high probability of being recently active were included in our map. While our mapping effort was conducted at a smaller scale using higher resolution image data than was used in previous wrinkle ridge analyses (e.g., Yue et al., 2015; 2017; Thompson et al., 2017), one inherent disadvantage to our methodology is that it eliminates from our database any recently active ridges that may not deform any craters due to random crater distribution statistics.

Results

Using LROC NAC images in the LROC Quickmap interface, we identified and mapped 2,277 impact craters in the diameter range of ~0.03–2.0 km on the nearside lunar mare that have been deformed by compressional tectonic activity (Fig. 2.2a). We further identified 1,116 wrinkle ridge segments distributed across 37 isolated clusters of recent tectonic activity in the nearside lunar mare (Fig.

2.2b). The mapped wrinkle ridge segments exhibit a mean length of 4.4 km and combined length of 5,070 km. The isolated zones of recent tectonic activity can be observed as areas of dense surface deformation in our crosscut crater map (Fig. 2.2b). A density map of the small, recently active wrinkle ridges shows broad similarities with the density of tectonically deformed impact craters (Fig. 2.S5). Such a correlation is expected given that the density map of tectonically deformed impact craters was used to aid in the identification of small, recently active wrinkle ridges. Morphologically, the wrinkle ridges mapped here exhibit narrow widths (~100–300 m) and relatively minimal topographic relief. In cross section, the small ridges commonly exhibit narrow central ridges with steeply sloping bounding scarps that are superposed on more broad topographic arches (Fig. 2.S6). This cross-sectional morphology is common among other lunar wrinkle ridges of varying sizes (e.g., Watters, 2022). A dendritic pattern was observed among individual ridge clusters in which narrow, sinuous ridges propagated parallel to and away from one another in a single, overarching direction (Fig. 2.3). Regionally, the small, sinuous ridges demonstrated a preferred NNW-SSE orientation at equatorial latitudes (30˚S–30˚N) that shallowed to a preferred WNW-ESE orientation at higher latitudes (30˚N–60˚N) (Fig. 2.4).

Discussion

The tectonically deformed impact craters identified in this work exhibit diameters ranging from ~0.03–2.0 km (e.g., Fig. 2.3). A previous study derived

absolute model age estimates for four tectonically deformed impact craters in this same size range using ejecta boulder size-frequency distributions and an established boulder density/age correlation equation (Li et al. 2018; Lu et al., 2019). That study established ages of $12.4 \pm^{10.7}_{10.8}$ Ma, $16.6 \pm^{10.8}_{10.8}$ Ma, $38.4 \pm^{12.7}_{12.6}$ Ma, $55.5 \pm^{6.8}_{6.8}$ Ma for four tectonically-deformed impact craters with diameters of 186 m, 227 m, 215 m, and 305 m, respectively (Lu et al., 2019 – their Figures 6-7). Those crater ages were then assigned as upper age constraints for tectonic activity associated with the small wrinkle ridges that crosscut them. We, therefore, adopt their upper age estimate (~56 Ma) as a conservative lower age estimate for the wrinkle ridge activity identified in this work. We also add that this lower age limit is further corroborated by independent observations of tectonically deformed impact craters in Mare Frigoris (Williams et al., 2019), impact crater degradation modelling (Fassett and Thomson, 2014), and prior crater degradation calibrations (Moore et al., 1980).

In order to place an upper constraint on the timing of crater deformation and wrinkle ridge activity, our database of tectonically deformed craters was clipped to only those craters that were less than ~300 m in diameter (i.e., below the resolution of the LROC WAC image dataset). An impact crater lifetime equation was then used to calculate a value of ~1.5 Ga for the lifetime of a 300 m diameter crater (Basilevsky, 1976). The spatial distribution of those small (~0.03–0.3 km diameter) tectonically deformed craters is similar to that of the overall distribution with larger (~0.3–2.0 km) craters included (Fig. 2.S7). Such a correlation

indicates that the timing of the tectonic activity identified in this work is generally consistent across the nearside mare. We therefore adopt an upper age estimate of ~1.5 Ga for the timing of wrinkle ridge activity identified here.

Our results indicate that recently active (~0.056–1.5 Ga) wrinkle ridge clusters are present in at least 37 locations across most nearside mare basins (Fig. 2.2b). Buffered crater counting methods have been used in past studies to establish absolute model ages (AMAs) for larger wrinkle ridges on the lunar surface (Yue et al., 2017), but that work grouped wrinkle ridge segments by basin for a combined age and was limited by the resolution of the LROC WAC data (100 m/pixel). The use of lower resolution data in that work resulted in the exclusion of the meter-scale wrinkle ridges and crosscut craters identified here. The derived wrinkle ridge AMAs (~3.1–3.5 Ga) were, accordingly much older than the ages inferred for the small, sinuous ridges identified here and likely reflect the initial formation age of large wrinkle ridges. Similar AMAs for the small, recently active ridges identified here are difficult to obtain due to a lack of superposing craters, non-linear ridge morphologies, and the tectonically altered diameters of the craters that have been crosscut (Früh et al., 2020; 2021). The presence of boulder fields on wrinkle ridge scarps has also been used to place temporal constraints on lunar tectonic activity. While many of the ridges presented in this work exhibit relatively low Diviner rock abundance values, we note that several ridges in S. Mare Procellarum, N. Mare Humorum, and Mare Serentiatus exhibit moderate rock abundance values and boulder populations on their bounding

scarps based on the wrinkle ridge rock abundance classification scheme of Valantinas and Schultz, 2020. (Figs. 2.S8–2.S10; Bandfield et al., 2011; Valantinas and Schultz, 2020). The relative lack of boulders on the recently active ridges presented here is potentially a function of substrate structure or lithology and should be pursued as a topic of future work.

Several stress mechanisms have been proposed to account for the formation of young lunar tectonic features on the lunar surface. Large-scale, radial wrinkle ridges located in the nearside mare basins have been postulated to result from vertical compensation in response to mare formation and isostatic loading of the lunar lithosphere (Melosh, 1978; Solomon and Head, 1980; Freed et al., 2001). Separately, the global distribution and preferred N-S orientation of recently active lobate scarps at equatorial latitudes has been cited as evidence for lithospheric flexure due to lunar orbital recession, solid body tides, and global contraction (Melosh, 1978; Melosh, 1980; Watters et al., 2015; 2019). Operating under the assumption that the presence of dense boulder fields on a wrinkle ridge indicates recent tectonic movement of that ridge, another recent study utilized the LRO Diviner rock abundance dataset to identify a network of recently active wrinkle ridges that exhibited heightened boulder populations on their scarp slopes (Bandfield et al., 2011; French et al., 2019; Valantinas and Schultz, 2020). The recently active ridges in Valantinas and Schultz, 2020 were coincident with a deep-seated rift network inferred from polygonal lineations in Gravity Recovery and Interior Laboratory (GRAIL) gravity gradient data (Andrews-Hanna et al.,

2014). The observed recent tectonism was therefore attributed to a reactivation of that deep seated fault system by a stress network that is antipodal to and caused by the SPA impact event (Schultz and Crawford, 2011; Valantinas and Schultz, 2020). Lastly, two separate wrinkle ridge clusters in east Mare Serenitatis and north Mare Imbrium have been presented as being recently active due to potential late-stage mare cooling and global contraction stresses, respectively (Lu et al., 2019; Clark et al., 2022). Morphologically, the small, sinuous ridges analyzed in those latter two studies are the most similar to those mapped in here. As such, mapped wrinkle ridges from Lu et al. (2019) and Clark et al. (2022) were included in our database of recently active ridges on the nearside mare.

Several of the aforementioned stress mechanisms can be ruled out as the cause of recent wrinkle ridge activity identified in our work. Unlike the larger, more evenly distributed wrinkle ridges associated with a mascon tectonic system, the recently active ridges presented here are narrow and sinuous in morphology and often occur in branching clusters of ~10–100 individual ridge segments in both mascon and non-mascon settings. Prior studies have also concluded that formation of mascon-related wrinkle ridge formation ceased at ~1.2 Ga based on crosscutting relationships with other surface features (Melosh et al., 1978; Solomon and Head, 1980; Freed et al., 2001). Thus, causation by mascon isostatic compensation is disfavored as a formation hypothesis due to the differential scale and timing of the ridges associated with that stress mechanism.

The hypothesis of late-stage mare cooling as causation for recent tectonism is partially supported by non-KREEP-bearing lunar samples returned by the Chang'e 5 mission that exhibit radiometric age dates of ~2.0 Ga. Prolonged cooling or volcanism within the lunar mare is necessary to justify such a young crystallization age (e.g., Tian et al., 2021). Given the time disparity between the most recent ridge activity documented here (~0.056 Ga) and the expected cessation of mare volcanism (~1.0 Ga; Schultz and Spudis, 1983; Hiesinger et al., 2011), we expect localized flow cooling and contraction to be an unlikely sole cause of widespread, recent tectonism in the lunar nearside mare. However, an increased number of the recently active wrinkle ridge clusters do appear to fall on young <2.0 Ga mare basalts in east and south Mare Procellarum (Hiesinger et al., 2011). Establishing a statistically robust correlation between mare surface age and recent tectonic activity is beyond the scope of the work presented here but may assist in deciphering between the potential formative causes presented below.

The ridges mapped in our work exhibit preferred NNW-SSE linear orientations at near-equatorial latitudes (0–30°S, 0–30°N) that gradually shallow to WNW-ESE orientations at greater distances from the lunar equator (30–60˚ N) (Fig. 2.4). At equatorial latitudes, these fault orientation patterns are consistent with those expected from stresses originating via a combination of lunar orbital recession, solid-body tides, and global contraction (e.g., Fig. 2C in Watters et al., 2015). However, the higher latitude wrinkle ridges (30–60˚N) exhibit a preferred

orientation that is perpendicular to the predicted orientation of compressional features resulting from the net isotropic stress field induced by orbital recession, global contraction, and tidal forces (Fig. 2.S11a). Such deviations could be a result of structural control over the recently active ridges by pre-existing faults or joints in the subsurface basalt layers. There also appears to be a lack of wrinkle ridge alignment with predicted feature orientations at the sub-Earth point on the lunar surface. In an attempt to account for potential structural control on the recently active ridge presented here, we have also measured preferred orientations of our ridges with ridges near mare boundaries excluded from the sampling (Fig. 2.S12). When ridges near mare boundaries were excluded from our orientation measurements, the preferred orientation of equatorial (30°N-30°S) ridges remained ~N-S whereas the high-latitude (30°N–60°N) ridges were slightly less E-W skewed.

Many of the recently active ridges mapped here also appear to be spatially correlated with GRAIL gravity gradient data (Fig. 2.S11b). Such a correlation is consistent with formation by an antipodal SPA stress network and associated deep moonquakes centered beneath the lunar nearside mare (Schultz and Crawford, 2011; Valantinas and Schultz, 2020). One primary difference between these two potential stress mechanisms is the scale and timing of tectonic deformation that results from each. The surface expression of an SPA antipodal stress release has been identified as a reactivation of deep-seated faults and a shifting of larger wrinkle ridges associated with those faults (Valantinas and

Schultz, 2020). An SPA-induced stress field would have also been most intense immediately after the SPA formation event (<4.2 Ga), and the associated energies would have relaxed somewhat with time. The lower lithospheric stresses imparted by ongoing orbital recession (~20–40 KPa) are more likely to result in morphologically smaller, recently-formed tectonic landforms that are limited in width, length, and depth of deformation (Watters et al., 2015). The narrow, sinuous morphologies associated with many of the ridges mapped in our work appear consistent with formation by those lithospheric stresses imparted by orbital recession, global contraction, and tidal forces. However, a close spatial correlation also exists between several recently active ridges and deep-seated rifts inferred from GRAIL gravity gradient data (i.e., Mare Frigoris, Mare Serenitatis, and Oceanus Procellarum). Therefore, SPA antipodal stresses are partially supported as a formation hypothesis for those recently active ridges that deviate from the predicted orientations noted above. If temporally viable, the addition of a secondary, SPA-induced stress mechanism helps to explain the local deviations from the overall NNW-SSE orientation observed in our wrinkle ridge dataset.

Conclusions

Through our analysis of small-scale wrinkle ridges and tectonically deformed impact craters on the lunar surface, we put forth the following conclusions.

- We identify tectonically deformed impact craters on the lunar mare in the diameter range of ~0.03–2.0 km. Models of ejecta boulder breakdown and

crater degradation indicate that the wrinkle ridges deforming the majority of these craters have been active in the time frame of ~0.056–1.5 Ga (Basilevsky, 1976; Moore et al., 1980; Fassett and Thomson, 2014; Li et al., 2018; Lu et al., 2019 Williams et al., 2019).

- Individual ridges identified in our work display narrow, sinuous morphologies and are spatially clustered in at least 37 isolated areas across most nearside mare basins. These recently active ridge clusters occur at the centers and edges of both mascon and non-mascon mare, indicating that their formation and activity is likely unrelated to mare thickness or isostatic compensation of the lunar lithosphere.
- The recently active wrinkle ridge segments documented here exhibit a preferred NNW-SSE orientation at equatorial latitudes that shallows to a WNW-ESE orientation with increased latitude. The small scale and orientation patterns of recently active wrinkle ridges at equatorial latitudes is consistent with formation by orbital recession, global contraction, and tidal forces (e.g., Watters et al., 2015). However, given the spatial coincidence between several recently active ridges and deep-seated rifts inferred from GRAIL gravity gradient data, SPA antipodal stresses are also a viable formation mechanism for a subset of the tectonic features presented here if those stresses have persisted since the SPA event (e.g., Valantinas and Schultz, 2020).

- We note that data gaps and time constraints prohibited a complete mapping of all recently active ridges on the lunar surface in this work. Future work should focus on establishing an exhaustive database of recently active wrinkle ridges on the Moon, using crater statistics to establish absolute ages for those recently active ridges, and further subdividing those wrinkle ridges based on morphological differences. Such investigations would allow for better constraints on the exact timing and causes of recent lunar tectonism.

References

Andrews-Hanna, J. C., Besserer, J., Head III, J. W., et al., (2014). Structure and evolution of the lunar Procellarum region as revealed by GRAIL gravity data. Nature, 514(7520), 68-71. https://doi.org/10.1038/nature13697

Bandfield, J. L., Ghent, R. R., Vasavada, A. R., Paige, D. A., Lawrence, S. J., & Robinson, M. S. (2011). Lunar surface rock abundance and regolith fines temperatures derived from LRO Diviner Radiometer data. Journal of Geophysical Research, 116, E00H02. https://doi.org/10.1029/2011je003866

Banks, M. E., Watters, T. R., Robinson, M. S., Tornabene, L. L., Tran, T., Ojha, L., & Williams, N. R. (2012). Morphometric analysis of small-scale lobate scarps on the Moon using data from the Lunar Reconnaissance Orbiter. Journal of Geophysical Research: Planets, 117(E12). https://doi.org/10.1029/2011JE003907

Basilevsky, A. T. (1976). On the evolution rate of small lunar craters, Proc. Lunar Planet. Sci. Conf., 7th, 1005– 1020.

Binder, A. B. (1982). Post-Imbrian global lunar tectonism: Evidence for an initially totally molten Moon. The moon and the planets, 26(2), 117-133. https://doi.org/10.1007/BF00929277

Binder, A. B., & Gunga, H. C. (1985). Young thrust-fault scarps in the highlands: Evidence for an initially totally molten Moon. Icarus, 63(3),421–441. https://doi.org/10.1016/0019-1035(85)90055-7

Clark, J. D., Bernhardt, H., Robinson, M. S., (2022). Extensional features at east Serenitatis wrinkle ridge-lobate scarp transition indicate recent tectonic activity. In 52nd Annual Lunar and Planetary Science Conference (No. 1305). https://www.hou.usra.edu/meetings/lpsc2017/pdf/1001.pdf

Clark, J. D., Hurtado, J. M., Hiesinger, H., van der Bogert, C. H., & Bernhardt, H. (2017). Investigation of newly discovered lobate scarps: Implications for the tectonic and thermal evolution of the Moon. Icarus, 298, 78–88. https://doi.org/10.1016/j.icarus.2017.08.017

Fassett, C. I., & Thomson, B. J. (2014). Crater degradation on the lunar maria: Topographic diffusion and the rate of erosion on the Moon. Journal of Geophysical Research: Planets, 119(10), 2255-2271. https://doi.org/10.1002/2014JE004698

Freed, A. M., Melosh, H. J., & Solomon, S. C. (2001). Tectonics of mascon loading: Resolution of the strike-slip faulting paradox. Journal of Geophysical Research: Planets, 106(E9), 20603–20620. https://doi.org/10.1029/2000JE001347

French, R. A., Watters, T. R., & Robinson, M. S. (2019). Provenance of block fields along lunar wrinkle ridges. Journal of Geophysical Research: Planets, 124(11), 2970-2982. https://doi.org/10.1029/2019JE006018

Frueh, T., Hiesinger, H., van der Bogert, C. H., & Schmedemann, N. (2020). Reassessment of Individual Lunar Wrinkle Ridge Ages in Mare Tranquillitatis. In 51st Lunar and Planetary Science Conference (Abs. 2326). https://www.hou.usra.edu/meetings/lpsc2020/pdf/1854.pdf

Frueh, T., Hiesinger, H., van der Bogert, C. H., Schmedemann, N., & Pauw, L. (2021). Possible Timing of Wrinkle Ridge Formation in Mare Tranquillitatis. In 52nd Lunar and Planetary Science Conference (Abs. 2548). http://www.hou.usra.edu/meetings/lpsc2021/pdf/1661.pdf

Frueh, T., Hiesinger, H., van der Bogert, C. H., Clark, J. D., Watters, T. R., & Schmedemann, N. (2023). Timing and origin of compressional tectonism in Mare Tranquillitatis. Journal of Geophysical Research: Planets, 128, e2022JE007533. https://doi.org/10.1029/2022JE007533

Golombek, M. P. (1979). Structural analysis of lunar grabens and the shallow crustal structure of the Moon. J. Geophys. Res., 84,4657-4666.

Hiesinger, H., Head, J. W., Wolf, U., Jaumann, R., & Neukum, G. (2011). Ages and stratigraphy of lunar mare basalts: A synthesis. Recent advances and current research issues in lunar stratigraphy. Geological Society of America Special Paper, 477, 1-51. https://doi.org/10.1130/2011.2477(01)

Li, B., Ling, Z., Zhang, J., Chen, J., Ni, Y., & Liu, C. (2018). Displacement-length ratios and contractional strains of lunar wrinkle ridges in Mare Serenitatis and Mare Tranquillitatis. Journal of Structural Geology, 109, 27-37. https://doi.org/10.1016/j.jsg.2018.01.003

Lu, Y., Wu, Y., Michael, G. G., Basilevsky, A. T., & Li, C. (2019). Young wrinkle ridges in Mare Imbrium: Evidence for very recent compressional tectonism. Icarus, 329, 24–33. https://doi.org/10.1016/j.icarus.2019.03.029

Lucchitta, B. K., & Watkins, J. A. (1978). Age of graben systems on the moon. In 9th lunar and planetary science conference (pp. 3459–3472).

Matsuyama, I., Keane, J. T., Trinh, A., Beuthe, M., & Watters, T. R. (2021). Global tectonic patterns of the Moon. Icarus, 358, 114202.

Maxwell, T.A. and Phillips, R.J. (1978). Stratigraphic correlation of the radar-detected subsurface interface in Mare Crisium. Geophys. Res. Lett., 5, 811-814.

McGill, G. E. (1971). Attitude of fractures bounding straight and arcuate lunar rilles. Icarus, 14, 53-58.

Melosh, H. J. (1978). The tectonics of mascon loading. In Lunar and planetary science conference proceedings (Vol. 9, pp. 3513-3525).

Melosh, H. J. (1980). Tectonic patterns on a tidally distorted planet. Icarus, 43, 334-337. https://doi.org/10.1016/0019-1035(80)90178-5

Moore, H. J., Boyce, J. M., & Hahn, D. A. (1980). Small impact craters in the lunar regolith—Their morphologies, relative ages, and rates of formation. The moon and the planets, 23(2), 231-252. https://doi.org/10.1007/BF00899820

Nypaver, C. A. & Thomson, B. J. (2022A). NypaverThomson_2022_data. figshare. Dataset. https://doi.org/10.6084/m9.figshare.19491668.v3

Nypaver, C. A. & Thomson, B. J. (2022B). New observations of recently active wrinkle ridges in the lunar mare: Implications for the timing and origin of lunar tectonics. Dataset. Zenodo. https://doi.org/10.5281/zenodo.6624329

Peeples, W. J., Sill, W. R., May, T. W., Ward, S. H., Philips, R. J., Jordan, R. L., Abbott, E. A., and Killpack, T. J. (1978). Orbital radar evidence for Lunar subsurface layering in Maria Serenitatis and Crisium. J. Geophys. Res., 83, 3459-3468.

Phillips, R. J., Adams, G. E, Brown, W. E., Jr., Eggleton, R. E., Jackson, P., Jordan, R., Peeples, W. J., Porcello, L. J., Ryu, J., Schaber, G., Sill, W. R., Thompson, T. W., Ward, S. H., and Zelenka, J. S. (1973). The Apollo 17 Lunar Sounder (Proc. Lunar Science Conf. 4). Geochim. Cosmochim. Acta, 3, (Suppl. 4), 2821-2831. Plescia, J. B., & Golombek, M. P. (1986). Origin of planetary wrinkle ridges based on the study of terrestrial analogs. Bulletin of the Geological Society of America, 97(11), 1289–1299. https://doi.org/10.1130/0016-7606(1986)97

Schleicher, L. S., Watters, T. R., Martin, A. J., & Banks, M. E. (2019). Wrinkle ridges on Mercury and the Moon within and outside of Mascons. Icarus, 331, 226-237. https://doi.org/10.1016/j.icarus.2019.04.013

Schmitt, H., et al. (2017), Revisiting the field geology of Taurus–Littrow. Icarus, 298, 2–33. https://doi.org/10.1016/j.icarus.2016.11.042.

Schmitt, H.H. and Ceman, E. A. (1973). Geological investigation of the Apollo 17 landing site. Apollo 17 Prel. Sci. Rep., NASA Spec. Pub, SP-330, 5-1 - 5-21.

Schultz, P. H. (1976). Moon morphology: Interpretations based on Lunar Orbiter photography. Austin: University of Texas Press. 308-322.

Schultz, P. H., & Crawford, D. A. (2011). Origin of nearside structural and geochemical anomalies on the Moon. Geological Society of America Special Papers, 477, 141-159. https://doi.org/10.1130/2011.2477(07)

Schultz, P. H., & Spudis, P. D. (1983, March). The beginning and end of mare volcanism on the Moon. In Lunar and Planetary Science Conference (Vol. 14, pp. 676-677).

Solomon, S. C., & Head, J. W. (1979). Vertical movement in mare basins: Relation to mare emplacement, basin tectonics, and lunar thermal history. Journal of Geophysical Research, 84(B4), 1667–1682. https://doi.org/10.1029/jb084ib04p01667

Solomon, S. C., & Head, J. W. (1980). Lunar Mascon Basins: Lava filling, tectonics, and evolution of the lithosphere. Reviews of Geophysics (1985), 18(1), 107–141. https://doi.org/10.1029/RG018i001p00107

Speyerer, E. J., Povilaitis, R. Z., Robinson, M. S., Thomas, P. C., & Wagner, R. V. (2016). Quantifying crater production and regolith overturn on the Moon with temporal imaging. Nature, 538 (7624), 215-218. https://doi.org/10.1038/nature19829

Strom, R. G. (1972). Lunar mare ridges, rings and volcanic ring complexes. In S. K. Runcorn & H. C. Urey (Eds.), The Moon (Vol. 47, pp. 187–215). International Astronomical Union. https://doi.org/10.1007/978-94-010-2861-5_19

Thompson, T.J., Robinson, M.S., Watters, T.R. and Johnson, M.B., (2017). March. Global lunar wrinkle ridge identification and analysis. In 48th Annual Lunar and Planetary Science Conference (Abs. 2665). https://www.hou.usra.edu/meetings/lpsc2017/pdf/2665.pdf

Tian, H. C., Wang, H., Chen, Y., et al., (2021). Non-KREEP origin for Chang'e-5 basalts in the Procellarum KREEP Terrane. Nature, 600 (7887), 59-63. https://doi.org/10.1038/s41586-021-04119-5

Trask, N. J. (1971). Geologic comparison of mare materials in the lunar equatorial belt, including Apollo 11 and Apollo 12 landing sites. US Geol. Surv. Prof. Pap., 750D, 138-148.

Valantinas, A., & Schultz, P. H. (2020). The origin of neotectonics on the lunar nearside. Geology, 48(7), 649–653. https://doi.org/10.1130/G47202.1

van der Bogert, C. H., Clark, J. D., Hiesinger, H., Banks, M. E., Watters, T. R., & Robinson, M. S. (2018). How old are lunar lobate scarps? 1. Seismic resetting of crater size-frequency distributions. Icarus, 306, 225–242. https://doi.org/10.1016/j.icarus.2018.01.019

Watters, T. R. (1988). Wrinkle ridge assemblages on the terrestrial planets. Journal of Geophysical Research: Solid Earth, 93(B9), 10236-10254. https://doi.org/10.1029/JB093iB09p10236

Watters, T. R. (2004). Elastic dislocation modeling of wrinkle ridges on Mars. Icarus, 171(2), 849 284–294. https://doi.org/10.1016/j.icarus.2004.05.024

Watters, T. R. (2022). Lunar Wrinkle Ridges and the Evolution of the Nearside Lithosphere. Journal of Geophysical Research: Planets, 127(3), e2021JE007058. https://doi.org/10.1029/2021JE007058

Watters, T. R., Johnson, C. L., & Schultz, R. A. (2010). Lunar tectonics. In Planetary tectonics, 11, 121.

Watters, T. R., Robinson, M. S., Banks, M. E., Tran, T., & Denevi, B. W. (2012). Recent extensional tectonics on the Moon revealed by the Lunar

Reconnaissance Orbiter Camera. Nature Geoscience, 5(3), 181–185. https://doi.org/10.1038/ngeo1387

Watters, T. R., Weber, R. C., Collins, G. C., Howley, I. J., Schmerr, N. C., & Johnson, C. L. (2019). Shallow seismic activity and young thrust faults on the Moon. Nature Geoscience, 12(6), 411–417. https://doi.org/10.1038/s41561-019-0362-2

Watters, T.R., Robinson, M. S., Beyer, R. A., Banks, M. E., Bell, 3rd, Pritchard, M. E., Hiesinger, H., van der Bogert, C. H., Thomas, P. C., Turtle, E. P., & Williams, N. R. (2010). Evidence of Recent Thrust Faulting on the Moon Revealed by the Lunar Reconnaissance Orbiter Camera. Science (American Association for the Advancement of Science), 329(5994), 936–940. https://doi.org/10.1126/science.1189590

Watters, T.R., Robinson, M. S., Collins, G. C., Banks, M. E., Daud, K., Williams, N. R., & Selvans, M. M. (2015). Global thrust faulting on the Moon and the influence of tidal stresses. Geology, 43(10), 851–854. https://doi.org/10.1130/G37120.1

Whitaker, E. A. (1981). The lunar Procellarum basin. In Multi-ring basins: Formation and evolution (pp. 105-111).

Wilhelms, D. E., John, F., & Trask, N. J. (1987). The geologic history of the Moon (No. 1348).

Williams, N. R., Bell III, J. F., Watters, T. R., Banks, M. E., Daud, K., & French, R. A. (2019). Evidence for recent and ancient faulting at Mare Frigoris and implications for lunar tectonic evolution. Icarus, 326, 151–161. https://doi.org/10.1016/j.icarus.2019.03.002

Yue, Z., Li, W., Di, K., Liu, Z., & Liu, J. (2015). Global mapping and analysis of lunar wrinkle ridges: LUNAR WRINKLE RIDGES GLOBAL MAPPING. Journal of Geophysical Research. Planets, 120(5), 978–994. https://doi.org/10.1002/2014JE004777

Yue, Z., Michael, G., Di, K., & Liu, J. (2017). Global survey of lunar wrinkle ridge formation times. Earth and Planetary Science Letters, 477, 14–20. https://doi.org/10.1016/j.epsl.2017.07.048

Appendix

Figures

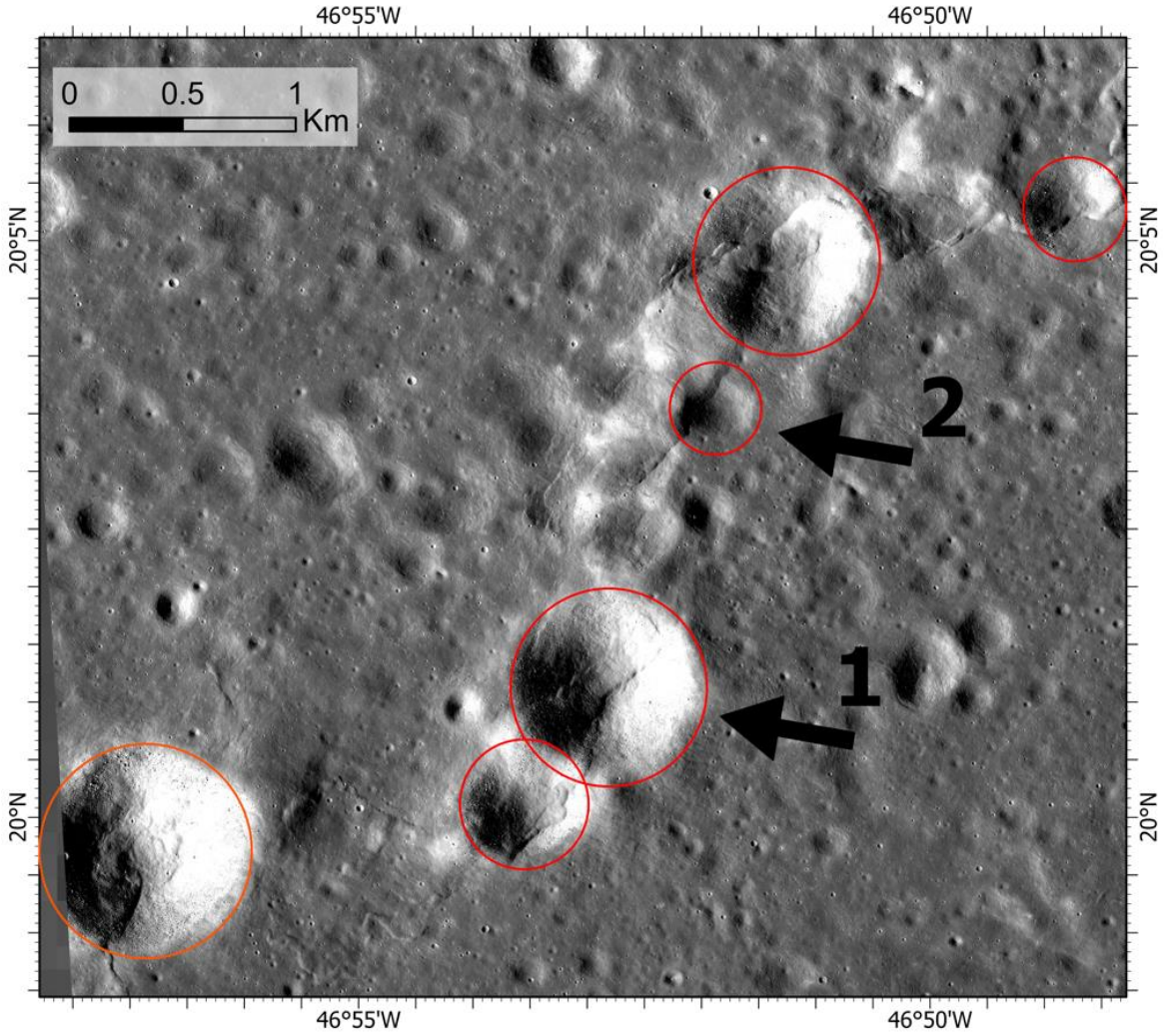

Figure 2.1. LROC NAC image showing: 1) a degraded crater crosscut by both parallel wrinkle ridge scarps and 2) crater deformation by a single wrinkle ridge scarp (LROC NAC M1219258635RE). Red circles represent tectonically deformed impact crater rims.

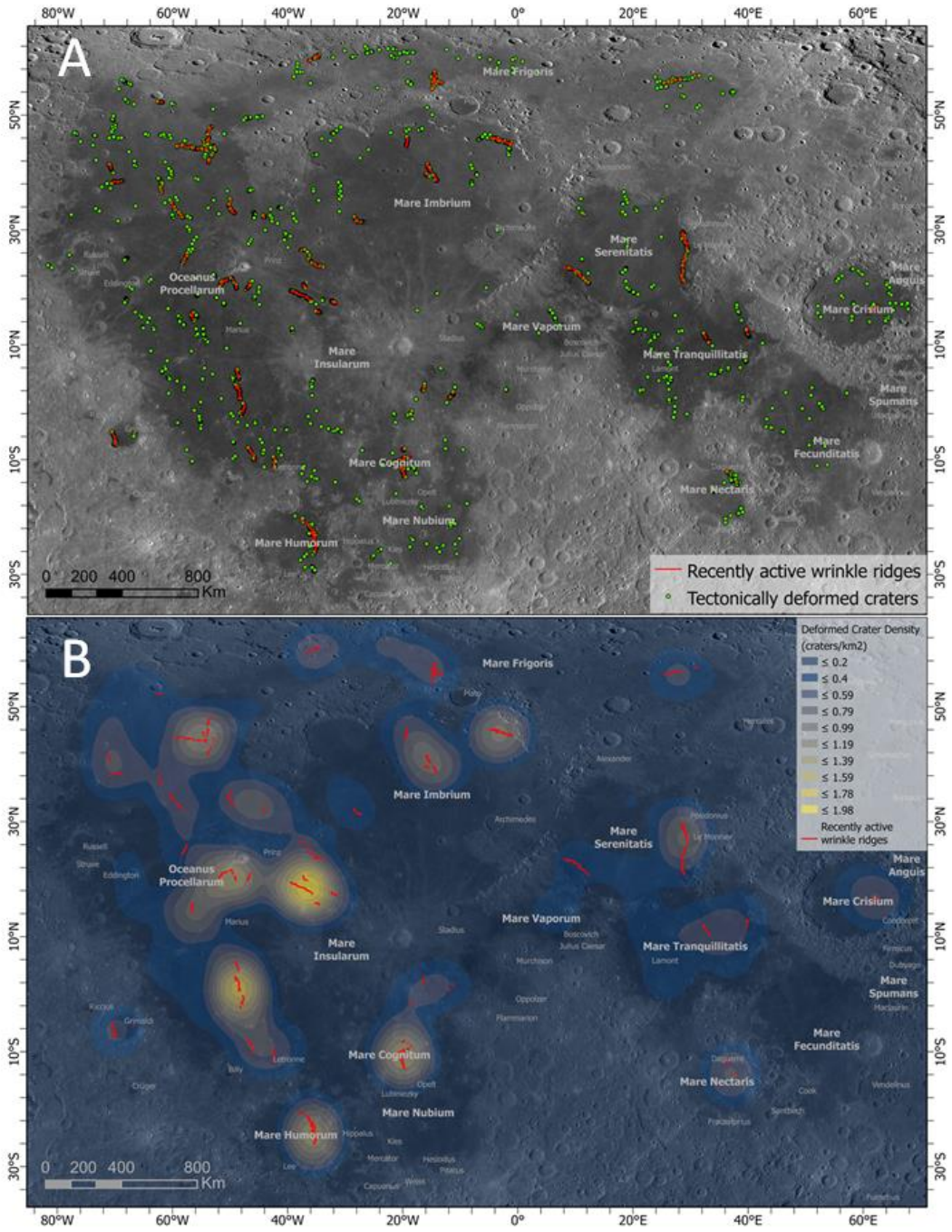

Figure 2.2. (A) Recently active wrinkle ridge segments (red line features) and 2,277 tectonically deformed impact craters identified in this study (green point features) overlying an LROC WAC mosaic of the lunar nearside mare. (B) Density map of the tectonically deformed impact craters given in part (A) overlain by the recently active wrinkle ridge segments identified in this work (red line features).

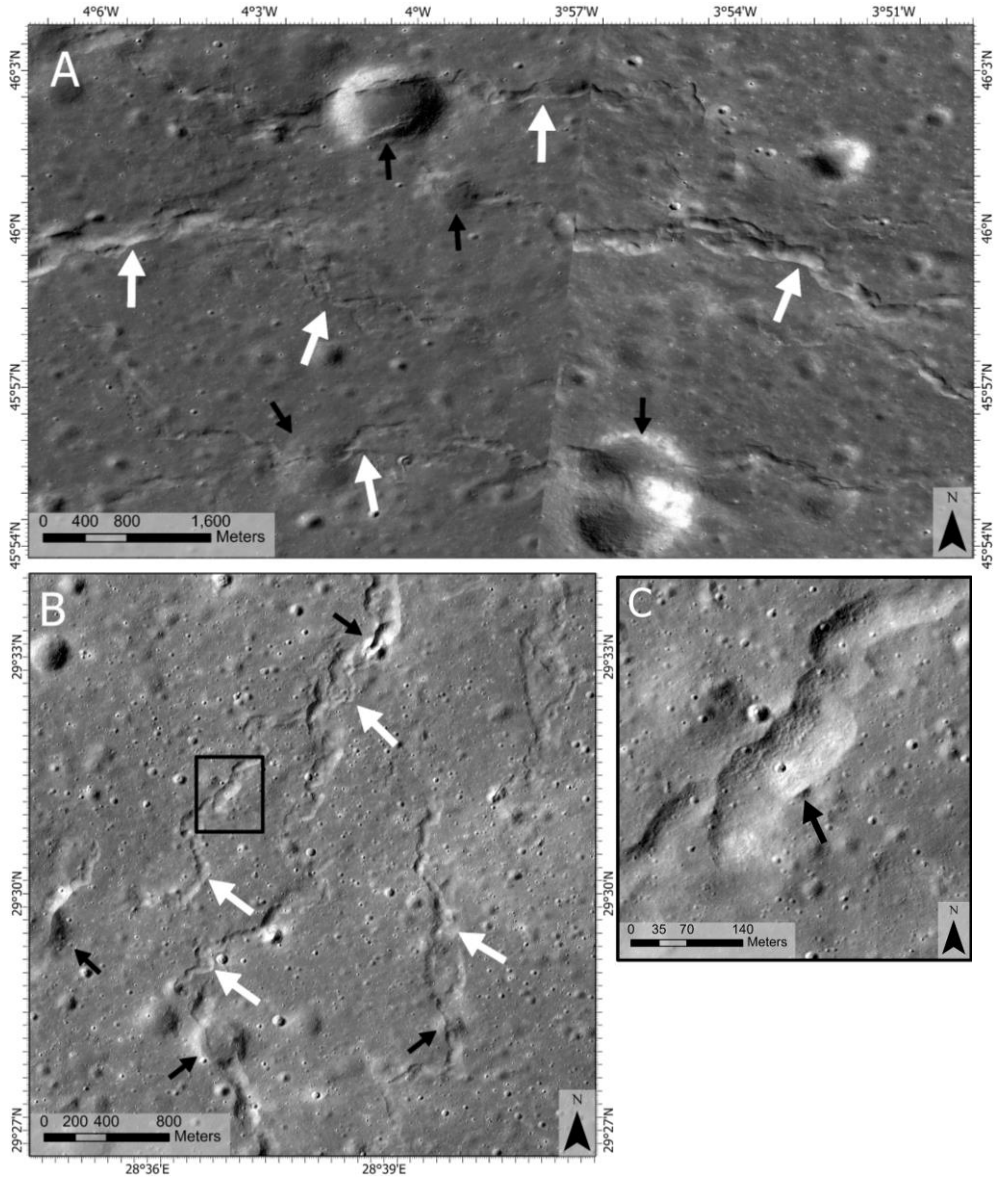

Figure 2.3. Examples of recently active wrinkle ridge systems located in N. Mare Imbrium (a) (LROC NAC M1274280167RE, M1236649139LE) and E. Mare Serenitatis (b) (LROC NAC M1289319410LE). (c) Image subset depicting a ~35 m-diameter impact crater crosscut by a recently active wrinkle ridge. White arrows indicate recently active ridges and black arrows show crosscut craters in all images.

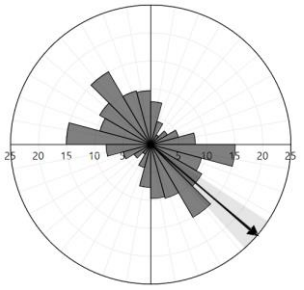

(A) 30˚N - 60˚N

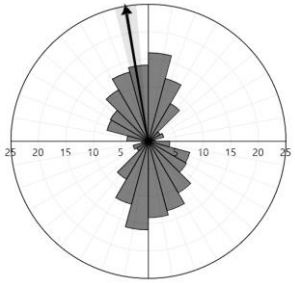

(**B**) 0˚ - 30˚N

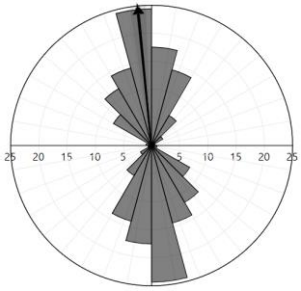

(**C**) 0˚ - 30˚S

Figure 2.4. Rose diagrams showing the preferred orientations of recently active, small wrinkle ridges (Fig. 2.2a) between (A) 30˚N and 60˚N, (B) 0˚ and 30˚N, and (C) 0˚ and 30˚ S. Arrows indicate preferred orientations.

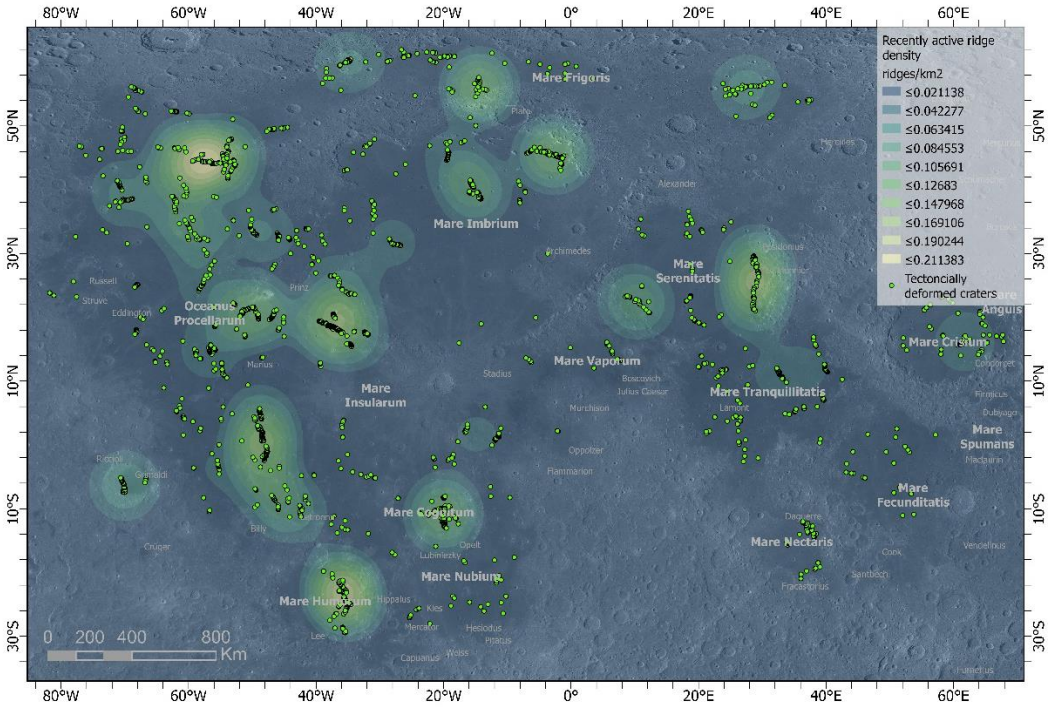

Figure 2.S5. Density map of the recently active wrinkle ridges given in Fig. 2a overlain by the tectonically deformed craters (green point features). Given that the tectonically deformed impact crater database was used to aid in the identification of recently active ridges, an inherent correlation between the densities of recently active ridges and tectonically deformed craters is expected.

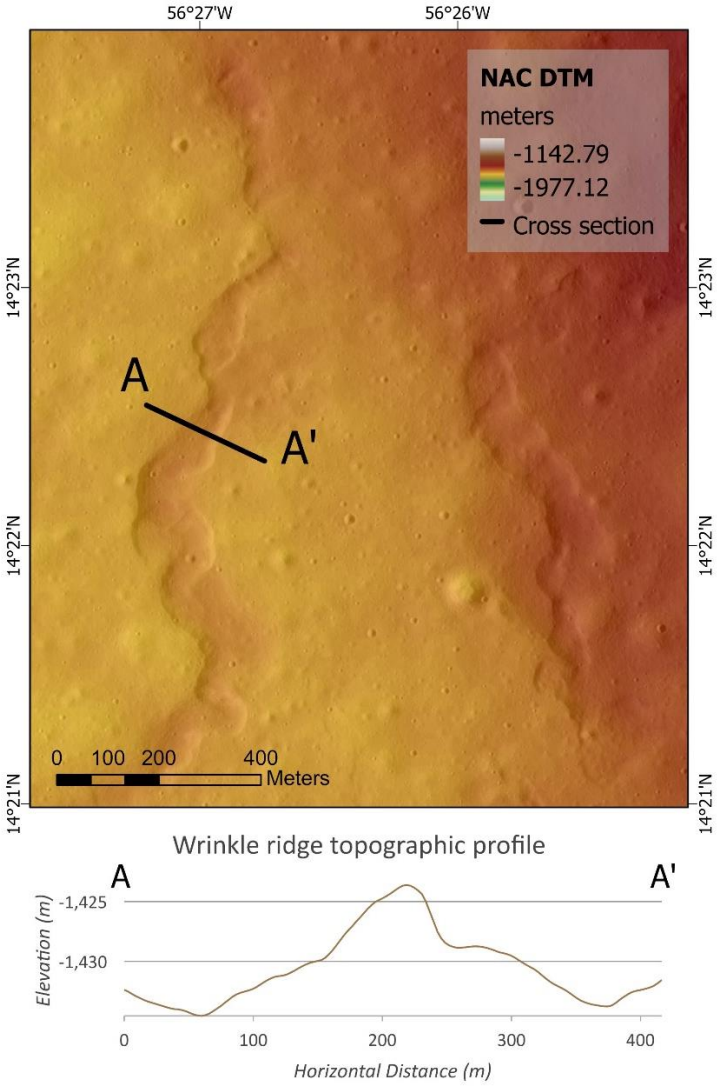

Figure 2.S6. LROC NAC image (Marius Cone ROI mosaic) of a wrinkle ridge complex located in central Mare Procellarum overlaid by an LROC NAC Digital Terrain Model (DTM; Marius Cone 1). In cross section, the ridge system here exhibits a narrow (~100 m) central ridge with a steep southeast facing scarp that is underlain by a broader (~300 m) topographic arch. At center, the ridge exhibits ~12 m in total relief.

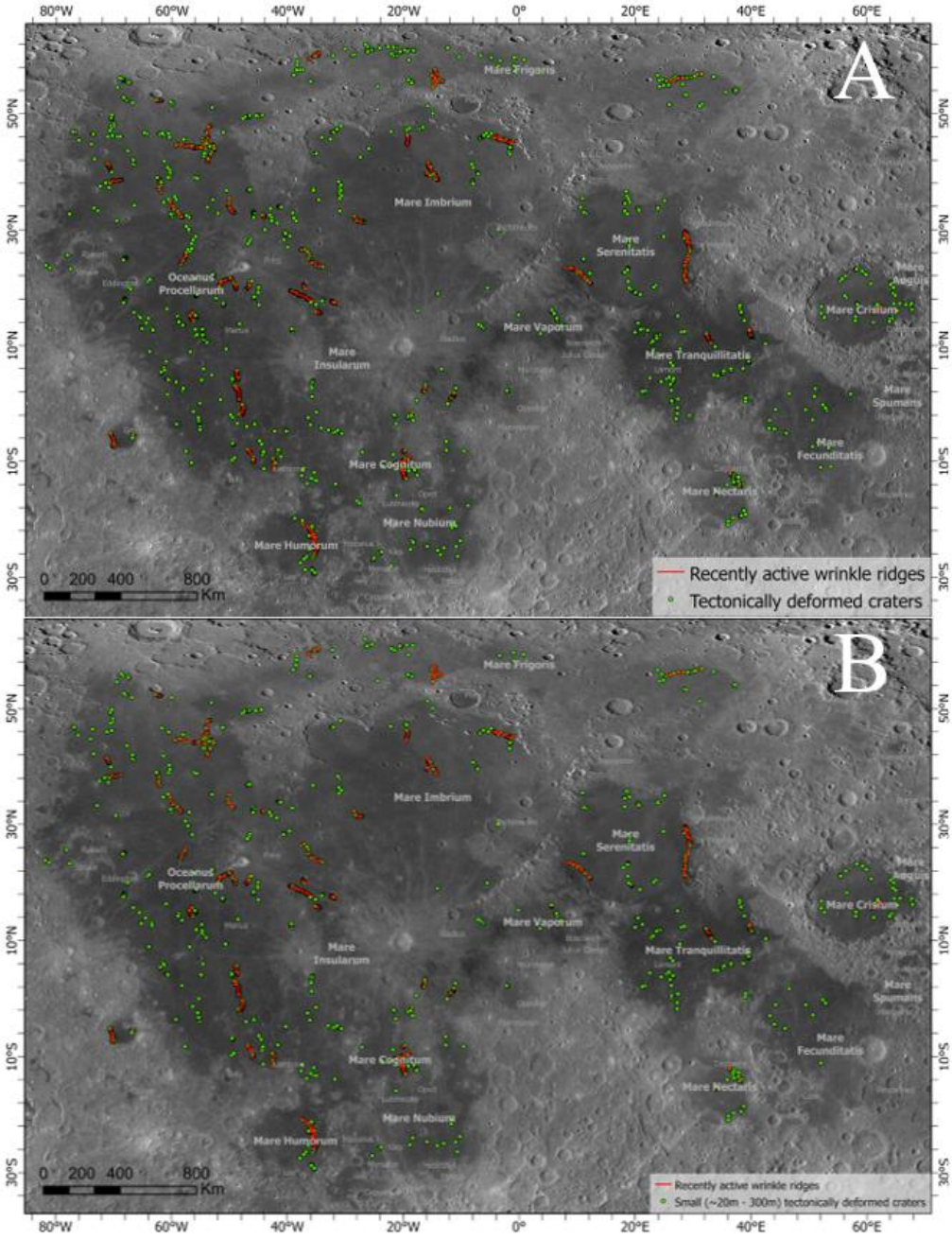

Figure 2.S7. (A) Overall distribution of 2,277 tectonically deformed impact craters in the diameter range of ~0.03–2.0 km (green point features). (B) Distribution of tectonically deformed impact craters clipped to only those smaller (~30–300 m diameter) craters that are not visible at the resolution of the LROC WAC image data (100m/pixel).

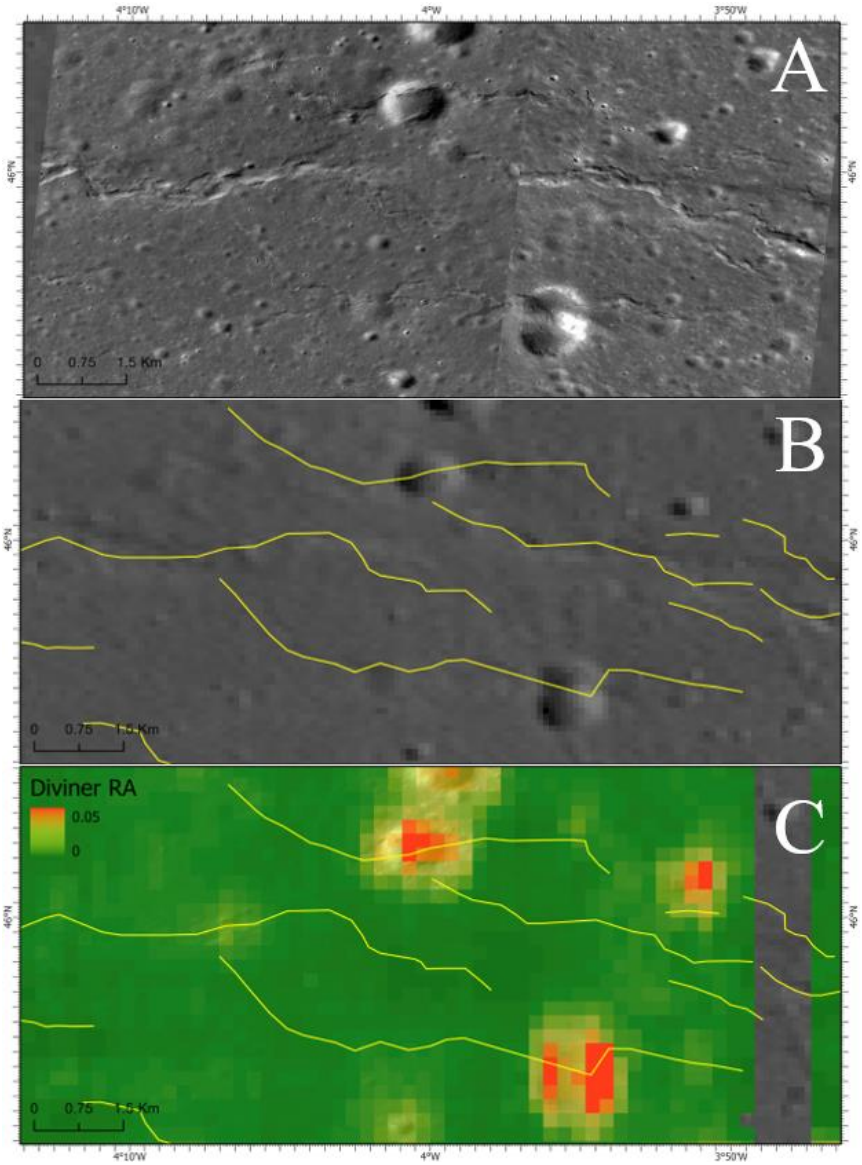

Figure 2.S8. (A) Wrinkle ridge complex from Fig. 3a Shown in LROC NAC data M1274280167RE, M1236649139LE), (B) LROC WAC data (100m/pixel), and (C) Diviner Rock Abundance data (237 m/pixel). The yellow polylines in the LROC WAC and Diviner rock abundance data indicate the locations of the wrinkle ridges in those data. Only the largest of the recently active ridges are visible in the WAC data, and the ridges are not visible in the Diviner Rock abundance data where all the elevated RA pixels appear to be associated with impact craters of varying sizes.

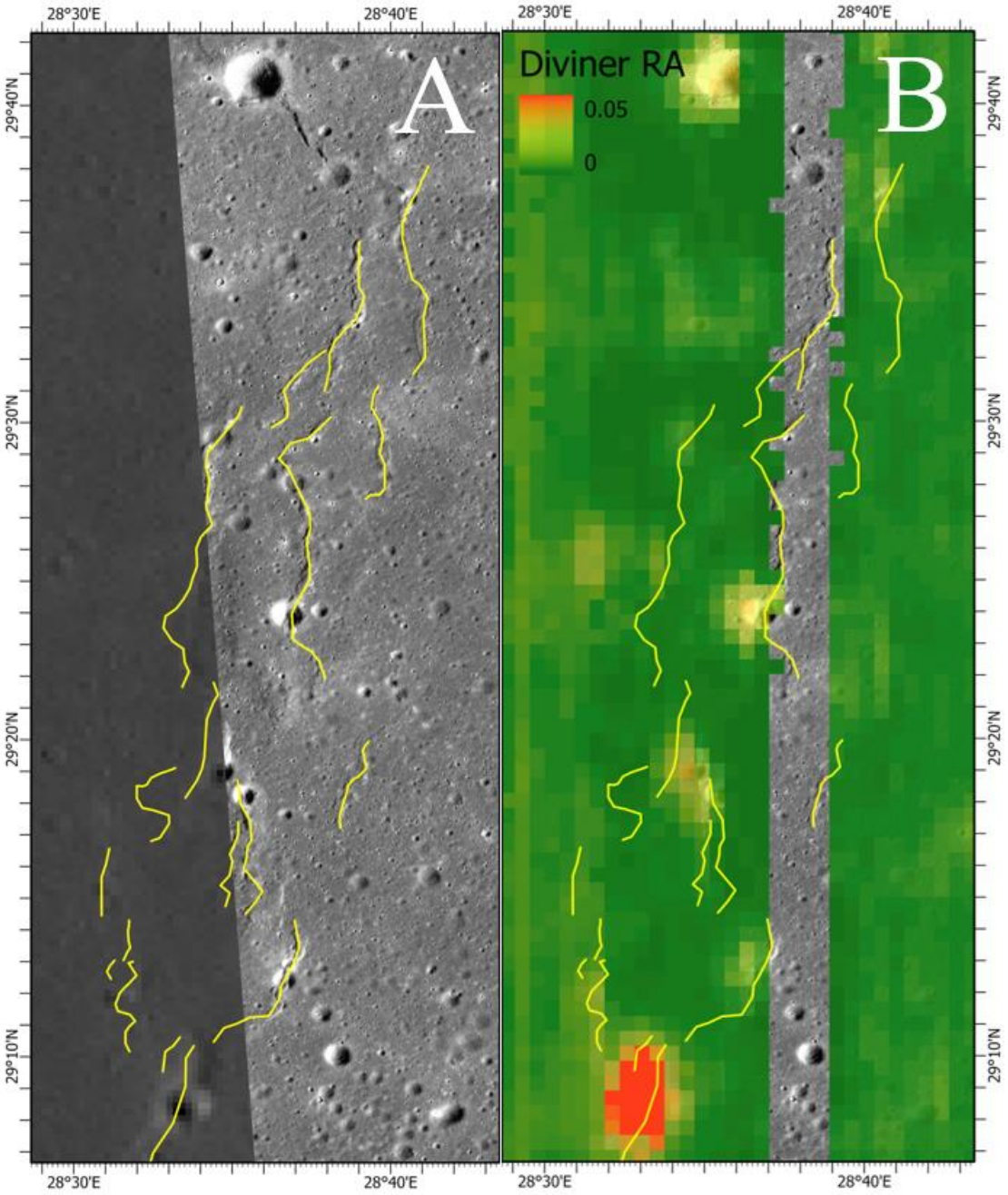

Figure 2.S9. (A) Wrinkle ridge complex from Fig. 3b Shown in LROC NAC data (LROC NAC M1289319410LE) and LROC WAC data (100m/pixel), and (B) Diviner Rock Abundance data (237 m/pixel). The yellow polylines in the LROC NAC, WAC, and Diviner rock abundance data indicate the locations of the recently active wrinkle ridges.

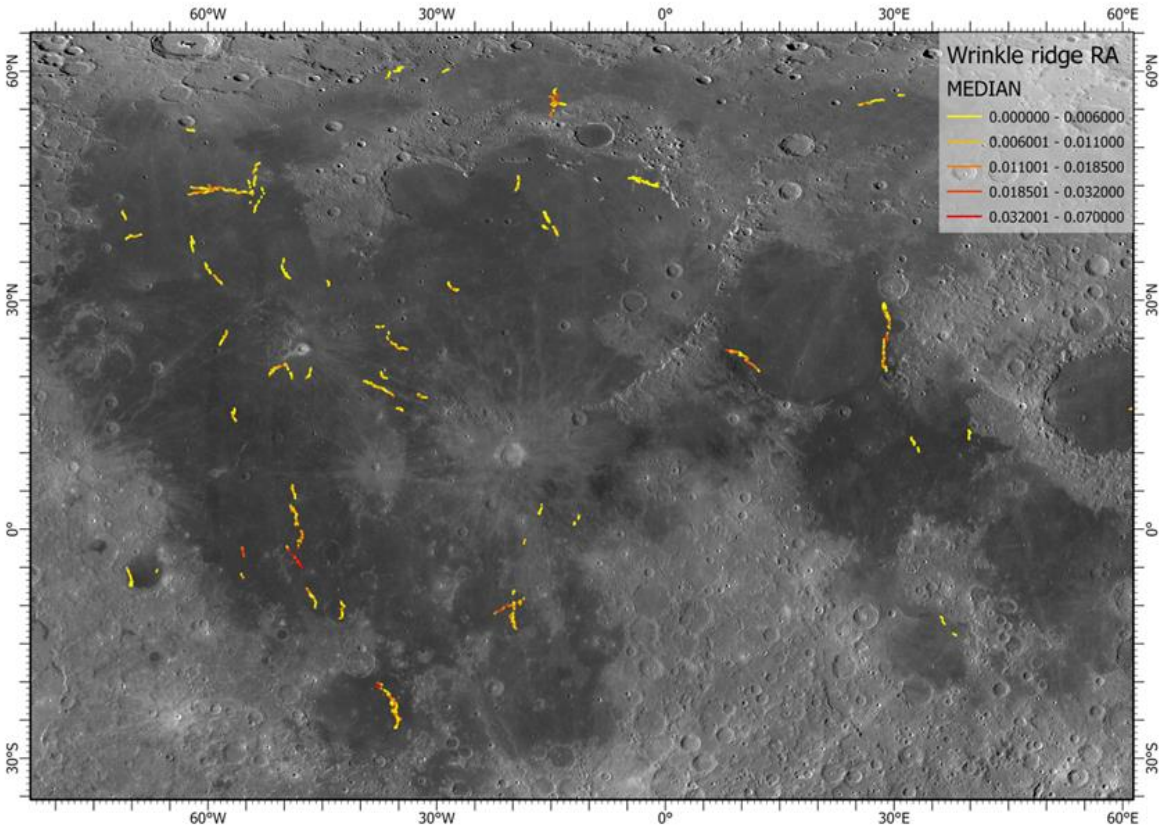

Figure 2.S10. Recently active wrinkle ridges identified in this work colorized by median Diviner rock abundance value. Many of the wrinkle ridges exhibit low rock abundance values, but several ridges in S. Mare Procellarum, Mare Serenitatis, and Mare Frigoris exhibit moderate rock abundance.

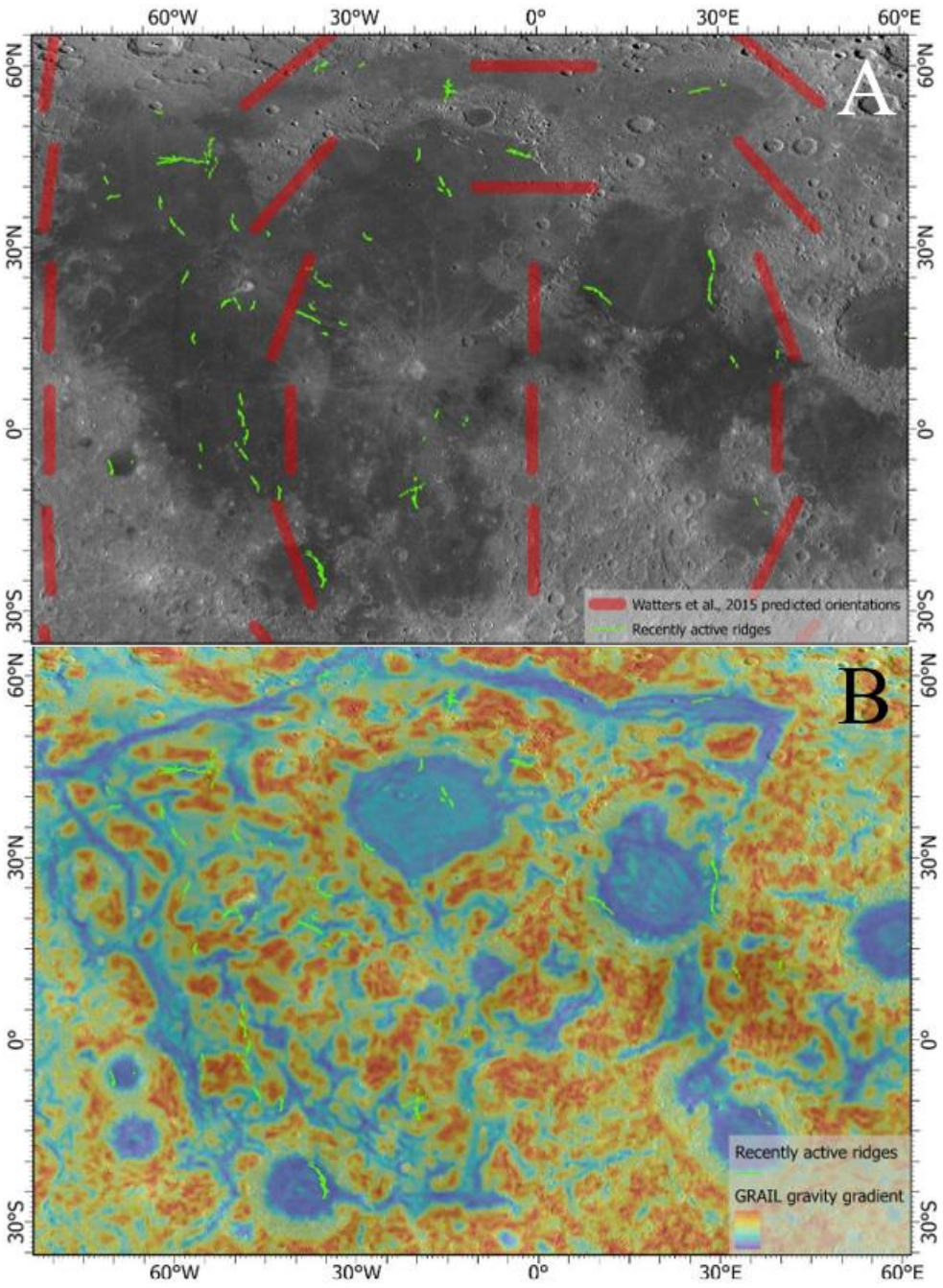

Figure 2.S11. (A) Recently active ridges mapped here (green polylines), overlain by the predicted compressional feature orientations (red polylines) from Watters et al., 2015 and (B) overlain onto the GRAIL gravity gradient dataset from Andrews-Hanna et al., 2014. Recently active ridges identified in this work show broad correlations with both the predicted orientations and the deep rift system inferred from the GRAIL gravity gradient data.

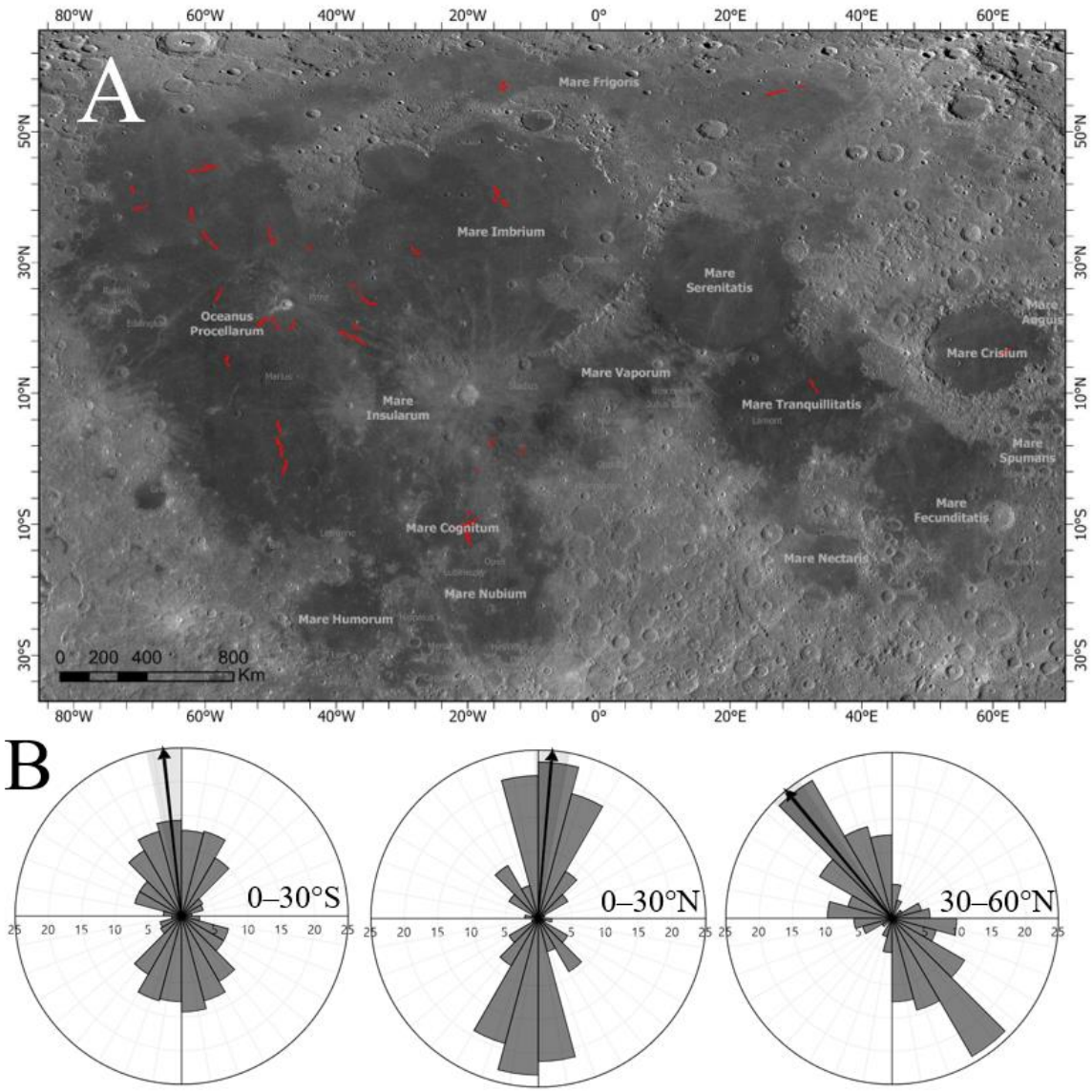

Figure 2.S12. (A) Wrinkle ridges that appear to exhibit structural control from mare boundaries have been removed from our database, and orientations have been replotted in 30° bins to match those in Fig. 2.4. (B) When boundary ridges are excluded from our database, equatorial ridges exhibit a preferred N-S orientation and higher latitude ridges exhibit a NW-SE orientation.

CHAPTER THREE : A DRONE BASED THERMOPHYSICAL INVESTIGATION OF BARRINGER METEORITE IMPACT CRATER EJECTA

Abstract

The impact cratering process has played a substantial role in shaping solid planetary surfaces throughout our solar system. However, variable environmental and geologic surface conditions can lead to interplanetary variations in impact crater formation and breakdown mechanics. Those variations are commonly quantified using orbital remote sensing data, but such investigations can be limited in scope and detail by the coarse resolution of orbital data. Investigations of terrestrial impact craters do not share this resolution-based limitation due to readily attainable, in situ measurements and the ability to collect higher-resolution remote sensing datasets. Therefore, terrestrial impact crater studies can improve our understanding of the impact cratering process on other planetary bodies by reexamining the validity of geologic interpretations derived from orbital data. The purpose of the work presented here is to use low-resolution (90 m/pixel) orbital and high-resolution (23 cm/pixel) drone-based thermophysical data—sensitive to surface grain size distribution and induration—to measure the ejecta distribution patterns of Meteor Crater in northeast Arizona, USA. In doing so, our work will serve to validate the effectiveness of thermophysical data for geologic mapping and impact ejecta analyses on Earth and beyond. Our results indicate that the thermophysical properties of the Meteor Crater ejecta blanket are well constrained at the scale of the orbital data resolution. Surface composition and thermophysical properties are also well correlated when the data sampling is conducted far from defined unit boundaries. However, when binned as a direct function of mapped

unit boundaries, no clear correlation between thermophysical properties and surface composition is observed. These results indicate that significant ejecta distribution variability exists below the resolution of orbital thermophysical remote sensing data. Additionally, although a broad correlation between surface composition and grain size distribution exists, any defined compositional unit boundaries may be subject to distortion from erosional processes on even a geologically short time scale (~63 years). In addition to providing insights into how remote sensing data can improve field-based geologic mapping campaigns and impact crater analyses, our results place constraints on how the accuracy of geologic maps may break down due to surface mixing and erosion.

Introduction

Given their omnipresence in our solar system, impact craters serve as valuable tools for understanding the geologic history and environmental conditions of solid planetary surfaces. However, the success of such research relies on a robust foundational understanding of impact crater formation and breakdown mechanics. Airless bodies such as Mercury and Earth's Moon provide unique opportunities to study impact crater formation and subsequent degradation processes using orbital remote sensing datasets at visible, infrared, and microwave wavelengths. However, many small-scale features of common impact crater structures are unobservable at the current resolution scale of orbital remote sensing data, thus rendering our understanding of impact crater formation on other planetary bodies incomplete. Those minute morphological details are

best studied on Earth where in-situ field analyses of impact structures are feasible.

Barringer Meteorite Impact crater (hereafter referred to as Meteor Crater) is a ~1.2 km-diameter impact crater in northeast Arizona, USA exhibiting all attributes of a simple impact crater including a quasi-circular, bowl-shaped crater structure, a raised crater rim, and an observable ejecta blanket (Shoemaker, 1963; Shoemaker and Keiffer, 1974; Roddy, 1978; Kring, 2017). Due to its recent (~50 Ka) formation and the arid Holocene climate of the southwestern United States, Meteor Crater has undergone minimal erosion relative to other terrestrial impact structures. Thus, Meteor Crater is the most well-preserved terrestrial example of an impact structure with which to improve our understanding of the impact cratering process on Earth and beyond using the combination of geological field mapping and remote sensing techniques.

Remote sensing methods have long been employed in the analysis of Meteor Crater and other terrestrial impact structures. Early investigations utilized airborne image base maps to establish the first geologic maps of the Meteor Crater structure and associated ejecta deposit (Shoemaker, 1960; 1963). More recent analyses have utilized multispectral thermal infrared reflectance data, synthetic aperture radar data, and ground-penetrating radar data to deconvolve the composition, distribution patterns, and subsurface structure associated with the Meteor Crater ejecta deposit (e.g., Garvin et al., 1992; Wright and Ramsey, 2006; Roy and Stewart, 2012; Russell et al., 2013). However, those

investigations utilized data from airborne and orbital platforms with limited pixel resolution resulting in scale-dependent interpretations. Topics such as the exact grain size-frequency distribution, extent, and volume of the Meteor Crater ejecta deposit remain the subject of active research (e.g., Durda and Kring, 2015, Schmeider et al., 2017).

The objective of the work presented here is to identify grain size distribution patterns and ejecta boundaries associated with the Meteor Crater ejecta deposit using sUAS (small, Unmanned Aircraft System; hereafter referred to as a "drone") -based and orbital thermophysical data. A secondary objective of this work is to quantify sub-pixel mixing within orbital thermophysical data and identify the cause(s) of any observed variability in those data. We use diurnal surface temperature variations to derive the apparent thermal inertia (ATI) over portions of the Meteor Crater ejecta deposit (e.g., Kahle, 1987). ATI serves as a proxy for real thermal inertia – a thermophysical parameter that is sensitive to the grain size distribution and degree of induration at the surface of the Meteor Crater ejecta deposit. In the work presented here, the term "grain" is used in reference to surface rock fragments ranging in size from dust-sized particles to boulders in the Meteor Crater ejecta deposit. By measuring mapped ejecta units with the derived ATI data, our results will allow future work to place tighter constraints on ejecta distribution models and identify any unforeseen environmental factors that may influence such models. If such a correlation were observed in our work, it would indicate that high-resolution thermophysical data can be used to identify

and map ejecta facies based on physical characteristics such as effective grain size distribution in addition to geochemical signatures. If ejecta can be mapped via ATI and grain size data, our work would help to constrain the boundaries of the continuous ejecta deposit, the locations of distal ejecta lobes, secondary craters, the trajectory of the impactor, and the total volume of ejected material.

Background

Meteor Crater

Meteor Crater is a ~1.2 km-diameter impact crater in NE Arizona, USA that resulted from the hypervelocity collision of the Canyon Diablo bolide with Earth's surface, whose estimated mass is ~3.2 × 108 kg (e.g., Barringer, 1905; Shoemaker, 1960; 1963; Shoemaker and Kieffer,1974; Collins et al., 2016). The formation age of Meteor Crater is the subject of ongoing research but is currently inferred to be ~50 ka based on the combination of erosion rate extrapolation, dissolution pit analysis, shock metamorphosis thermoluminescence ages, and cosmogenic exposure ages of boulders at the crater rim (Jakosky et al., 1932; Blackwelder, 1932; Sutton, 1985; Phillips et al., 1991; Nishiizumi et al., 1991). The regional geology into which Meteor Crater formed includes the flat lying Permian Coconino and Toroweap sandstones overlain by the Permian Kaibab and Triassic Moenkopi formations, respectively. The Coconino sandstone is a fine-grained quartzose sandstone exhibiting massive cross beds and conjugate NW-SE and SW-NE joint sets with a spacing of ~5–10 m. With a thickness of ~210–240 m at Meteor Crater, the Coconino represents ~70% of the stratigraphic

depth excavated by the crater and is the oldest lithology disrupted by Meteor Crater. The Toroweap formation conformably overlies the Coconino and is composed of interbedded dolomite and sandstone. Past investigations and mapping efforts at the crater have used the singular term “Coconino” to describe both the Coconino sandstone and Toroweap collectively due to their conformable depositional history (Shoemaker, 1960; 1963). Hence, we employ a similar nomenclature in the present analysis where “Coconino” is used to describe both compositional units. The ~80-m-thick Kaibab formation is composed of fossiliferous interbedded dolomites, dolomitic limestones, and sandstones and is separated into three primary (alpha, beta, and gamma) members each representing unique depositional environments. Like the Coconino, the Kaibab exhibits two conjugate joint sets with NW-SE and SW-NE orientations with an average spacing that is slightly closer than the Coconino joint sets at ~1–3 m (Kumar et al., 2010). Lastly, the Moenkopi Formation is composed of the lower Wupatki member shale and the upper Moqui member siltstone and sandstone. The thin (~9 m-thick) Moenkopi formation unconformably overlies the Permian Coconino sandstone and Kaibab formations and is among the uppermost members of the Grand Canyon Sequence – to which all four excavated lithologies belong. Collectively, these lithologies were excavated during the formation of Meteor Crater and are exposed within the surrounding ejecta deposit in an annular pattern that is generally inverse to their subsurface stratigraphic

order. For complete descriptions of all units, see Roddy, (1978) and Kring (2017; Ch. 2).

The continuous ejecta deposit associated with Meteor Crater is the focus of the work presented here. The compositional units that comprise the Meteor Crater ejecta deposit were initially deposited in an inverse stratigraphy relative to their pre-impact stratigraphy (e.g., Roddy, 1978). Moenkopi ejecta material is represented at the base of the ejecta layer sequence superposed by Kaibab and Coconino ejecta respectively. Coconino ejecta (i.e., the deepest excavated lithology) is predominantly represented at the south crater rim with Kaibab and Moenkopi emplaced at increasing distances from the rim in all directions, respectively. Although post-deposition erosion has heavily modified the ejecta deposit, remnants of these patterns may still be observed in many areas around the crater. The largest excavated ejecta fragments (boulders) are typically present at the crater rim with mean fragment size decreasing as a function of radial distance away from the crater (Gilbert, 1896). Also apparent within the ejecta are a series of concentric, topographic ridges that are the result of shearing within the ejecta blanket during deposition (Kring et al., 2011a; b). Extensive surface mapping and coring campaigns have estimated that ~175 million tons of material were excavated during crater formation and deposited within the surrounding ejecta deposit. However, only ~73% of that material is represented in the modern continuous ejecta deposit out to an average distance of ~1.89 crater radii from the crater rim, with the rest of the excavated material

represented as alluvium due to weathering or deposited elsewhere as distal ejecta (e.g., Roddy et al., 1975).

Although Meteor Crater is considered to be the most well-preserved terrestrial impact structure due to its youth, the predominantly arid climate of the southwestern United States, the crater and associated ejecta deposit has been subjected to significant erosional processes. Estimates in deflation or vertical erosion range from ~15–20 m at the crater rim to <1 m farther out in the ejecta deposit (Shoemaker and Kieffer, 1974; Nishiizumi et al., 1991; Grant and Schultz, 1993). Since the time of crater formation (~50,000 ka), periods of extended pluvial conditions at the crater have altered many of the original depositional patterns and structures within the Meteor Crater ejecta deposit. Evidence for those wetter climatic conditions comes in the form of Pleistocene lacustrine sediments at the bottom of Meteor Crater indicating the past existence of a ~10 m-deep lake (e.g., Barringer, 1905; Shoemaker, 1960; Reger and Batchhelder, 1971; Shoemaker and Kieffer, 1974; Roddy, 1978). The pluvial climatic conditions that led to lake formation would have been favorable for chemical weathering of Kaibab limestone, and, to a lesser degree, Coconino sandstone ejecta fragments. While those chemical weathering mechanisms still persist in modern times due to infrequent precipitation at the crater, the physical weathering mechanisms of thermal fatigue and aeolian erosion are the most consistent weathering mechanisms acting on the Meteor Crater ejecta deposit in modern times. Both past and present weathering mechanisms have contributed

to significant alteration of individual rocks within the Meteor Crater ejecta deposit as well as the distribution of those rocks.

Thermophysical Remote Sensing

Thermal inertia (I) can be thought of as a material's resistance to change in temperature and is defined by:

$$I = (k\rho c)^{½} \quad (1)$$

where k represents bulk thermal conductivity (W/ m K), ρ represents the density (g cm^{-3}) of the material, and c is the specific heat capacity (cal g^{-1} K^{-1}) of the material (e.g., Price, 1977; Kieffer et al., 1977; Putzig, 2006). Relative to bulk thermal conductivity, which can vary by several orders of magnitude, density and specific heat capacity only vary by a factor ~2 for a geologic surface with little or no moisture content. The bulk thermal conductivity of a surface is directly related to the thermal conductivity of the interstitial gas, the amount of pore space within the system, and the thermophysical properties of solid materials within the soil or regolith (e.g., Presley and Christensen, 1997; Piqueux and Christensen, 2009). Since the effective pore space of a loosely consolidated, geologic material is commonly proportional to grain size, the thermal inertia of a dry, unconsolidated surface is most affected by the rock grain size distribution or degree of induration (e.g., Presley and Christensen, 1997; Fergason et al., 2006). For example, everything else being equal, a surface with a larger effective grain size or higher degree of induration will exhibit an increased resistance to temperature fluctuations (lower ΔT) as a result of the higher thermal inertia of that surface.

While the effective grain size of unconsolidated materials exhibits a dominant control on thermal inertia, rock mineralogy can also be observed to affect thermal inertia in a significant way. This dependence of thermal inertia on surface mineralogy is particularly relevant for sedimentary rocks that can exhibit considerable variability in density and thermal conductivity (Gupta, 1991). Past work has reported thermal inertia values of 0.034, 0.054, and 0.045 $cal/cm^2/s^{1/2}/°C$ for shale, sandstone, and limestone respectively (Gupta, 1991 - their table 12.1). Those thermal inertia values were estimated assuming a continuous slab of solid rock, however. While an important consideration for the work presented here, the effects of mineralogy on the thermal inertia of unconsolidated sediments are unlikely to overcome the contributions of surface grain size distribution – which can vary by several orders of magnitude for a given surface.

From a remote sensing standpoint, true thermal inertia is not readily determinable for a terrestrial surface due to the variable effects of environmental conditions on bulk thermal conductivity and the inability to directly obtain density and specific heat capacity via the measurement of reflected or emitted photons from that surface (e.g., Kahle, 1987). In the work presented here, we utilize surface temperature data (~90 m/pixel) and reflectance data (~30 m/pixel) from the Advanced Spaceborne Thermal Emission and Reflection Radiometer (ASTER) instrument onboard the NASA TERRA satellite to derive apparent

thermal inertia (ATI) as a proxy for true thermal inertia due to the aforementioned limitations. The ATI of a surface is defined by:

$$ATI = (1-A)/\Delta T \quad (2)$$

where A represents surface albedo and ΔT represents the diurnal change in surface temperature (Price, 1977; Kahle, 1987). Similar to past investigations of surface ATI, the effects of solar incidence angle on ATI are disregarded for simplicity (e.g., Price, 1977; Kahle, 1987; Sabol et al., 2006). ASTER level 2 surface temperature data are corrected to account for atmospheric effects, so the effects of atmospheric absorption on thermal infrared data do not affect our ATI measurements. The albedo data used for our ATI derivation is calculated from ASTER VNIR bands 1 & 3 using the methods of Mokhtari et al. (2013) and the empirically derived equation:

$$A = 0.697 \times b1 + 0.298 \times b3 + 0.008 \quad (3)$$

where b1 represents Band 1 and b3 represents Band 3 of the ASTER VNIR instrument.

Past Work

Past investigations have utilized in-situ field methods, drill-coring campaigns, and ground penetrating radar techniques to establish the extent and spatial characteristics of the Meteor Crater ejecta deposit and the compositional units therein (e.g., Shoemaker, 1963; Roddy et al., 1975; Russell et al., 2013). Most pertinent to the work presented here is the surface distribution of Meteor Crater ejecta and the unit boundaries that have been defined via extensive field

mapping efforts and in-situ measurements (e.g., Shoemaker, 1960; 1963 – Fig. 3.1a). That mapping effort was conducted using a ~5 m observation scale resulting in an equivalent spatial uncertainty on defined unit boundaries. In addition to that scale-based uncertainty on defined unit boundaries, larger-scale inconsistencies between unit contacts identified in this work and those delineated in the original map of the Meteor Crater ejecta deposit have been noted in several locations around the crater. Such inconsistencies will be discussed further in the results section of this work. Hence, validation of unit boundaries within the ejecta along with the complete extent of the ejecta blanket remain subjects of active research (e.g., Schmieder et al., 2017).

Prior remote sensing investigations of Meteor Crater have utilized thermal infrared data from the ASTER and Thermal Infrared Multispectral Scanner (TIMS) instruments for the purposes of spectral deconvolution of discrete lithologies within the ejecta of Meteor Crater (Ramsey, 2002; Wright and Ramsey, 2006). Although a trend of decreasing effective grain size with distance from the crater rim was noted, the primary focus of these investigations was to define lithologic diversity within the ejecta deposit and to test the suitability of similar methods for analysis of impact craters on Mars. A recent investigation of ejecta grain size frequency distribution used boulder counting methods across the continuous ejecta deposit of the crater (Durda and Kring, 2015). Preliminary results of that work indicate a non-uniform distribution of boulders around the craters and an increased effective grain size associated with Kaibab ejecta,

followed by Coconino and Moenkopi ejecta, respectively. The work presented here builds on these prior investigations as the first analysis to utilize a combination of orbital and drone-based remote sensing data to characterize the surface grain size distribution associated with each compositional unit within the Meteor Crater ejecta deposit.

Thermophysical data products are commonly used in characterizing surface grain size distributions in studies of other planetary bodies (e.g., Jakosky, 1986; Mellon et al., 2000; Bandfield et al., 2011; Hayne et al., 2017). Martian surface conditions, grain size distribution patterns, and geologic history have been inferred on a global scale using thermophysical data from multiple orbital assets including Mariner 9 (Kieffer et al., 1973), Viking IRTM (Infrared Thermal Mapper) (e.g., Kieffer et al., 1977), Mars Global Surveyor (MGS) Thermal Emission Spectrometer (TES) (e.g., Mellon et al., 2000; Putzig, 2006), and Mars Odyssey Thermal Emission Imaging System (THEMIS) data (e.g., Ferguson et al., 2006). Likewise, lunar surface temperature data from the Clementine long-wave infrared (LWIR) camera and the Diviner thermal radiometer onboard the Lunar Reconnaissance Orbiter (LRO) have been used to estimate the meter-scale roughness of the lunar surface, the thermal inertia of the lunar surface, and the porosity of the upper lunar regolith (e.g., Lawson and Jakosky, 2001; Bandfield et al., 2011; Hayne et al., 2017). These derived datasets are commonly extrapolated to infer lunar surface ages, surface unit boundaries, and regolith evolution rates (Ghent et al., 2014; 2016; Nypaver et al., 2021; Williams et al.,

2022). Such interpretations pertaining to the lunar and martian surfaces are limited by the spatial resolution of the orbital data used in those investigations (i.e., 237 m/pixel Diviner Rock Abundance data and ~100 m/pixel Mini-RF radar data) that frequently prohibits the observation of meter and decameter-scale trends and features. By comparing orbital thermophysical measurements of a similar scale to those used on other planetary bodies with higher-resolution drone-based data, our work will help to inform those prior investigations by defining sub-pixel data and process variability.

Methods

ASTER data

The orbital data used in this investigation were collected by the ASTER instrument onboard the NASA TERRA satellite (e.g., Yamaguchi et al., 1998). ASTER is a multispectral instrument in a sun-synchronous polar orbit with an 05:30/18:30 equatorial crossing time. The instrument possesses three visible-near infrared (VNIR) bands in the 0.51–0.86 μm region, six short wave infrared (SWIR) bands in the 1.6–2.43 μm region, and five thermal infrared (TIR) bands in the 8.125–11.65 μm region. The ASTER kinetic surface temperature (AST_08) data used in this work are derived from the ASTER TIR bands and are publicly available through the NASA Earthdata search portal (https://search.earthdata.nasa.gov/search) with a native resolution of ~90 m/pixel. This work also makes use of the ASTER VNIR radiance data for the purpose of surface albedo derivation and ATI calculation using Equation 2.

Those VNIR data are also available from the Earthdata search portal with a resolution of ~30 m/pixel. The ASTER crossing times over Meteor Crater are ~05:30 and ~18:30. Hence, the specific surface temperature images used for this analysis were a single daytime image (AST_08_00307032004182036_20221213100657_10582) collected on 07-03-2004 at 18:20:36 and a singular nighttime image (AST_08_00301232018052930_20210308134058_21100) collected on 01-23-2018 at 05:29:30.

Drone-based Data Collection

Our work draws comparisons between the aforementioned ASTER-derived thermophysical measurements and surface temperature measurements collected via a FLIR (Forward Looking InfraRed) Vue Pro 640 R radiometric thermal camera with a 9 mm lens attached to a DJI Phantom 4 Pro sUAS (Fig. 3.2). Drone-based data collection was limited by both weather conditions and flight duration/battery capacity. Given the prevalence for strong winds in the vicinity of Meteor Crater, data collection was conducted in the late spring (May 17–18, 2022), when conditions tend to be more quiescent. Ambient temperatures at the time of data collection ranged from 8.3–32.8°C, wind speeds at the time of data collection ranged from 4.8–45.1 kph, and sunrise/sunset times were 05:19 and 19:22, respectively. Drone-based surface radiance measurements were collected over five separate ~90 × 110 m regions of interest (ROIs) within the Meteor Crater ejecta blanket. Those radiance measurements are then readily converted

to radiant surface temperature in real time by the FLIR camera under the assumption that the surface has an average emissivity of 1.0. Thus, surface temperature measurements were acquired for all five ROIs (Fig. 3.3). Individual ROIs were selected based on accessibility and the presence of multiple mapped lithologic units in each ROI. ROIs 1–2 were located in the NE quadrant of the ejecta deposit approximately ~500 m from the crater rim, ROI 3 was located directly on the S/SE crater rim, and ROIs 4-5 were located in the SE and SW quadrants of the crater ejecta, respectively, at distances of ~500 m from the crater rim (Fig. 3.3). Pre-dawn (~05:00–05:30) and afternoon (~14:00–14:30) surface temperature images with a spatial resolution of ~23.4 cm/pixel were collected by maintaining a hover at ~60 m altitude over each ROI for 3–5 minutes. Images were collected at 1-second intervals in order to account for an internal recalibration of the FLIR camera. The timing and nature of this recalibration are largely proprietary to FLIR, but the recalibration is designed to account for temporal drifting in measured radiance and radiant temperature readings due to warming of the camera housing. The time intervals between recalibration shifts are unpredictable, but the measurements are consistently reset to a real surface radiance/surface temperature after each recalibration shift. By collecting data at 1-second intervals for extended periods of time (<5 mins), we ensured that at least one recalibration shift occurred during data collection. It was those post-recalibration images that were used for our analysis. For georeferencing purposes, we also collected high-resolution (~1.3 cm/pixel)

orthophoto mosaics over each ROI using the 20 Mpixel RGB camera onboard the DJI Phantom 4 Pro drone.

Data Processing Methods

The day and nighttime ASTER images were downloaded from the Earthdata search portal in geotiff format and ingested directly into ESRI's ArcGIS Pro 3.0 over a USGS orthophoto mosaic basemap of Meteor Crater. The ASTER VNIR band 1 & 3 data were also ingested into ArcGIS Pro and converted into an albedo image using the ArcGIS Pro raster calculator and Equation 1. Once projected in ArcGIS Pro, the raster calculator tool and Equation 2 were used to create an ATI image over the crater using the daytime, nighttime, and albedo images. Drone-based surface temperature image pairs were used to create ATI images in a manner similar to that used for the ASTER ATI. The individual ROI surface temperature images were ingested into ArcGIS and georeferenced using visible surface features (boulders, vegetations, and human-placed items) as tie points between the high-resolution orthophoto mosaics and the thermal images. Each ROI surface temperature image was georeferenced using no fewer than 10 tie points and a spline fitting function. The spline fitting function accounted for a conical distortion that was inherent in the drone-based images, but positional offsets on the order of ~2–3 m were still present at the edges of those images in some cases. After each drone-based surface temperature image was georeferenced and projected in ArcGIS Pro, Equation 2 was used to calculate ATI for each ROI. In Equation 2, ΔT represents the total change in surface

temperature throughout the day. Due to time constraints and wind conditions during drone-based data collection, it was difficult to collect data during the exact warmest and coolest points of the day. Hence, our method is an oversimplification of ATI – which, itself, is a simplification of thermal inertia. Given the short timeframes in which drone data were collected in the pre-dawn and mid-afternoon hours (~20–30 mins) and the minimal diurnal temperature fluctuations in that timeframe, we expect that this simplification contributes to minimal variations between different ATI images. Moreover, data collection time discrepancies are unlikely to contribute any variation to relative unit variations within individual ATI images.

Since albedo data were not collected using the drone-based instrumentation, ASTER albedo was used in the calculation of ATI over the individual ROIs. The method of broadband albedo estimation used here was developed and tested by prior work (Mokhtari et al., 2013). Through ground-based validation of similar models and a linear regression analysis of the model data with artificial neural network-derived albedo, those authors determined that the derived data served as an accurate representation of surface broadband albedo. However, there is still a possibility that the large pixel size (30 m/pixel) conceals some amount of real surface albedo variability below the resolution of the data. An additional complication of using coarse-resolution (30 m/pixel) albedo data and high-resolution (0.025 m/pixel) drone-based surface temperature data to calculate ATI is a cross-hatching artifact in the resulting images. This artifact represents the

pixel boundaries of the ASTER albedo data in areas where neighboring ASTER albedo pixels were significantly variable (>50% difference in albedo value). Considering the self-similarity of albedo values (<10% difference) for most the Kaibab ejecta, Moenkopi ejecta, and Alluvium, we expect this artifact to have a negligible effect on the presented results for ROIs 1,2, 4, and 5. For example, a 10% difference in albedo for neighboring pixels with equivalent ΔT values would result in a 2.4% difference in ATI for those pixels. However, at the crater rim (ROI 3) ASTER albedo pixel values vary by an order of magnitude (0.06–0.29). This range of ASTER albedo values in ROI 3 has the potential to induce the above-mentioned cross-hatching artifact into our derived ATI data. Moreover, since the lower albedo region of ROI 3 is spatially coincident with the north-sloping, slightly shadowed inner crater rim and the Kaibab ejecta within that region, the derived Kaibab ATI in that ROI is likely to be elevated relative to other Kaibab ejecta material throughout the ejecta. The elevated albedo associated with the Coconino ejecta in ROI 3 is expected given the predominantly white coloration of the quartzose sandstone that comprises the unit.

Before measuring the ATI data over pre-defined ejecta unit boundaries, control ATI values were first established to provide the best possible representative ATI values for each lithology in the Meteor Crater ejecta deposit. To establish these baseline ATI values, 10 × 10 m sampling areas were drawn within the boundaries of a given unit and the ArcPro Zonal statistics tool was used to extract mean and standard deviation drone-based ATI values for that unit

(Fig. 3.S7). Because these sampling areas were selected to avoid unit boundaries, areas of clear fluvial or aeolian erosion, and areas of human disturbance, the resulting ATI values ideally serve as baseline ATI values for each lithology with which to compare other ATI measurements. With control ATI values established, the ArcPro Zonal Statistics tool was first used to extract mean and standard deviation values of drone-based ATI values within previously established unit boundaries (Shoemaker 1960; 1963) represented in each ROI. The unit boundaries used to bin the drone-based ATI values were digitized versions of the boundaries defined in the original geologic mapping of Meteor Crater. While care was taken to ensure that every ROI contained at least two distinct lithologies and one unit boundary, no ROIs contained all four lithologies represented in the ejecta deposit (i.e., Kaibab, Coconino, Moenkopi, and alluvium). All discernable vegetation was digitally clipped from the sampling to ensure accurate estimates of ATI of the ground surface only within each defined unit. The digital clipping of all discernable vegetation resulted in the exclusion of <5% of the drone-based ATI data from analysis.

The ArcPro Zonal Statistics tool was also used to extract mean and standard deviation values of ASTER ATI in a manner similar to that of the drone-based data. The polygon features used to bin ASTER ATI data were the same as those used to sample the drone-based data (i.e., digitized versions of the units defined in the original geologic mapping of Meteor Crater). In the case of the ASTER ATI, the pixel resolution of the data (90 m) is much larger than the scale at which the

original Meteor Crater geologic map was compiled. To account for this discrepancy, the ASTER ATI data within each geologic unit were sampled using a 0.025 m grid within the respective unit boundaries. This artificial upsampling of the ASTER data weights the resulting ATI average value based on the area of that unit within a given pixel (Fig. 3.S8).

One alternate method of ATI calculation to that utilized here is to bin the drone-based data in spectral radiance space as opposed to directly binning the ATI data created using band math operations in conjunction with albedo and temperature images over the entirety of a given ROI (i.e., the method described above). In theory, this alternate radiance binning method would better account for the non-linear dependence of radiance on temperature ($\sim T^4$) described by the Stefan-Boltzmann Law. However, the radiance-binning would be more computationally intensive due to additional averaging of the radiance data and the conversion of those back to temperature data using an inverse Planck function. In order to compare the validity and effectiveness of these two methods for calculating ATI, we conducted a test wherein ATI was calculated using both the ATI-binning (i.e., “direct-binning”) and radiance-binning methods (Table 3.1). The temperature data output by the FLIR camera were first converted back to radiance centered at 10.5 μ. The radiance data were then binned using the original compositional unit boundaries within ROI 3, and those mean radiance values were converted back to temperature using an inverse Planck function calculator publicly available from the National Oceanic and Atmospheric

Administration (NOAA - https://ncc.nesdis.noaa.gov/Planck.php). Once re-converted back into temperature space, the data were used to calculate ATI using Equation 2. The resulting ATI data were then directly compared to the temperature-binned ATI data associated with the compositional units in ROI 2 to assess differences between the two result sets. The ATI data produced via the radiance binning method are statistically inseparable from those produced using the temperature binning method (<0.02% difference). Hence, we rely on the temperature binning method in the work presented here due to the reduced computational load associated with that method.

Results

The overall distributions of drone-based ATI data associated with each compositional unit represented in the Meteor Crater ejecta deposit are presented in Figure 3.4. Each histogram represents the combined distribution of drone-based ATI data for each compositional unit sampled across all ROIs with the thermophysical effects of surface vegetation digitally clipped from the data. The distribution of Alluvium, Coconino, and Moenkopi ejecta ATI appear unimodal and non-gaussian in nature. However, the distribution of Kaibab ejecta ATI is more narrowly distributed than the other three units with a peak at 2.1×10^{-2} – 2.7×10^{-2} T^{-1} and secondary peak at 3.5×10^{-2} T^{-1} indicating a slight bimodality associated with the Kaibab ATI data.

The drone-derived control ATI values (i.e., the ATI values that were collected well away from unit boundaries or obvious areas of enhanced surface erosion)

indicate that the Coconino sandstone exhibits the highest ATI, followed by the Kaibab, alluvium, and Moenkopi, respectively (Fig. 3.5a). Those control ATI values are statistically separable via a difference of means test. The ASTER-derived ATI values for those same units are consistent with the relative control values in that the Coconino exhibits the highest ATI, followed by the Kaibab, alluvium, and Moenkopi, respectively. However, ATI values derived via the ASTER data are less quantitatively separable than the drone-based control values. The ASTER ATI values also appear to be systematically lower than the control ATI values. Such an offset is likely due to the ~18:20 orbital passing time of the TERRA satellite over Meteor Crater and the higher kinetic surface temperatures associated with that time of day. Additionally, variations between ASTER and drone-based ATI values may result from differences in weather or environmental conditions at the time of data collection as well as inherent differences in the instrument architecture. However, those differences are unlikely to result in relative variability between discrete compositional unit ATI values The concentric binning of ASTER ATI data around the craters also reveals an exponential decrease in ATI from 1.6×10^{-2} T^{-1} at the crater rim to a background ATI value of 1.3×10^{-2} T^{-1} at a distance of ~800 m from the crater rim (Fig. 3.5b).

The drone-based ATI data exhibit more variability and less quantitative agreement with the ATI trends derived via ASTER data. In drone-based data, the Kaibab ATI was higher than the alluvium and Coconino ATI in ROIs 1, 2, and 3.

However, while the Kaibab ATI was higher than the Moenkopi ATI in ROI 5, the Moenkopi ATI was elevated above the Kaibab ATI in ROIs 2 and 4 (Fig. 3.5a, Table 3.2). The Coconino and Kaibab ATI values in ROI 3 were also elevated relative to the other four ROIs. Hence, no clear correlation between ATI and previously mapped geologic unit boundaries can be discerned using high-resolution, drone-based ATI. Several possible explanations for the observed dissociation between thermophysical and compositional unit boundaries are evaluated in the discussion below. Similar to the relationship between the control ATI values and the ASTER ATI, drone-based ATI values in every ROI were elevated relative to the ASTER-equivalent unit ATI.

Discussion

The distribution of Meteor Crater ejecta material is well-behaved at the scale of the ASTER ATI data. Given the loose compaction of surface material and minimal induration within the Meteor Crater ejecta deposit, we assume that rock grain size variations are the primary control on ATI variations observed in this work. Under such an assumption, the radial decrease in ASTER ATI is consistent with a decrease in ejecta grain size with distance from the crater rim. This observation is also consistent with early observations of the boulder distribution around Meteor Crater (e.g., Gilbert, 1896) as well as observations of ejecta distribution patterns on the Earth's Moon (e.g., Bart and Melosh, 2010; Watkins et al., 2019). The unit-based differences in ASTER ATI indicate that the Coconino ejecta exhibits the largest effective grain size, followed by Kaibab

ejecta material, alluvium, and Moenkopi, respectively. That grain size distribution (i.e., Coconino, Kaibab, alluvium, Moenkopi, respectively) is consistent with the distribution of drone-based, control ATI values, but the quantitative difference (separability) between those control ATI values is substantially greater than in the ASTER dataset. A larger effective grain size associated with Kaibab and Coconino ejecta material is also supported by a prior finding of increased boulder size-frequency distribution associated with those units relative to Moenkopi within the Meteor Crater ejecta deposit (Durda and Kring, 2015).

Drone-based ATI data provide an additional level of geologic detail that is indiscernible in the ASTER orbital ATI data. The overall distribution of drone-based ATI data associated with each compositional unit indicates that the Coconino ejecta material exhibits the highest mean ATI, followed by Kaibab ejecta and Moenkopi ejecta, respectively. Such a ranking is consistent with the expected mineralogy-based differences in thermal inertia for sandstone, limestone, and siltstone. However, since Coconino and Kaibab ejecta have also been observed to exhibit the largest effective grain size distribution in optical data (Durda and Kring, 2015), it is possible that both grain size distribution and mineralogical effects could be playing a role in the observed distribution of ATI values within the Meteor Crater ejecta deposit. Given the increased dependency of thermal inertia on bulk density of unconsolidated materials, such as ejecta, it remains likely that grain size distribution exhibits a dominant control on the ATI data collected here (e.g., Presley and Christensen, 1997; Fergason et al., 2006).

The anisothermality of the Meteor Crater ejecta is readily apparent in the non-long-tailed distributions of unit ATI (Fig. 3.4). The anomalously high ATI values in those histograms are the result of high-ATI boulders with each field of view. This effect is most apparent in the Kaibab ATI distribution which exhibits a narrow ATI peak at $2.1 \times 10^{-2} – 2.7 \times 10^{-2}$ T^{-1} and secondary, less intense peak at 3.5×10^{-2} T^{-1}. This slight bimodality is indicative of the excess of boulders present in Kaibab ejecta relative to the other compositional units within the ejecta (e.g., Kring, 2017; Durda and Kring, 2015). The other units within the ejecta do not exhibit this same bimodality and are, therefore, less affected by point anomalies within the ATI data.

In the five ROIs sampled here, no clear correlation between drone-based ATI values binned by previously established compositional unit boundaries (Shoemaker, 1960; 1963) is observable. The drone-based ATI data for ROIs 1, 3, and 5 indicate that Kaibab ejecta exhibits the largest effective grain size in those areas whereas the ATI data for ROIs 4 and 5 indicate that Moenkopi ejecta exhibits a larger effective grain size distribution than the Kaibab and alluvium material in ROIs 4–5. The Kaibab and Coconino ATI values derived for ROI 3 are significantly elevated relative to the other drone-based ROI ATI values as well as to the overall ASTER ATI values for those units.

Given the distinct and separable nature of the control ATI values, the lack of an apparent correlation between the mapped geologic units within the Meteor Crater Ejecta deposit and high-resolution ATI data is likely a result of both syn

and post-depositional mixing across unit boundaries as well as uncertainty in the placement of geologic contacts. Past climatic conditions in the Meteor Crater region were far wetter than they are currently, thus enhancing fluvial erosion of the crater and associated ejecta (e.g., Spaulding and Graumlich, 1986; Kumar et al., 2010; Kring, 2017). Currently, aeolian processes are the dominant erosional agent for modifying the Meteor crater structure and ejecta blanket (e.g., Kring, 1997; Grant and Schultz, 1993; Kumar et al., 2010). Second to wind-driven erosion are modern fluvial processes that result from less frequent rainstorms and snow melt in the desert southwest (e.g., Kumar et al., 2010). Meteor Crater has also been subjected to excavation and mining operations as well as human recreational activities and frequent grazing from cattle (e.g., Fairchild, 1907; Fig. 3.S9). The combined effect of these processes is an ejecta surface that is dissimilar to the originally deposited eject blanket in many ways. Past estimates of erosion for the Meteor crater range from <1.0 vertical meter in the continuous ejecta to >15.0 vertical meters at places along the crater rim (e.g., Shoemaker and Keiffer, 1974; Grant and Schultz, 1993). Much of this erosional deflation results from aeolian and fluvial processes stripping fine grained material from the surface and leaving behind larger, immobile rock fragments. Such a process would likely result in increased surface ATI values. Additionally, chemical and physical weathering processes systematically reduce larger rocks and boulders into smaller fragments, thereby reducing ATI. The balance of these processes is complex, and local variability in the intensity of each of the aforementioned

weathering mechanisms has the potential to alter the effective grain size distribution of the original ejecta deposit and cause mixing of material across unit boundaries. This mixing of unconsolidated sediments across unit boundaries (i.e., horizontal erosion within the ejecta deposit) can be observed within several of our drone-based ATI images. For example, in ROI 5, the Kaibab ejecta material is mapped as a NW-SE trending unit bounded by Moenkopi ejecta to the east and west (e.g., Shoemaker, 1960; 1963). In our drone-based ATI data, however, the unit boundary between the high-ATI Kaibab and low-ATI Moenkopi ejecta appears to be extended up to ~10–20 m beyond the original unit boundary into the unit previously defined as Moenkopi ejecta (Fig. 3.6). One explanation for this dissimilarity between the original Kaibab-Moenkopi geologic unit boundary in ROI 5 (Shoemaker, 1960) and the thermophysical unit boundary observed in our drone-based ATI data is a horizontal mixing of units due to the above-mentioned erosional processes. Offsets of similar magnitudes (~10–20 m) can be observed in ROIs 1 and 2 associated with alluvium, Kaibab, and Moenkopi unit boundaries.

All potential sources of variability in the drone-based ATI values discussed here must be considered when using remote sensing data to characterize surface geology on Earth and other planetary bodies. Impact-induced churning of the lunar regolith and aeolian erosion and sediment deposition on Mars are processes that have the potential to dissociate mapped geologic contacts from unit boundaries discerned in remote sensing observations. Our observations are corroborated by past work on the thermal properties of the martian surface

(Mellon et al., 2000). Those authors found a weak correlation between geologic unit boundaries and thermophysical unit boundaries on a global scale. The observed anticorrelation between thermophysical and geologic units in that work was not unexpected and was attributed to the aeolian mantling of martian surface dust over compositional unit boundaries.

In addition to erosion-induced transport of material across ejecta unit boundaries, error associated with the definition of the unit boundaries themselves may be a cause of the observed disparities between the control ATI values and those measured via pre-defined unit boundaries. Prior work has noted several areas within the ejecta deposit where the defined unit boundaries appear to be inconsistent with the currently observable geologic contacts (Schmeider et al., 2017). Any error associated with the ejecta unit boundaries defined in the original map of Meteor Crater is likely the result of the ~5 m observation scale associated with that mapping effort. This error associated with defined unit boundaries propagates into the ATI measurements presented here and may induce unintended mixing of unit ATI data across unit boundaries. In the work presented here, however, we cannot deny the accuracy of previously mapped unit boundaries using aerial remote sensing data collected and presented here as our work is not systematically corroborated by in-situ field measurements. Such a limitation highlights the need for parallel field mapping campaigns in remote sensing investigations such as this one to strengthen remote observations with limited resolution capabilities.

Although, discrepancies and sources of error challenge the likelihood of a ubiquitous correlation between mapped geologic units and the thermophysical properties of the surface, the combination and comparison of low-resolution orbital and high-resolution drone based thermophysical data still yields several new insights about the distribution of the Meteor Crater Ejecta deposit and the use of thermophysical data for the characterization of surface geology. The ejecta unit grain size hierarchy observed in the ASTER and control ATI data (i.e., Coconino, Kaibab, alluvium, and Moenkopi, respectively) might be explained via the combination of pre-existing structure within those units, the compositional makeup of each unit, and the variable effects of erosion on units of differing lithology. Based on the ASTER and control ATI values, Coconino ejecta exhibit the largest effective grain size on average, followed by Kaibab ejecta material. The Coconino sandstone was the deepest unit excavated during the formation of Meteor Crater. As such, the Coconino was subject to the lowest shock-pressures of any other unit during the excavation, resulting in the coarse fragmentation of that unit and the deposition of that coarse material close to the crater rim. Similarly, the thickness and stratigraphic placement of the Kaibab likely contributes to the coarse grain size of the associated ejecta material. Relative differences in grain size distribution between these two units may also be the result of pre-existing structural control from the wider (~5–10 m) spacing of the joints associated with the Coconino relative to the narrower (~1–3 m) joint spacing associated with the Kaibab (Roddy, 1978; Kumar and Kring, 2008). The

fine-grained nature of the Moenkopi ejecta is expected given the susceptibility of shocked siltstone to physical and chemical weathering processes. An effective alluvium grain size that is greater than that of Moenkopi ejecta, but lower than that of Kaibab or Coconino ejecta is reasonable since the alluvium is a heavily weathered mixture of all three units.

Conclusions

In the work presented here, we utilize a combination of orbital and drone-based thermophysical data to characterize the extent, surface grain size-frequency distribution, and erosional state of the Meteor Crater ejecta deposit. Based on the results of this investigation, we put forth the following conclusions:

- A correlation between compositional unit and bulk grain size frequency distribution is discernible using the combination of previous field-based mapping and drone-based and orbital apparent thermal inertia (ATI) data. Both the ASTER and control drone-based ATI data indicate that Coconino ejecta material exhibits the largest effective grain size, followed by Kaibab, alluvium, and Moenkopi, respectively. The larger effective grain size associated with Coconino and Kaibab ejecta material is supported by past analyses of boulder distributions around the crater, and likely results from the combination of pre-existing structure and relative excavation depths associated with each of those units. It should also be noted that the observed unit-based variations in

ATI may also partially be a result of the variably effects of mineralogy on thermal inertia.

- When binned using previously defined compositional unit boundaries (Shoemaker 1960; 1963), no definitive correlation between ATI and ejecta composition is observed. The observed variability is likely a result of erosion-induced mixing of unconsolidated surface material across unit boundaries and, to a lesser degree, observation scale-based errors associated with the original identification of the unit boundaries. Based on the spatial differences between previously defined map boundaries and those observed in our drone-based ATI data, the combination of aeolian, fluvial, and human-induced erosion has caused ~10−20 m of horizontal erosion (i.e., sediment transport) within the Meteor Crater continuous ejecta deposit since the original geologic mapping of the crater.
- Details associated with the spatial distribution and structure of km-scale impact crater ejecta deposits exist below the resolution of most orbital data sets and are only discernible using high-resolution remote sensing data or in-situ field mapping methods. To a first order, this finding is evident in the observation that the mapped compositional unit boundaries associated with the Meteor Crater ejecta deposit are in no way discernable using the low-resolution (90 m/pixel) ASTER thermophysical data used here. Higher-resolution, drone-based

thermophysical data allow for a more precise assessment of ejecta grain size distribution but given the limited sensitivity of those data to the upper layers of a surface, higher 108esoluteion thermophysical data appear more well suited to characterize the erosional state of a surface rather than compositional variability.

The work presented here highlights the usefulness of drone-based high resolution thermophysical data in analyzing impact crater ejecta. Moreover, by comparing those high-resolution thermophysical data with lower-resolution orbital data and geologic map boundaries defined via field mapping methods, we identify several key limitations in the use of orbital remote sensing data for assessing planetary surface conditions and drawing geologic interpretations. These results inform similar investigations of impact ejecta deposits on other planetary bodies using orbital remote sensing data. However, the data presented here — and the ability to draw robust interpretations over the entirety of the ejecta deposit based on those data — are limited in scale. Future work should focus on the acquisition of high-resolution thermophysical and hyperspectral data over the entirety of the Meteor Crater ejecta deposit and beyond for a more complete understanding of the intricacies associated with high resolution thermophysical analyses.

References

Bandfield, J. L., Ghent, R. R., Vasavada, A. R., Paige, D. A., Lawrence, S. J., & Robinson, M. S. (2011). Lunar surface rock abundance and regolith fines temperatures derived from LRO Diviner Radiometer data. Journal of Geophysical Research: Planets, 116(E12).

Barringer, D.M. (1905). Coon Mountain and its crater. Proceedings of the Academy of Natural Sciences of Philadelphia, v. 57, pp. 861-886.

Bart, G. D., & Melosh, H. J. (2010). Distributions of boulders ejected from lunar craters. Icarus, 209(2), 337-357.

Blackwelder, E. (1932). The age of Meteor Crater. Science, 76(1981), 557-560.

Collins, G.S., Mason, K.D., and Kring, D.A. (2016) Numerical modeling of Meteor Crater: Simple crater formation in a layered sedimentary target. 79th Annual Meeting of The Meteoritical Society, Abstract #6418.

Durda, D.D. and Kring, D.A. (2015). Size-frequency and spatial distribution of ejecta blocks at Meteor Crater, AZ. Lunar and Planetary Science XLVI, Abstract #1487.

Fairchild, H. L. (1907). Origin of meteor crater (Coon butte), Arizona. Bulletin of the Geological Society of America, 18(1), 493-504.

Fergason, R. L., Christensen, P. R., Bell III, J. F., Golombek, M. P., Herkenhoff, K. E., & Kieffer, H. H. (2006). Physical properties of the Mars Exploration Rover landing sites as inferred from Mini-TES–derived thermal inertia. Journal of Geophysical Research: Planets, 111(E2).

Garvin, J. B., Schnetzler, C. C., & Grieve, R. A. (1992). Characteristics of large terrestrial impact structures as revealed by remote sensing studies. Tectonophysics, 216(1-2), 45-62.

Ghent, R. R., Carter, L. M., Bandfield, J. L., Udovicic, C. T., & Campbell, B. A. (2016). Lunar crater ejecta: Physical properties revealed by radar and thermal infrared observations. Icarus, 273, 182-195.

Ghent, R. R., Hayne, P. O., Bandfield, J. L., Campbell, B. A., Allen, C. C., Carter, L. M., & Paige, D. A. (2014). Constraints on the recent rate of lunar ejecta breakdown and implications for crater ages. Geology, 42(12), 1059-1062.

Gilbert, G.K. (1896). The origin of hypotheses, illustrated by the discussion of a topographic problem. Science, v. 3, pp. 1-13.

Grant, J. A., & Schultz, P. H. (1993). Erosion of ejecta at Meteor Crater, Arizona. Journal of Geophysical Research: Planets, 98(E8), 15033-15047.

Gupta, R. P. (1991). Remote sensing geology. Springer.

Hayne, P. O., Bandfield, J. L., Siegler, M. A., Vasavada, A. R., Ghent, R. R., Williams, J. P., ... & Paige, D. A. (2017). Global regolith thermophysical properties of the Moon from the Diviner Lunar Radiometer Experiment. Journal of Geophysical Research: Planets, 122(12), 2371-2400.

Jakosky, B. M. (1986). On the thermal properties of Martian fines. Icarus, 66(1), 117-124.

Jakosky, J.J., Wilson, C.H., and Daly, J.W. (1932). Geophysical examination of Meteor crater, Arizona. American Institute of Mining, Metallurgical, and Petroleum Engineers, Transactions, v. 97, pp. 63-98

Kahle, A. B. (1987). Surface emittance, temperature, and thermal inertia derived from Thermal Infrared Multispectral Scanner (TIMS) data for Death Valley, California. Geophysics, 52(7), 858-874.

Kieffer, H. H., Chase Jr, S. C., Miner, E., Münch, G., & Neugebauer, G. (1973). Preliminary report on infrared radiometric measurements from the Mariner 9 spacecraft. Journal of Geophysical Research, 78(20), 4291-4312.

Kieffer, H. H., Martin, T. Z., Peterfreund, A. R., Jakosky, B. M., Miner, E. D., & Palluconi, F. D. (1977). Thermal and albedo mapping of Mars during the Viking primary mission. Journal of Geophysical Research, 82(28), 4249-4291.

Kieffer, H. H., Martin, T. Z., Peterfreund, A. R., Jakosky, B. M., Miner, E. D., & Palluconi, F. D. (1977). Thermal and albedo mapping of Mars during the Viking primary mission. Journal of Geophysical Research, 82(28), 4249-4291.

Kring (2017). Guidebook to the Geology of Barringer Meteorite Crater, Arizona (a.k.a. Meteor Crater) 2nd edition. The Lunar and Planetary Institute.

Kring, D. A. (1997). Air blast produced by the Meteor Crater impact event and a reconstruction of the affected environment. Meteoritics & Planetary Science, 32(4), 517-530.

Kring, D.A., Balcerski, J., Blair, D.M., Chojnacki, M., Donohue, P.H., Drummond, S.A., Garber, J.M., Hopkins, M., Huber, M.S., Jaret, S.J., Losiak, A., Maier, A., Mithell, J., Ong, L., Ostrach, L.R., O'Sullivan, K.M., Potter, R.W.K., Robbins, S., Shankar, B., Shea, E.K., Singer, K.N., Sori, M., Sturm, S., Willmes, M., Zanetti, M., and Wittmann, A. (2011a). Asymmetrical distribution of impact ejected lithologies at Barringer Meteorite Crater (aka Meteor Crater). Lunar and Planetary Science XLII, Abstract #1746.

Kring, D.A., Balcerski, J., Blair, D.M., Chojnacki, M., Donohue, P.H., Drummond, S.A., Garber, J.M., Hopkins, M., Huber, M.S., Jaret, S.J., Losiak, A., Maier, A., Mithell, J., Ong, L., Ostrach, L.R., O'Sullivan, K.M., Potter, R.W.K., Robbins, S., Shankar, B., Shea, E.K., Singer, K.N., Sori, M., Sturm, S., Willmes, M., Zanetti, M., and Wittmann, A. (2011b). Fold hinge in overturned Coconino sandstone and its structural displacement during the formation of

Barringer Meteorite Crater (aka Meteor Crater). Lunar and Planetary Science XLII, Abstract #1740.

Kumar, P. S., & Kring, D. A. (2008). Impact fracturing and structural modification of sedimentary rocks at Meteor Crater, Arizona. Journal of Geophysical Research: Planets, 113(E9).

Kumar, P. S., Head, J. W., & Kring, D. A. (2010). Erosional modification and gully formation at Meteor Crater, Arizona: Insights into crater degradation processes on Mars. Icarus, 208(2), 608-620.

Lawson, S. L., & Jakosky, B. M. (2001). Lunar surface thermophysical properties derived from Clementine LWIR and UVVIS images. Journal of Geophysical Research: Planets, 106(E11), 27911-27932.

McCarty, C. B., & Moersch, J. E. (2020). Remote characterization of physical surface characteristics of Mars using diurnal variations in apparent thermal inertia. Icarus, 345, 113739.

Mellon, M. T., Jakosky, B. M., Kieffer, H. H., & Christensen, P. R. (2000). High-resolution thermal inertia mapping from the Mars global surveyor thermal emission spectrometer. Icarus, 148(2), 437-455.

Mokhtari, M. H., Busu, I., Mokhtari, H., Zahedi, G., Sheikhattar, L., & Movahed, M. A. (2013). Neural network and multiple linear regression for estimating surface albedo from ASTER visible and near-infrared spectral bands. Earth Interactions, 17(3), 1-20.

Nishiizumi, K., Kohl, C. P., Shoemaker, E. M., Arnold, J. R., Klein, J., Fink, D., & Middleton, R. (1991). In situ10Be-26Al exposure ages at Meteor Crater, Arizona. Geochimica et Cosmochimica Acta, 55(9), 2699-2703.

Nypaver, C. A., Thomson, B. J., Fassett, C. I., Rivera-Valentín, E. G., & Patterson, G. W. (2021). Prolonged Rock Exhumation at the Rims of Kilometer-Scale Lunar Craters. Journal of Geophysical Research: Planets, 126(7), e2021JE006897.

Phillips, F. M., Zreda, M. G., Smith, S. S., Elmore, D., Kubik, P. W., Dorn, R. I., & Roddy, D. J. (1991). Age and geomorphic history of Meteor Crater, Arizona, from cosmogenic 36Cl and 14C in rock varnish. Geochimica et Cosmochimica Acta, 55(9), 2695-2698.

Piqueux, S., & Christensen, P. R. (2009). A model of thermal conductivity for planetary soils: 1. Theory for unconsolidated soils. Journal of Geophysical Research: Planets, 114(E9).

Piqueux, S., & Christensen, P. R. (2009). A model of thermal conductivity for planetary soils: 2. Theory for cemented soils. Journal of Geophysical Research: Planets, 114(E9).

Presley, M. A., & Christensen, P. R. (1997). Thermal conductivity measurements of particulate materials 1. A review. Journal of Geophysical Research: Planets, 102(E3), 6535-6549.

Presley, M. A., & Christensen, P. R. (1997). Thermal conductivity measurements of particulate materials 2. Results. Journal of Geophysical Research: Planets, 102(E3), 6551-6566.

Price, J. C. (1977). Thermal inertia mapping: A new view of the earth. Journal of Geophysical Research, 82(18), 2582-2590.

Putzig, N. E. (2006). Thermal inertia and surface heterogeneity on Mars. University of Colorado at Boulder.

Ramsey, M. S. (2002). Ejecta distribution patterns at Meteor Crater, Arizona: On the applicability of lithologic end-member deconvolution for spaceborne thermal infrared data of Earth and Mars. Journal of Geophysical Research: Planets, 107(E8), 3-1.

Reger, R. D., & Batchelder, G. L. (1971). Late Pleistocene molluscs and a minimum age of Meteor Crater, Arizona. Journal of the Arizona Academy of Science, 6(3), 190-195

Roddy, D. J., Boyce, J. M., Colton, G. W., & Dial, A. L. (1975). Meteor Crater, Arizona Rim Drilling, Volume, Thickness, Depth, and Energy Calculations. In Lunar and Planetary Science Conference (Vol. 6).

Roddy, D.J. (1978). Pre-impact geologic conditions, physical properties, energy calculations, meteorite and initial crater dimensions and orientations of joints, faults and walls at Meteor Crater, Arizona. Proc. Lunar Planetary Science Conf. 9th, pp. 3,891-3,930.

Roy, S., & Stewart, R. R. (2012). Near-surface seismic investigation of Barringer (meteor) crater, Arizona. Journal of Environmental and Engineering Geophysics, 17(3), 117-127.

Russell, P. S., Grant, J. A., Williams, K. K., Carter, L. M., Brent Garry, W., & Daubar, I. J. (2013). Ground penetrating radar geologic field studies of the ejecta of Barringer Meteorite Crater, Arizona, as a planetary analog. Journal of Geophysical Research: Planets, 118(9), 1915-1933.

Russell, P. S., Grant, J. A., Williams, K. K., Carter, L. M., Brent Garry, W., & Daubar, I. J. (2013). Ground penetrating radar geologic field studies of the ejecta of Barringer Meteorite Crater, Arizona, as a planetary analog. Journal of Geophysical Research: Planets, 118(9), 1915-1933.

Sabol, D. E., Gillespie, A. R., McDonald, E., & Danillina, I. (2006). Differential thermal inertia of geological surfaces. In Proceedings of the 2nd Annual International Symposium of Recent Advances in Quantitative Remote Sensing, Torrent, Spain (pp. 25-29).

Schmieder, M., Boschi, S., Caudill, C., Chandnani, M., DiFrancesco, N.J., Hibbard, S.M., Hughson, K., Kinczyk, M., Martin, A.C., Martin, E., Martinot, M., McCarty, C.B., Powell, K.E., Sarafian, A., Schaub, D.R., Shirley, K., and D. A. Kring (2017). Mapping ejecta on the east and southeast side of Barringer Meteorite Crater (a.k.a. Meteor Crater), Arizona. Lunar and Planetary Science XLVIII, Abstract #2180.

Shoemaker, E.M. (1960). Impact mechanics at Meteor Crater, Arizona. Princeton University.

Shoemaker, E.M. (1963). Impact mechanics at Meteor crater, Arizona. In: The Moon, Meteorites and Comets, edited by Middlehurst, B.M. and Kuiper, G.P., University of Chicago Press, Chicago, v. IV, pp. 301-336.

Shoemaker, E.M. and Kieffer, S.W. (1974). Guidebook to the geology of Meteor crater, Arizona. Meteoritical Society, 37th Annual Meeting, Arizona State University Centre for Meteorite Studies, Tempe, Arizona, 1974 (66 pp.) Reprinted in 1988.

Spaulding, W. G., & Graumlich, L. J. (1986). The last pluvial climatic episodes in the deserts of southwestern North America. Nature, 320(6061), 441-444.

Sutton, S. R. (1985). Thermoluminescence measurements on shock-metamorphosed sandstone and dolomite from Meteor Crater, Arizona: 1. Shock dependence of thermoluminescence properties. Journal of Geophysical Research: Solid Earth, 90(B5), 3683-3689.

Watkins, R. N., Jolliff, B. L., Mistick, K., Fogerty, C., Lawrence, S. J., Singer, K. N., & Ghent, R. R. (2019). Boulder distributions around young, small lunar impact craters and implications for regolith production rates and landing site safety. Journal of Geophysical Research: Planets, 124(11), 2754-2771.

Williams, J. P., Pathare, A. V., Costello, E. S., Gallinger, C. L., Hayne, P. O., Ghent, R. R., ... & Elder, C. M. (2022). The effects of terrain properties upon the small crater population distribution at Giordano Bruno: Implications for lunar chronology. Journal of Geophysical Research. Planets, 127(5).

Wright, S. P., & Ramsey, M. S. (2006). Thermal infrared data analyses of Meteor crater, Arizona: Implications for Mars spaceborne data from the Thermal Emission Imaging System. Journal of Geophysical Research: Planets, 111(E2).

Yamaguchi, Y., Kahle, A. B., Tsu, H., Kawakami, T., & Pniel, M. (1998). Overview of advanced spaceborne thermal emission and reflection radiometer (ASTER). IEEE Transactions on geoscience and remote sensing, 36(4), 1062-1071.

Appendix

Figures

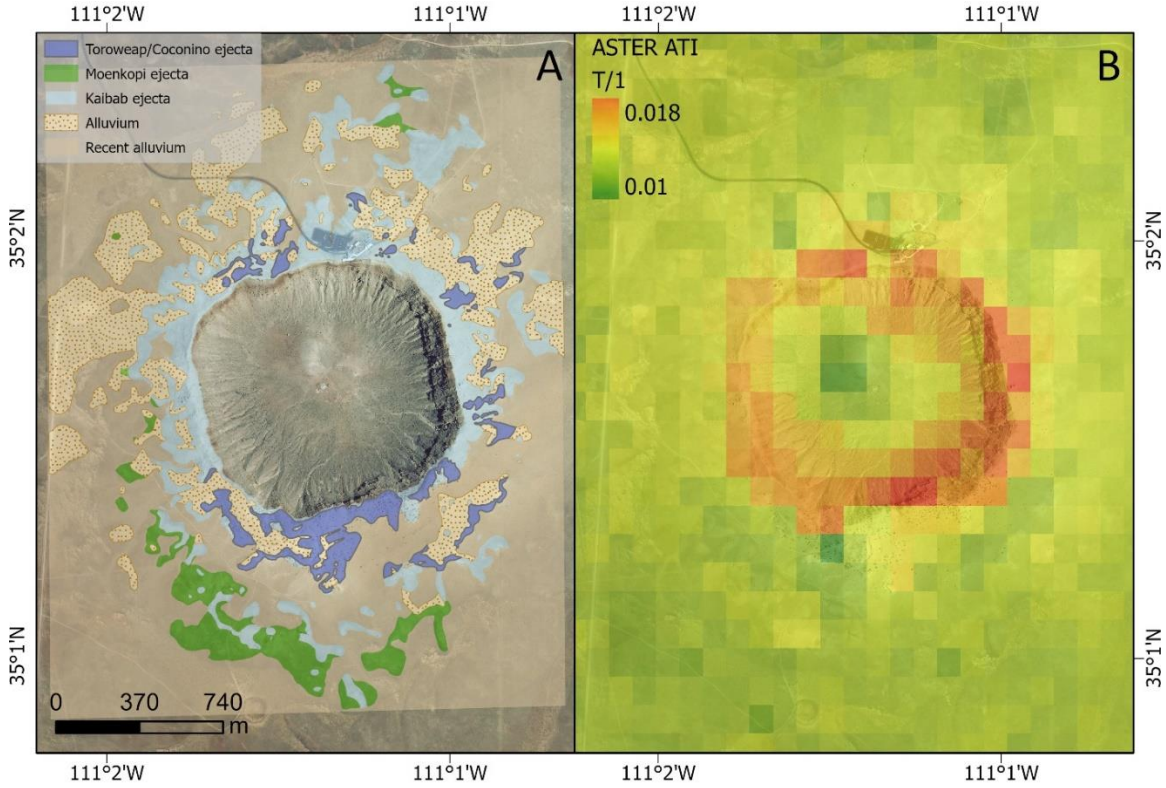

Figure 3.1. (a) United States Geological Survey (USGS) orthophoto mosaic (~1.0 m/pixel) of Meteor Crater overlaid by digitized versions of the original ejecta units produced by Shoemaker, 1960. The unit boundaries presented here were digitized by tracing the unit boundaries from the original Meteor Crater geologic map at a scale of 1:1000 in ArcGIS Pro. (b) USGS Orthophoto mosaic overlaid by ASTER apparent thermal inertia (ATI) data derived in this work. The highest ATI values are associated with the crater walls and rim. Such elevated ATI values are expected due to the dependency of insolation history on the slopes and slope azimuths of those areas. The ATI data associated with the E-SE crater rim are elevated relative to other areas of the crater structure and ejecta.

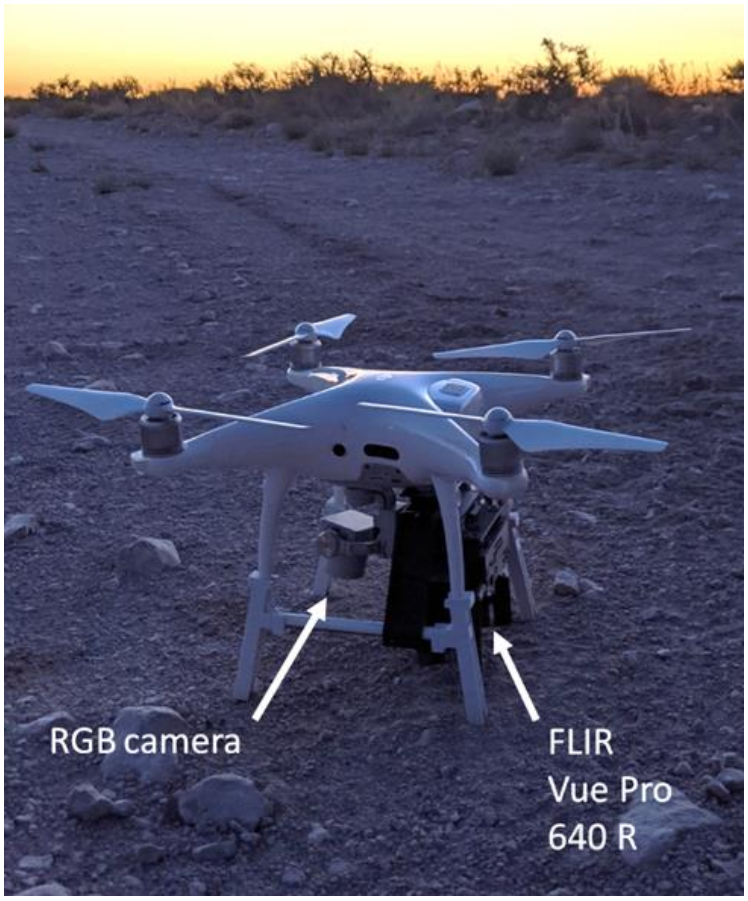

Figure 3.2. DJI Phantom 4 Pro sUAS (drone) equipped with a 20 Mpixel RGB camera and a FLIR Vue Pro 640R thermal camera.

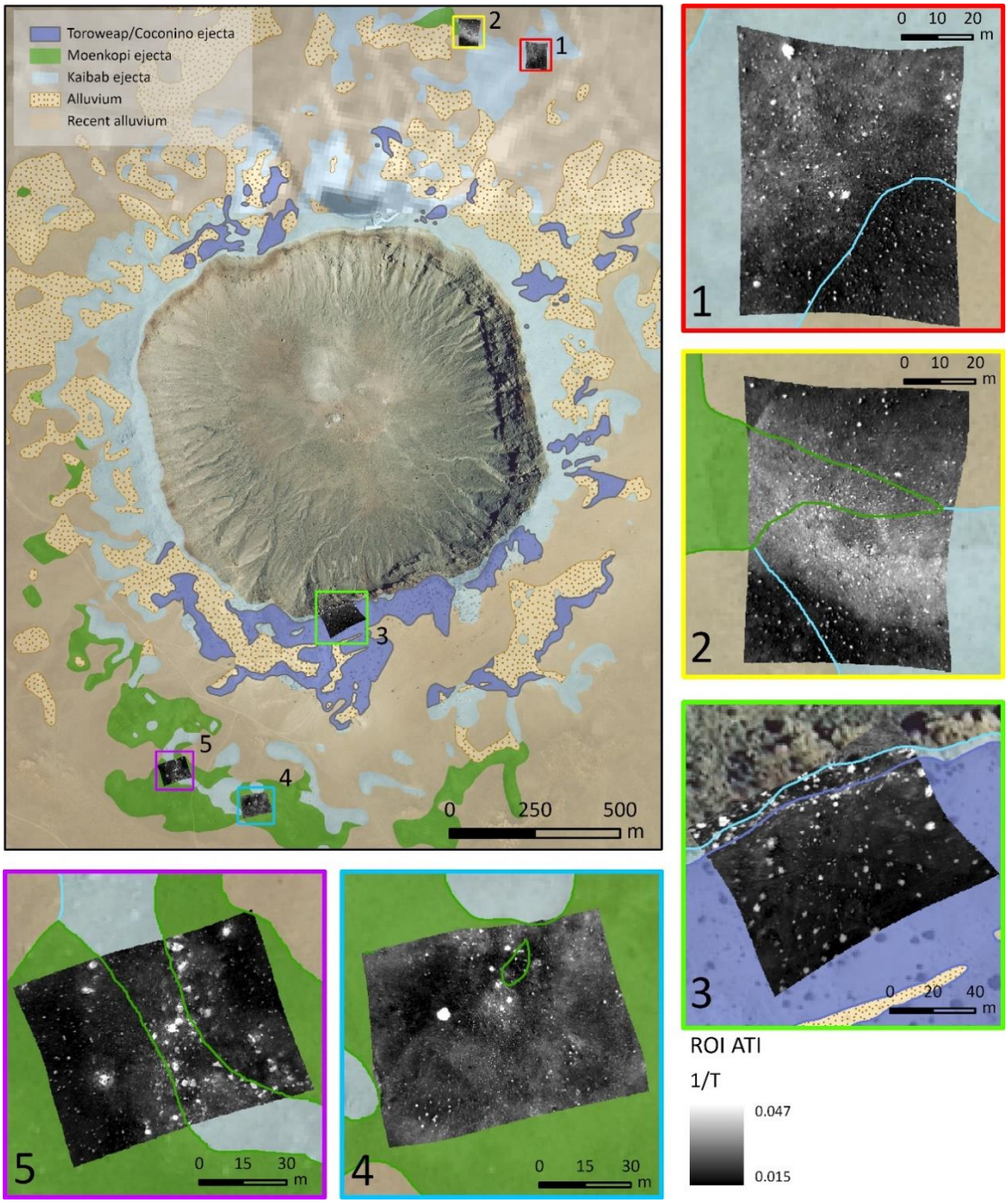

Figure 3.3. USGS orthophoto mosaic overlaid by compositional ejecta units with the locations of five drone-based apparent thermal inertia (ATI) images derived in this work. Numbers next to each extent indicator box represent the respective ROI numbers and the order in which the image data were collected. Extent indicator colors correspond to the borders of enlarged ROI ATI maps.

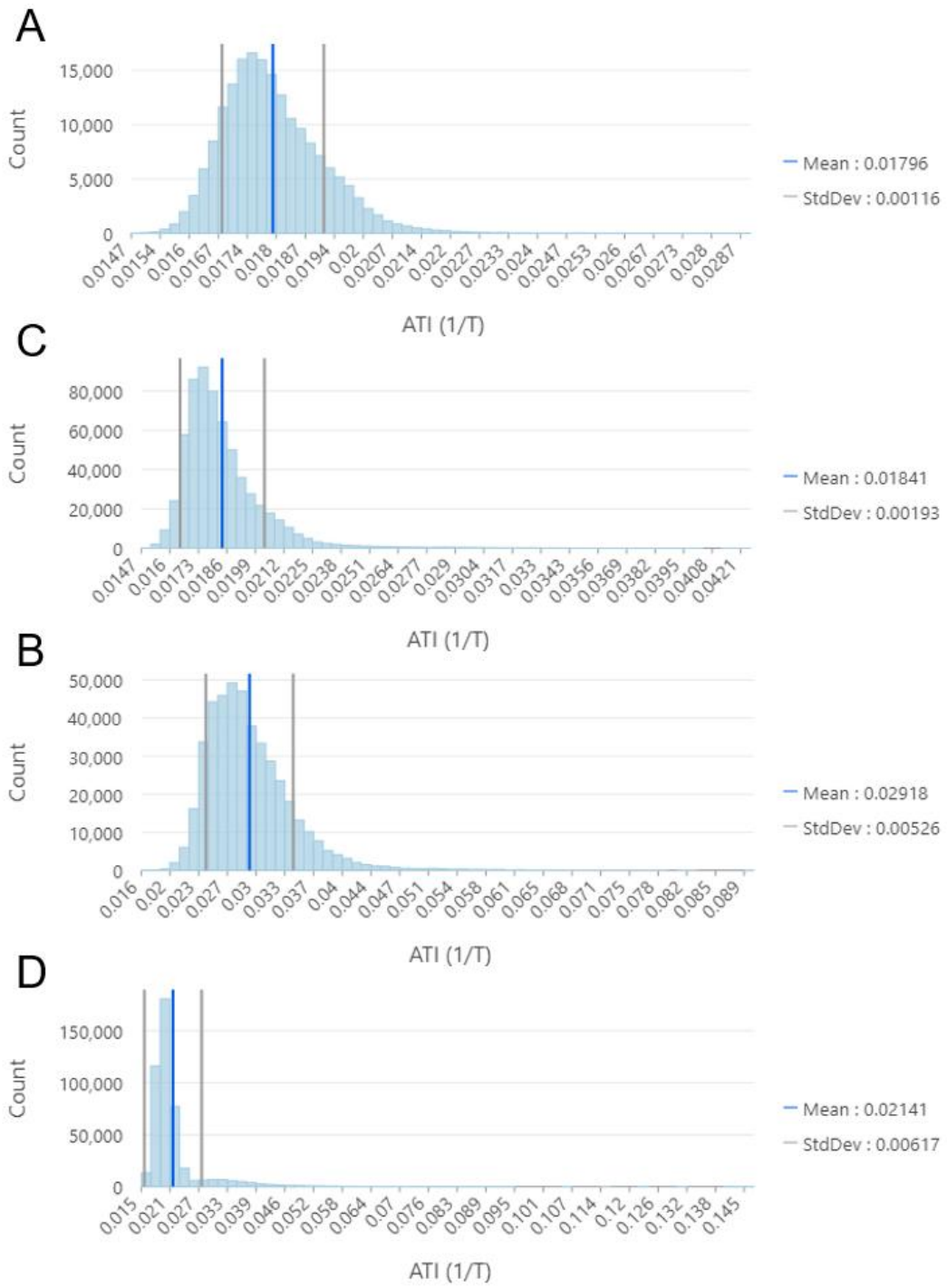

Figure 3.4. Histogram distributions of drone-based ATI data associated with (a) Alluvium, (b) Moenkopi, (c) Coconino, and (d) Kaibab ejecta. Each histogram represents combined ATI data from all ROIs in which respective units were sampled. The thermophysical effects of surface vegetation have been removed from these data via manual clipping of the high ATI pixels associated with vegetation in each ATI image.

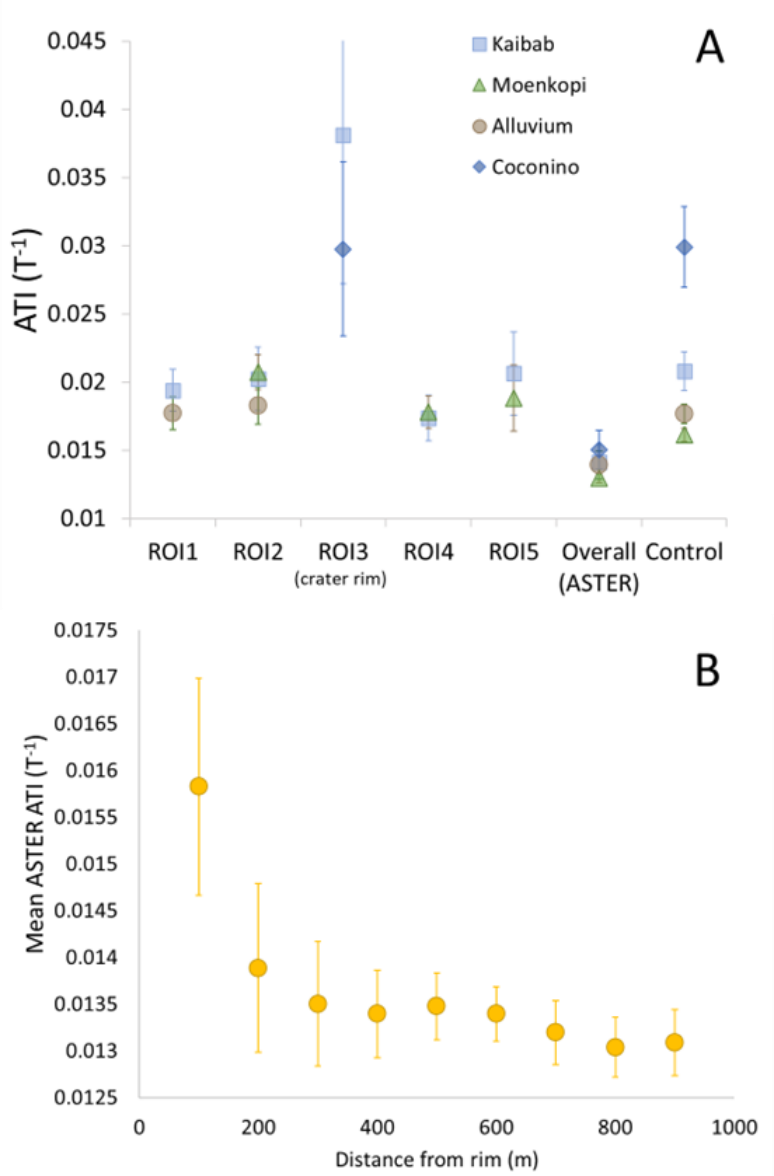

Figure 3.5. (a) Mean drone-based and ASTER apparent thermal inertia (ATI) values binned using previously identified unit boundaries within the Meteor Crater Ejecta deposit (Shoemaker, 1960; 1963). Drone-based ROI data are presented in the order in which they were collected from left to right on the x-axis followed by ASTER ATI data and drone-based control ATI values, respectively. Error bars represent the standard deviation for each mean value. Data point colors correspond to map unit colors in Fig. 3.1a. (b) Mean ASTER ATI values as a function of distance from the Meteor Crater rim. Radial ATI data were collected by drawing successive 100-m-wide concentric bins around the crater rim and measuring the average ATI under each using the ArcGIS Pro zonal statistics tool. Error bars represent standard deviation for each radial mean value.

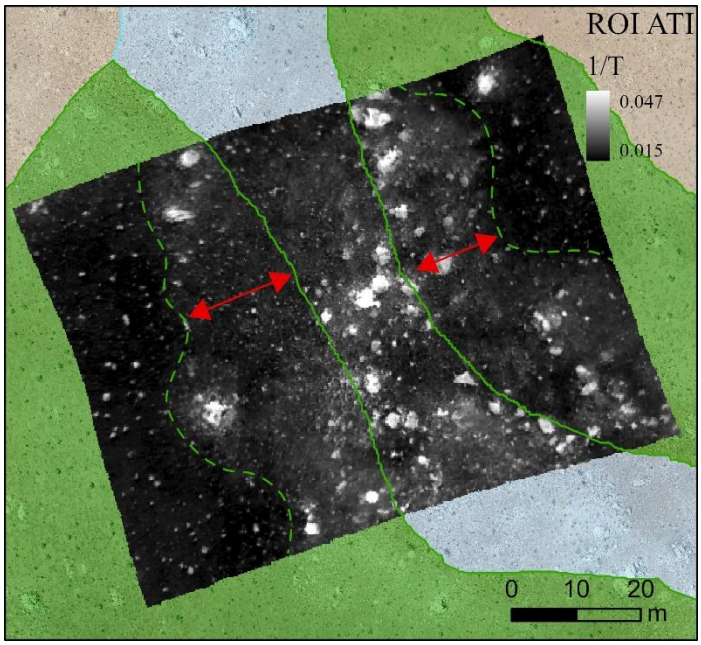

Figure 3.6. ROI5 apparent thermal inertia (ATI) image showing the original Kaibab-Moenkopi unit boundary (solid green line) and the perceived thermophysical boundary between the two compositional units (dashed green boundary) that has been extended due to erosion-induced mixing of the two units. Red arrows indicate the area of horizontal mixing between the unit boundaries.

Tables

Table 3.1. Comparison test between two potential data binning methods for FLIR thermophysical data. The radiance-binning method accounts for the non-linear dependence of temperature on radiance within a given field of view. The ATI direct-binning does not account for that dependence, but is less computationally intensive. As illustrated by this test comparison test between the two methods for compositional units in ROI 2, the percent difference in ATI values that result from these two methods are negligible. Therefore, we utilize the temperature binning method in the present investigation.

ROI2 Radiance-binned morning temperatures			
	Moenkopi	Kaibab	Alluvium
Radiance @10.5 microns	7.7860	7.6860	7.5570
Mean Temperature	285.7900	285.0280	284.0360
ROI2 Radiance-binned afternoon temperatures			
	Moenkopi	Kaibab	Alluvium
Radiance @10.5 microns	13.9810	14.1220	14.7540
Mean Temperature	325.0280	325.7920	329.1660
ROI2 Radiance-binned ATI			
	Moenkopi	Kaibab	Alluvium
ROI2 Albedo	0.1750	0.1810	0.1840
ROI2 ATI	0.0210	0.0201	0.0181
ROI2 Direct-binned ATI			
	Moenkopi	Kaibab	Alluvium
ROI2 Albedo	0.1750	0.1810	0.1840
ROI2 ATI	0.0207	0.0202	0.018244
Percent difference between binning methods	0.0148	0.0051	0.0090

Table 3.2. Apparent thermal inertia (ATI) mean, minimum, maximum, standard deviation corresponding to the compositional units represented in each ROI, as well as overall ASTER ATI values and control ATI values corresponding to each compositional unit.

Kaibab	Mean ATI	Max	Min	Std. Dev.	Uncertainty
Overall (ASTER)	0.014	0.018	0.012	0.001	8.851
Control	**0.021**	**0.029**	**0.017**	0.001	6.698
ROI1	0.019	0.034	0.015	0.002	8.012
ROI2	0.020	0.034	0.014	0.002	11.423
ROI3	0.038	0.147	0.024	0.011	28.645
ROI4	0.017	0.028	0.015	0.002	9.573
ROI5	0.021	0.045	0.016	0.003	14.740
Moenkopi					
Overall (ASTER)	0.013	0.014	0.012	0.000	2.525
Control	0.016	0.020	0.015	0.000	3.013
ROI1	–	–	–	–	–
ROI2	0.021	0.032	0.017	0.001	6.188
ROI3	–	–	–	–	–
ROI4	0.018	0.035	0.015	0.001	6.674
ROI5	0.019	0.043	0.015	0.002	12.831
Alluvium					
Overall (ASTER)	0.014	0.011	0.018	0.001	7.484
Control	0.018	0.025	0.016	0.001	3.988
ROI1	0.018	0.030	0.015	0.001	6.804
ROI2	0.018	0.031	0.015	0.001	7.488
ROI3	–	–	–	–	–
ROI4	–	–	–	–	–
ROI5	–	–	–	–	–
Coconino					
Overall (ASTER)	0.015	0.017	0.013	0.001	9.278
Control	0.030	0.048	0.023	0.003	9.859
ROI1	–	–	–	–	–
ROI2	–	–	–	–	–
ROI3	0.030	0.092	0.016	0.006	21.434
ROI4	–	–	–	–	–
ROI5	–	–	–	–	–

Supplemental Information

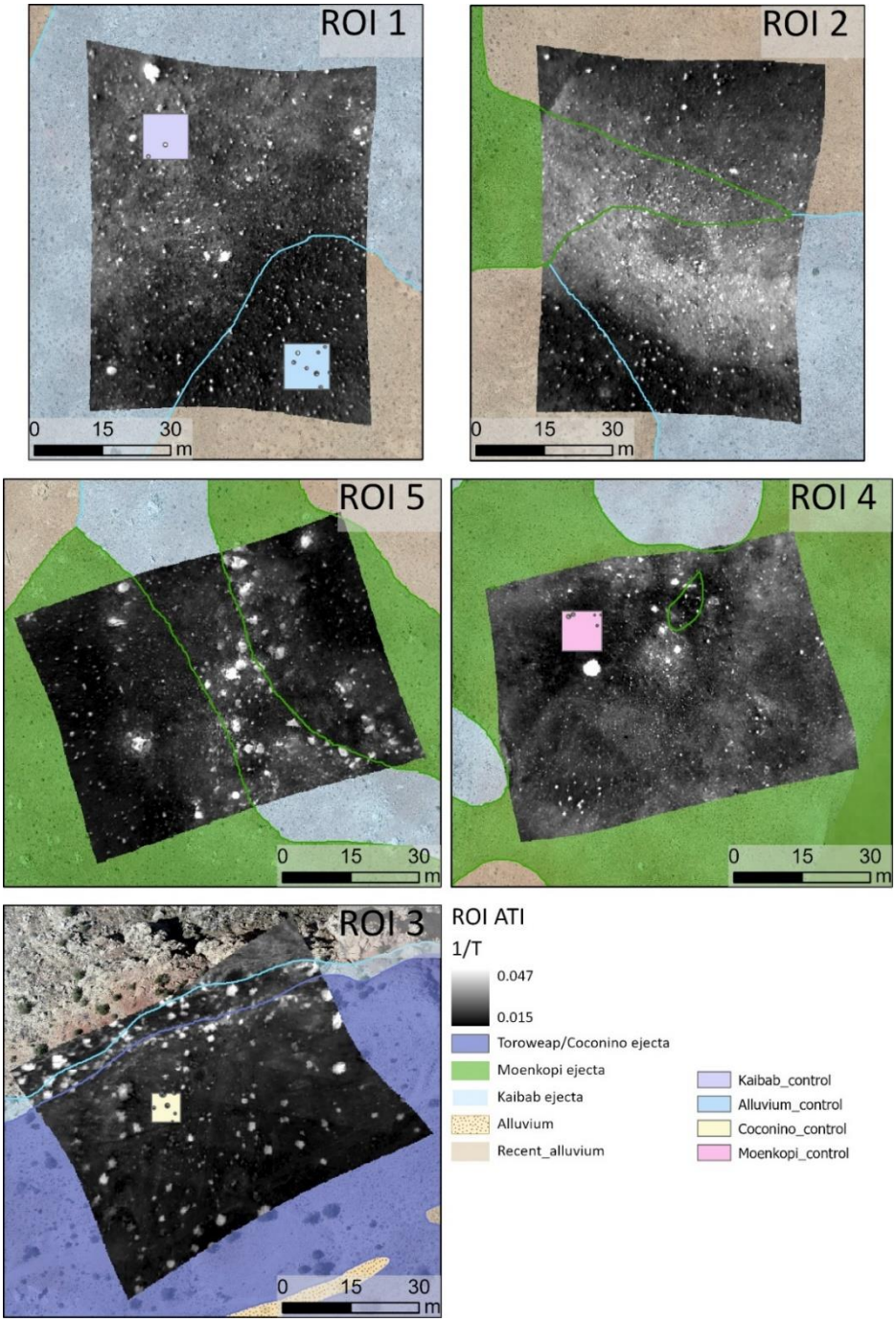

Figure 3.S7. Enhanced ROI apparent thermal inertia (ATI) images overlaid onto a USGS orthophoto mosaic (~1m/pixel) and digitized unit boundaries from Shoemaker, 1960; 1963. Locations of control ATI sampling are shown with 10 m x 10 m polygons. Similar to ATI data collection over defined units, vegetation was clipped from the control ATI sampling polygons before measurement to ensure sampling of geologic surface materials only.

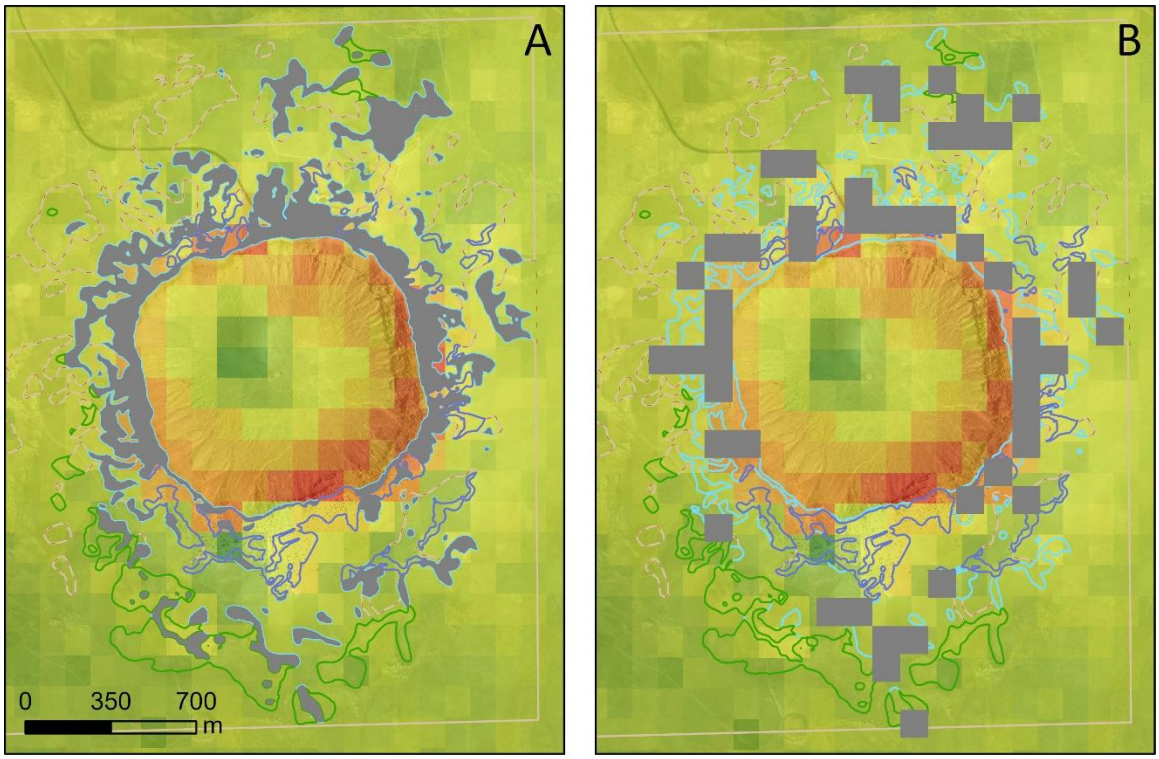

Figure 3.S8. (A) An example of the zonal statistics sampling for Kaibab ejecta ASTER ATI using an upsampled grid (i.e., the method used in this work) and (B) the default zonal statistics sampling method for Kaibab ejecta in ASTER apparent thermal inertia (ATI) data. By default, The ArcGIS Pro zonal statistics tool only samples those pixels from the input value raster with center points that are directly under the feature zone (i.e., B). In the work presented here, we artificially upsample the input value raster and average based on the pixel resolution from another raster that is already in the data frame (the 23cm/pixel drone-based ATI images). This smaller sampling grid allows us to account for only those input raster pixels that are contained within the feature zone boundaries. This method weights the mean by the area of the pixel covered by the feature zone and provides a more accurate representation of the ASTER ATI than the default zonal statistics method.

Figure 3.S9. Two previously established mining roads cutting through the Meteor Crater ejecta deposit. These roads trend ~E-W parallel to the south rim of the crater. The left road transects our ROI3 ATI image and likely influences the Kaibab ATI measurement in that ROI to a small degree..

CONCLUSIONS

The work presented in this dissertation yields several new insights into the geomorphic and tectonic evolution of the lunar surface. Moreover, our work improves the understanding of the thermophysical and radar remote sensing datasets used to determine the geologic history of a planetary surface. In chapter 1, radar and thermophysical measurements corresponding to >6,000 km-scale impact craters on the lunar maria revealed that impact ejecta deposits, specifically at impact crater rims, break down at an exponential and predictable rate. That rate remains underutilized as a tool for planetary age dating, and a logical expansion of this work would include fitting impact craters of an unknown formation age to those established breakdown rates to derive surface ages independently of traditional impact crater production functions. The comparison impact crater rim and ejecta evolution rates also revealed that impact crater rims retain elevated rock populations for longer than the predicted lifetime of a boulder on the lunar surface. Such a result led to the interpretation that rocks are being exhumed from the subsurface at a rate that outpaces the race of surface rock breakdown on the Moon.

The initial goal of chapter two was to identify the mechanism responsible for causing downslope movement of regolith at impact crater rims (i.e., the seismic source of surface acceleration). Potential seismic sources in the lunar maria included shallow moonquakes recorded by the Apollo seismic program and recently active lobate scarps near the mare-highlands boundary. Until that point, published observations of recently active wrinkle ridges on the lunar maria were limited to local regions of Mare Frigoris and Mare Imbrium. Hence, when we identified a population of recently active wrinkle ridges across the entire nearside mare, an in depth investigation of the timing, spatial distribution, and origin of those newly identified wrinkle ridges took precedence as the most valuable contribution to the lunar scientific community. Our initial reconnaissance mapping and analysis of those features indicated that they were indeed, recently, active based on their cross-cutting relationships with small lunar impact craters, but the origin of the compressional stress responsible for their formation remains unclear. Future work is already underway to establish the absolute model ages and fault kinematics associated with the newly discovered population of tectonic features identified in this work. Such information will help to reveal the exact contributions of lunar compressional stress mechanisms to the formation of recently active wrinkle ridges on the lunar maria.

As mentioned previously, the final chapter of this dissertation was an intentional extension of chapter one results and interpretations. Meteor Crater in NE Arizona, USA serves as an ideal analog for planetary impact crater investigations due to it's recent formation in an arid environment that is generally devoid of vegetation. Our work drew comparisons between drone-based and orbital thermophysical measurements of the Meteor Crater Ejecta deposit. Those measurements were compared with compositional surface units established during the original geologic mapping of the crater. The thermophysical data, sensitive to surface grain size distribution and induration, showed broad

correlations with surface composition at the scale of the orbital resolution. The drone-based thermophysical data also correlated well with surface composition when the data were sampled in areas of the ejecta that were devoid of unit boundaries, obvious erosion, or human disturbance. However, when the drone-based data were binned and averaged based on previously defined compositional unit boundaries, no correlation between composition and thermophysical properties was observed. This lack of a correlation was interpreted to be the result of some combination of horizontal mixing and erosion of geologic materials at the surface and, to a lesser degree, error associated with the originally defined map boundaries. Such a result indicates the sub pixel mixing is likely affecting similar observations and models of ejecta depositions on other terrestrial planets. The results of this project were foreshadowed by the findings of chapter one in two ways: 1) The difference between crater rim and ejecta thermophysical signatures reveals intra-ejecta variability in remote sensing data that was previously unresolved in coarse-resolution remote sensing data and 2) boulder exhumation is a known phenomenon to have occurred at Meteor Crater. Estimates of vertical deflation/erosion at the rim of Meteor Crater are an order of magnitude greater than farther out in the ejecta deposit. Such connections reiterate the value that Meteor Crater and other terrestrial analogs hold in planetary science.

VITA

Cole Nypaver grew up in Scenery Hill, Pennsylvania where he developed a passion for the natural world from an early age. His introduction into scientific research was made through the Pennsylvania Junior Academy of Sciences (PJAS) where he would go on to earn a first place and a perfect score in the state PJAS presentation competition during his eighth-grade year at John F. Kennedy middle school in Washington, Pennsylvania. His science project that year focused on the decomposition rate of surface matter as a function of earthworm density in the underlying soil. After high school, Cole went on to major in Geology at Mercyhurst University in Erie Pennsylvania under the guidance of his advisor, Dr. Nicholas Lang. After spending several semesters with a major concentration in Paleontology, he transitioned into planetary science in his junior year at Mercyhurst (although, Paleontology remains an interest of Cole's to this day). The impetus for Cole's transition into planetary science came in the form of an internal internship that was offered to him by his advisor, Dr. Nicholas Lang. Cole's task during this internship was to produce a reconnaissance geologic map of the V-49 Mahuea Tholus quadrangle of Venus using Magellan radar data. This task foreshadowed Cole's graduate research career as he would continue to use orbital synthetic aperture radar data in his research for many years to come. It was also, through this internship, where Cole met his future graduate advisor, Dr. Bradley Thomson, who was a close colleague of his undergraduate advisor and a collaborator on the Venusian mapping project that Cole worked on during his undergraduate career. Cole went on to pursue a Master of Science degree in Geology at the University of Tennessee, Knoxville with his advisors Dr. Bradley Thomson and Dr. Devon Burr. His M.S. research was focused on measuring the rate of lunar impact crater degradation using synthetic aperture radar data from the Miniature Radar Frequency (Mini-RF) Instrument onboard the Lunar Reconnaissance Orbiter. Due to his proficient use of the Mini-RF radar dataset and Dr. Bradley Thomson's position as a Mini-RF science team co-investigator, Cole was named as a science team affiliate to the Mini-RF instrument in 2018. He would go on to work directly with the Mini-RF science team throughout the remainder of his graduate career. After completing his M.S. Degree in December of 2019, Cole re-applied and was accepted to work with Dr. Thomson as a Ph.D. student in the UTK department of Earth and Planetary Sciences. Cole and Dr. Thomson would go on to publish new scientific findings pertaining to lunar impact crater breakdown processes and recent tectonic activity in peer-reviewed journals such as The Journal of Geophysical Research and Geophysical Research Letters. Cole would also go on to independently publish research findings pertaining to radar detection on lunar lava flows in the Planetary Science Journal with his colleagues from the Mini-RF Science team. After receiving his PhD, Cole intends to continue his research career by delving deeper into the aspects of lunar science that are described in his dissertation.